POLITECNICO
MILANO 1863

SCUOLA DI INGEGNERIA INDUSTRIALE
E DELL'INFORMAZIONE

Lightweight solutions for High Manganese steel

TESI DI LAUREA MAGISTRALE IN
BIO INSPIRED ENGINEERING
INGEGNERIA MECCANICA

Author: **Xuwei Xu**

Student ID: 11009598
Advisor: Prof. Carlo Mapelli
Co-advisor: Bazri Shahab
Academic Year: 2025-26

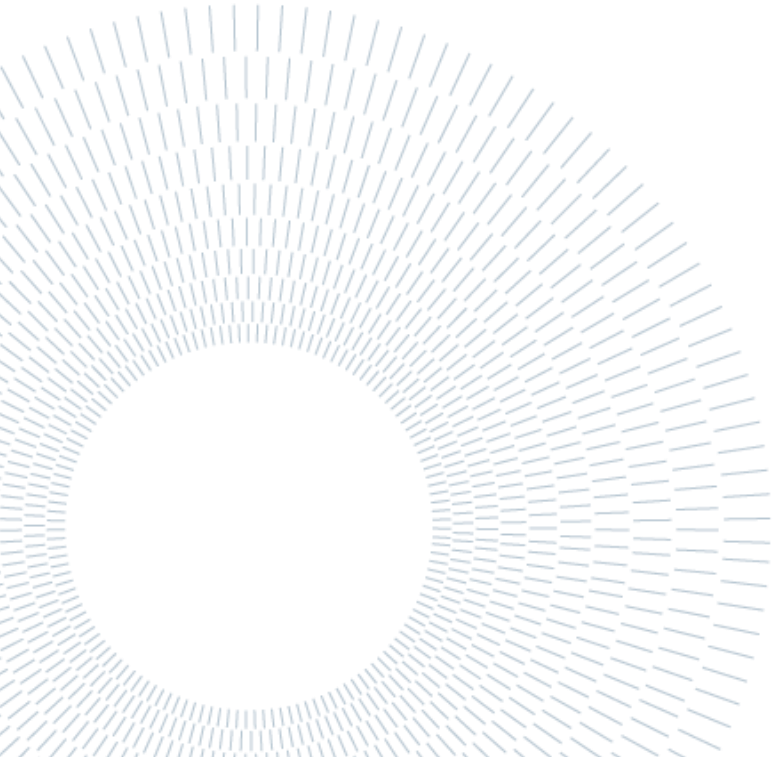

Abstract

The increasing demand for energy efficiency, reduced emissions, and enhanced structural performance has intensified the need for lightweight materials with high specific mechanical properties. High-manganese steels are particularly attractive due to their excellent ductility, toughness, and strain-hardening capability; however, their relatively high density limits their application in weight-critical components. A common strategy for density reduction is the addition of aluminium in Fe–Mn–Al–C low-density steels. Nevertheless, this approach is not universally applicable. In specific environments, such as lead-cooled nuclear reactors, the high chemical reactivity of aluminium and its detrimental behaviour at elevated temperatures make its use unfavourable. In these cases, steels rich in chromium are required to ensure corrosion resistance and thermal stability, resulting in inherently higher density. Consequently, lightweight design cannot rely on alloy chemistry alone and must be achieved through structural optimization. Bioinspired geometry represents an effective solution to this challenge.

This thesis investigates two complementary lightweight strategies for high-Mn steels: alloy design through aluminium addition and bioinspired structural optimization for dense, Al-free alloys. The first part of the work analyses Fe–Mn–Al–C low-density steels, focusing on the role of aluminium in density reduction, phase stability, κ-carbide formation, and strengthening mechanisms. A novel high-Mn alloy is experimentally characterized and compared with a reference material in terms of microstructure and mechanical behaviour.

The second part of the thesis addresses lightweight design through geometry, inspired by the hierarchical porous structure of the cholla cactus skeleton. This approach enables mass reduction while preserving load-bearing capacity, making it particularly suitable for high-density, Cr-rich steels intended for high-temperature and corrosive environments. Thin-walled hollow cylindrical cellular structures were designed using a bioinspired methodology and evaluated through analytical modelling, finite element simulations, and experimental compression tests. The structures were manufactured via additive manufacturing and then investment casting, considering technological constraints and scalability.

The results show that aluminium alloying effectively reduces density while maintaining favourable specific mechanical properties, although it introduces microstructural complexities that require careful control. For applications where aluminium cannot be used, bioinspired geometrical optimization significantly

improves the stiffness-to-weight ratio and energy absorption compared to conventional hollow cylinders with the same volume.

This work demonstrates that the integration of advanced alloy development with bioinspired structural design provides a versatile and application-driven pathway for lightweight high-performance components, particularly for extreme environments where material chemistry is constrained.

Keywords: High-Mn steel, Fe–Mn–Al–C steel, lightweight design, bioinspired structures, additive manufacturing, investment casting, finite element analysis, compressive behaviour.

Abstract in italiano

La crescente richiesta di efficienza energetica, riduzione delle emissioni e miglioramento delle prestazioni strutturali ha reso sempre più necessario lo sviluppo di materiali leggeri caratterizzati da elevate proprietà meccaniche specifiche. Gli acciai ad alto contenuto di manganese risultano particolarmente interessanti per applicazioni strutturali grazie alla loro eccellente duttilità, tenacità e capacità di incrudimento; tuttavia, la loro densità relativamente elevata ne limita l'impiego nei componenti sensibili al peso. Una strategia comunemente adottata per la riduzione della densità consiste nell'aggiunta di alluminio negli acciai Fe–Mn–Al–C a bassa densità. Tale soluzione, però, non è universalmente applicabile. In ambienti specifici, come nei reattori nucleari raffreddati a piombo, l'elevata reattività chimica dell'alluminio e il suo comportamento sfavorevole alle alte temperature ne rendono indesiderabile l'utilizzo. In questi contesti sono necessari acciai ricchi in cromo, in grado di garantire resistenza alla corrosione e stabilità termica, ma caratterizzati da densità più elevata. Di conseguenza, la riduzione di peso non può essere ottenuta esclusivamente attraverso la progettazione della lega, ma deve essere perseguita mediante l'ottimizzazione geometrica. In questo scenario, il design bioispirato rappresenta una soluzione efficace.

La presente tesi analizza due strategie complementari per la progettazione leggera degli acciai ad alto contenuto di Mn: la progettazione della lega tramite aggiunta di alluminio e l'ottimizzazione strutturale bioispirata per leghe dense prive di Al. Nella prima parte del lavoro vengono studiati gli acciai Fe–Mn–Al–C a bassa densità, con particolare attenzione al ruolo dell'alluminio nella riduzione della densità, nella stabilità delle fasi, nella formazione dei κ-carburi e nei meccanismi di rafforzamento. Una nuova lega ad alto contenuto di Mn è stata caratterizzata sperimentalmente e confrontata con un materiale di riferimento in termini di microstruttura e comportamento meccanico.

La seconda parte della tesi affronta il problema della riduzione di massa attraverso l'ottimizzazione geometrica, ispirata alla struttura gerarchica porosa dello scheletro del cactus cholla. Questo approccio consente di ridurre il peso mantenendo la capacità portante, risultando particolarmente adatto per acciai ad alta densità e ricchi in cromo destinati ad ambienti ad alta temperatura e corrosivi. Sono state progettate strutture cellulari cilindriche a parete sottile mediante una metodologia bioispirata e analizzate tramite modelli analitici, simulazioni agli elementi finiti e prove sperimentali di

compressione. Le strutture sono state realizzate mediante processi di fusione e manifattura additiva, tenendo conto dei vincoli tecnologici e della scalabilità.

I risultati mostrano che l'aggiunta di alluminio consente un'efficace riduzione della densità mantenendo proprietà meccaniche specifiche favorevoli, sebbene introduca complessità microstrutturali che devono essere opportunamente controllate. Per le applicazioni in cui l'alluminio non può essere utilizzato, l'ottimizzazione geometrica bioispirata permette di migliorare significativamente il rapporto rigidezza/peso e la capacità di assorbimento di energia rispetto a cilindri cavi convenzionali a parità di volume.

Il lavoro dimostra che l'integrazione tra sviluppo di leghe avanzate e progettazione strutturale bioispirata rappresenta un approccio versatile e orientato all'applicazione per la realizzazione di componenti ad alte prestazioni e a massa ridotta, in particolare per ambienti estremi in cui la chimica del materiale è vincolata.

Parole chiave: Acciai ad alto Mn, acciai Fe–Mn–Al–C, ottimizzazione geometrica, strutture bioispirate, manifattura additiva, colata a cera persa, analisi agli elementi finiti, comportamento a compressione.

Contents

Introduction

The demand for lightweight structural materials has grown significantly in recent decades, driven by the need to improve energy efficiency, reduce emissions, and enhance performance in sectors such as transportation, construction, and power generation. Steels remain the most widely used structural materials due to their favourable balance of strength, toughness, and cost. Among them, high manganese steels are particularly attractive because of their good ductility, toughness, and work-hardening capacity, which enable them to withstand demanding mechanical and impact-loading conditions. However, their relatively high density poses a limitation for applications where weight reduction is critical.

To address this challenge, research has increasingly focused on developing strategies that reduce the weight of high manganese steels while maintaining their outstanding mechanical properties. Two main approaches have emerged:

The first involves alloy design through the incorporation of low-density elements, such as aluminium, which significantly reduces density while potentially improving oxidation and corrosion behaviour. Nevertheless, aluminium additions also introduce microstructural complexities that can influence phase stability, ductility, and processing. Understanding and optimizing these effects are important to fully exploit the benefits of aluminium alloying in high manganese steels.

However, this approach is not universally applicable. In certain environments, such as nuclear reactors, aluminium is restricted, and it requires the addition of chromium for high temperature application. In such cases, the density of high-manganese steel becomes a fixed constraint, and alternative approaches are necessary.

The second strategy draws inspiration from nature and focuses on structural design. By introducing bioinspired geometries, such as cellular, lattice, or hierarchical structures, the effective weight of components can be reduced without compromising their mechanical performance. This approach leverages advances in computational design, additive manufacturing, and materials engineering, enabling high-manganese steels to be used in lightweight architectures with optimized stiffness, strength, and energy absorption capabilities.

This thesis explores both pathways for lightweight design in high-manganese steels. Special focus is placed on the role of aluminium addition in modifying material properties and on the potential of bioinspired geometrical optimization to unlock new applications.

In detail, the following chapters are organized according to this scheme:

- Chapter 1 - Introduction of an overview on high manganese steel and the state of the art relative to low density Fe-Mn-Al-C steels and their main properties.
- Chapter 2 - Description of the materials and methods applied in the analysis that compose this work including the bio inspiration, lightweight design, structure design, numerical and experimental methods.
- Chapter 3 - Characterization of the novel alloy developed within this work and a previous alloy similar to the new one studied by other students, with focus on microstructure and mechanical features.
- Chapter 4 – Result and discussion on preliminary numerical simulations, casting process and experimental testing on real structures.
- Chapter 5 - Conclusions and final remarks on the results.
- Bibliography.

1 Overview on High Mn steel

Manganese is one of the most widely used alloying elements in steelmaking due to its relatively low cost and multifunctional benefits. At concentrations above 0.8 wt.%, manganese enhances the strength and hardness of high-carbon steels, while simultaneously improving toughness, particularly in fine-grained microstructures. In steels containing more than 10 wt.% Mn, the austenitic phase is retained after cooling, producing what is known as Hadfield manganese steel. This alloy exhibits exceptional toughness, ductility, and wear resistance, combined with a strong work-hardening capability that arises from the strain-induced transformation of austenite to martensite. These properties make manganese steel indispensable in demanding industries such as mining, construction, power generation, and railways [1].

Despite their excellent mechanical performance, manganese steels face significant challenges in terms of corrosion resistance. The high anodic dissolution rate associated with manganese compromises durability in aggressive environments, limiting their service life and applications. To overcome this drawback, extensive research has focused on alloying strategies and surface treatments that can enhance corrosion resistance without diminishing mechanical advantages. Nitrogen, as an interstitial solute, plays a critical role by stabilizing austenite, refining grain structure, and enhancing both strength and toughness. Furthermore, nitrogen additions improve resistance to localized and intergranular corrosion. Surface modification techniques, such as plasma nitriding and direct gas nitriding, have been shown to form dense nitride layers that reduce corrosion current density and suppress pitting.

Chromium is another key alloying element investigated for improving the performance of manganese steels. It increases yield strength and, in moderate concentrations, contributes to pitting resistance by enriching passivation films. However, excessive chromium promotes the precipitation of brittle secondary phases (Cr_7C_3), which undermine corrosion resistance by facilitating pitting initiation. Nevertheless, the synergistic addition of chromium and nitrogen has demonstrated promise, simultaneously enhanced corrosion resistance and stabilizing protective rust layers in marine and atmospheric conditions. Advanced characterization studies have revealed that alloying elements such as Cr and Cu not only refine corrosion product morphologies but also influence the formation and stabilization of protective oxides (Fe_3O_4, $FeCr_2O_4$), thereby improving long-term atmospheric corrosion resistance [2].

The unique deformation behavior of manganese steels also distinguishes them from conventional steels. Their outstanding strain-hardening capacity is attributed to dynamic interactions between dislocations, solute atoms, and secondary deformation mechanisms. Depending on the stacking fault energy, manganese steels can exhibit either twinning-induced plasticity (TWIP) or transformation-induced plasticity (TRIP). Both mechanisms contribute to the alloy's remarkable combination of strength and ductility, generating a "dynamic composite" microstructure during deformation. This microstructural adaptability explains the superior elongation and toughness of manganese steels compared to ferritic steels [3].

From a thermodynamic perspective, the addition of manganese to the Fe–C system profoundly alters phase equilibria. At concentrations exceeding ~13 wt.%, Mn suppresses the peritectic reaction, stabilizing austenite across a broader temperature range. The eutectoid transformation temperature is significantly reduced, extending the austenitic phase field into lower temperature regimes. With increasing manganese content, the formation of complex carbides (M_7C_3, $M_{23}C_6$) becomes more favorable, and novel Mn-rich phases (β-Mn) may emerge when Mn exceeds ~20 wt.%. These transformations underscore the critical role of manganese in tailoring the microstructural and functional behavior of steels [4].

Aluminium has emerged as an important alloying element in manganese steels. The primary benefit of aluminium addition lies in its ability to significantly reduce the density of the alloy, leading to the development of lightweight steels with high specific strength [5]. This property is particularly attractive for structural applications in transportation and energy sectors, where weight reduction directly translates into improved efficiency and performance [6]. Aluminium also contributes to corrosion resistance by promoting the formation of protective oxide films and stabilizing rust layers in certain environments. However, its addition is not without drawbacks. High aluminium contents can encourage the precipitation of brittle intermetallic phases, reduce ductility, and complicate steel processing due to increased oxidation tendencies [7]. The complex balance between these beneficial and detrimental effects necessitates a detailed understanding of aluminium's role in manganese steels. Accordingly, the next chapter of this thesis will provide an in-depth discussion of manganese steels with aluminium additions, with particular attention to their microstructural characteristics, mechanical properties, and corrosion behaviour.

1.1. Fe-Mn-Al-C steel

The development of advanced lightweight steels has gained increasing interest in recent years, particularly for applications requiring both mechanical performance and reduced mass, such as in the automotive, aerospace, and chemical industries. Among the most promising candidates are Fe–Mn–Al–C steels, which offer a significant density reduction compared to conventional steels while maintaining desirable mechanical and corrosion-resistant properties [7].

Alloying elements with lower densities than iron (Fe, 7.8 g/cm³), such as aluminium (Al, 2.7 g/cm³), silicon (Si, 2.3 g/cm³), manganese (Mn, 7.21 g/cm³), and chromium (Cr, 7.19 g/cm³), are commonly added to Fe–C steels to achieve density reduction and to influence the phase constitution of the material. The reduction in density arises not only from the inherently lower atomic masses of these elements but also from their effect on the steel's lattice parameters, which further contributes to lowering the overall mass per unit volume of the alloy [8].

The addition of aluminium plays a central role in these steel systems. Specifically, for each 1 wt.% of Al added to the alloy, the density is reduced by approximately 1.3%, enabling an overall reduction in steel density of up to 10% (~ 6.5g/cm³) when higher Al concentrations are employed, as showed in Figure 1.1. In addition to reducing density, Al also improves oxidation and corrosion resistance, making Fe–Mn–Al–C alloys potential substitutes for more expensive Fe–Cr–Ni-based stainless steels in demanding environments. These include high-temperature oxidation-resistant applications and chemically aggressive environments such as those encountered in aerospace and chemical processing industries. [9]

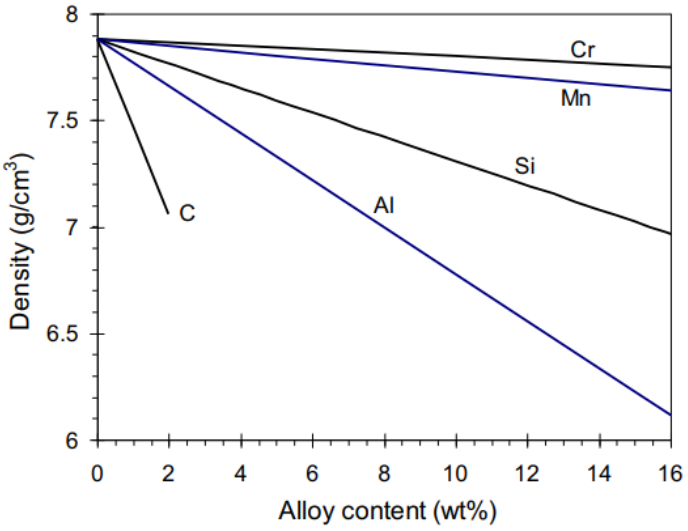

Figure 1.1 Effect of alloy elements on the density reduction of ferritic iron by elements lighter than Fe. [4]

The effectiveness of aluminium (Al) in reducing the density of steel is comparable in both ferritic and austenitic alloys, as demonstrated by the similar coefficients observed in the respective empirical Equations (1.1) for density prediction (0.098 for ferritic and 0.101 for austenitic systems). These values indicate that the addition of 1 wt.% Al leads to an approximate 1.3% decrease in density, making aluminium a reliable alloying element for achieving lightweight steel compositions.

In contrast, the influence of manganese (Mn) on density reduction is negligible, as shown in Equation (1.1). The primary role of Mn in these alloy systems is to modify the phase constitution, particularly by stabilizing the austenitic phase, rather than contributing significantly to the overall mass reduction.

From a theoretical standpoint, carbon (C) exhibits the highest potential for density reduction in austenitic low-density steels, with a calculated effect nearly four times greater than that of Al on a per-weight-percent basis. However, this potential is not fully realized in practice due to the limited solubility and typical usage levels of carbon, which rarely exceed 2 wt.% in steel alloys. In comparison, aluminium concentrations as high as 12 wt.% can be employed, making Al the more practical and impactful alloying element for density reduction in advanced steel design [10].

$$\rho_{\text{ferritic}}\ (\text{g/cm}^3) = 7.874 - 0.098\ (\text{wt\% Al})$$
$$\rho_{\text{austenitic}}\ (\text{g/cm}^3) = 8.15 - 0.101\ (\text{wt\% Al}) - 0.41\ (\text{wt\% C}) - 0.0085\ (\text{wt\% Mn}) \quad (1.1)$$

More recently, research has shifted toward exploring the potential of Fe–Mn–Al–C steels for structural applications, particularly in the automotive industry. These alloys offer a compelling combination of properties for crash-resistant and lightweight vehicle structures. However, the integration of high Al content introduces significant changes in both the physical metallurgy and mechanical behaviour of the steels. Notably, Al addition also reduces Young's modulus, with an approximate 2% decrease per 1 wt.% of Al, which must be carefully considered in structural design [4].

From a microstructural standpoint, aluminium is a strong ferrite stabilizer, while manganese and carbon act as austenite promoters. Therefore, to achieve a balanced microstructure with sufficient austenite content, which is essential for enabling deformation mechanisms such as twinning-induced plasticity (TWIP, to ensure high ductility and toughness), the alloy composition must be carefully optimized [11]. As a result, Fe–Mn–Al–C steels can exhibit a wide range of microstructures, with varying volume fractions of ferrite and austenite, depending on the specific balance of alloying elements. These microstructural characteristics, in turn, influence the overall mechanical performance and deformation behaviour of the steels, distinguishing them significantly from conventional carbon steels [12].

Table 1.1: Types of Fe-Mn-Al-C steel depending on chemical composition [4].

	Al [wt.%]	Mn [wt.%]	C [wt.%]	σ_{UTS} [MPa]	ϵ [%]
Ferritic (α)	5–9%	< 5%	<0.05%	200–600	10–40
Ferrite based duplex	3–7%	2–12%	0.05–0.5%	400–900	10–40
Austenite based duplex	5–10%	5–30%	0.4–0.7%	800–1300	10–40
Austenite (γ)	5–12%	12–30%	0.6–2.0%	800–1500	30–80

Lightweight steels exhibit a wide range of microstructures and mechanical properties, primarily governed by their chemical composition and processing history. Based on their microstructural characteristics, these steels can be broadly categorized into three classes: ferritic, duplex, and austenitic. Each category presents distinct combinations of strength and ductility, making them suitable for different structural applications.

Ferritic Steels: Ferritic based low-density steels typically contain low concentrations of manganese (Mn) and carbon (C), with Mn up to 5 wt.% and minimal carbon content. These alloys develop an elongated δ-ferrite microstructure under hot-working conditions. Depending on the aluminum content, the room temperature microstructure may consist of disordered A2-FeAl, ordered B2-FeAl, or DO_3-ordered Fe_3Al phases. These steels exhibit relatively modest mechanical properties, with ultimate tensile strength (UTS) ranging from 200 to 600 MPa and tensile elongation (TE) between 10% and 40%. The reduced strength and ductility of ferritic steels, compared to other alloy systems, limit their application in high-performance structural components [4].

Duplex Steels: Duplex lightweight steels contain intermediate levels of Mn and C, leading to a mixed-phase microstructure composed of ferrite (δ) and austenite (γ). These steels can be further subdivided based on their dominant phase. Ferrite-based duplex steels exhibit a δ + γ microstructure at hot-working temperatures, with δ-ferrite being the primary phase (volume fraction >50%). Due to the relatively low alloy content, particularly in C and Mn, the austenite phase in these steels is less stable and prone to transformation during cooling or deformation. This results in complex transformation behavior at lower temperatures, which can be influenced significantly by variations in processing parameters. Austenite-based duplex steels, by contrast, possess a γ + δ microstructure at high temperatures, where austenite forms the continuous matrix. The higher alloying content, especially Mn (12–30 wt.%), Al (up to 12 wt.%), and C (0.6–2.0 wt.%), enhances the thermal and mechanical stability of the austenitic phase. Upon cooling, austenite may remain metastable or transform depending on the conditions. These steels often exhibit κ-carbide precipitation within

the austenitic grains and intragranular κ-carbide phase, which contributes to strengthening mechanisms. Due to the presence of three main constituents: δ-ferrite, metastable austenite, and κ-carbides, these steels are often referred to as triplex steels. The mechanical properties of duplex steels vary depending on the phase balance and chemical composition. Typically, UTS values range from 400 to 900 MPa, with improved ductility compared to purely ferritic steels [4].

Austenitic Steels: Fully austenitic lightweight steels are characterized by high contents of Mn (12–30 wt.%), Al (up to 12 wt.%), and C (0.6–2.0 wt.%). These compositions promote a fully equiaxed austenitic microstructure at hot-working temperatures. Upon rapid cooling, the austenite phase remains metastable, enabling deformation mechanisms such as twinning-induced plasticity (TWIP) and transformation-induced plasticity (TRIP), which enhance ductility and strain hardening capacity. As a result, austenitic steels achieve superior mechanical performance, with UTS values ranging from 800 to 1300 MPa and tensile elongation up to 80% [4].

1.2. Phase Constitutions of Fe–Mn–Al–C Alloys

The phase diagram analysis of Fe–Mn–Al–C alloys present significant complexity due to the intricate interactions between constituent elements. In recent years, particularly over the last decade, novel phases and phase transformations have been identified within this quaternary system, indicating that a comprehensive and definitive characterization remains an ongoing challenge and may still be somewhat premature. Nevertheless, understanding the equilibrium and non-equilibrium phases of this alloy system is essential for the development and optimization of advanced materials.

1.2.1. Fe–Al alloy

Ferritic Fe–Al steels are primarily described by the binary Fe–Al phase diagram, with particular focus on the Fe-rich region due to the typical aluminium content in low-density steels being limited to below approximately 12 wt.%. Aluminium acts as a strong ferrite stabilizer, which significantly alters the phase stability by expanding the ferritic phase field and restricting the austenitic phase to a narrow loop. Within this loop, the maximum solubility of Al in face-centred cubic (FCC) γ-Fe is limited to 0.65 wt.%, rendering the alloy predominantly ferritic when the Al concentration exceeds ~1 wt.%. As a result, steels in this composition range lack transformation hardenability via an austenite-to-martensite transformation route [7].

The principal phases in the Fe-rich section of the Fe–Al system include the disordered A2 phase (α-Fe), and the ordered intermetallic phases B2 (FeAl) and DO_3 (Fe_3Al). The A2 phase corresponds to a solid solution of aluminium in body-centred cubic (BCC) α-Fe, with Al solubility reaching up to ~10 wt.% at room temperature. In this disordered structure, Fe and Al atoms are randomly distributed across the BCC lattice.

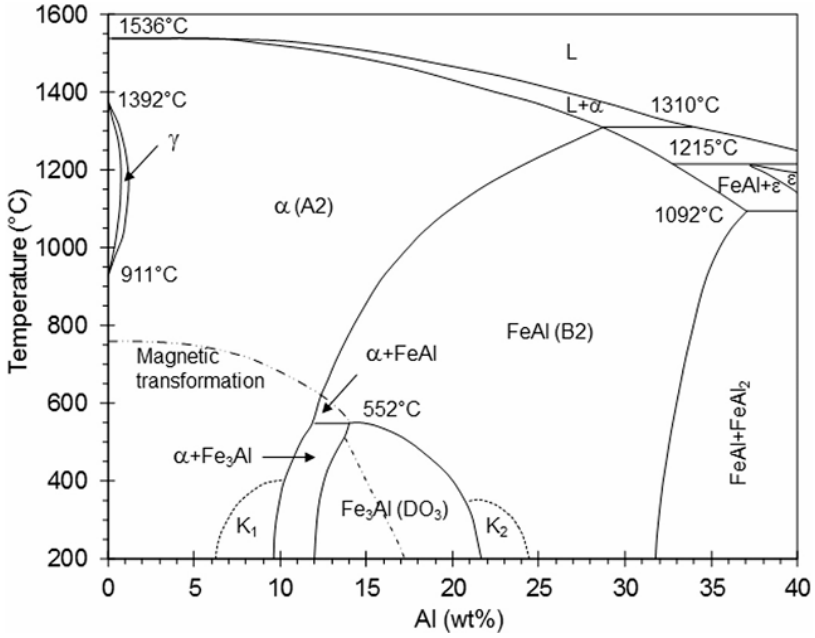

Figure 1.2 Constituents in Fe-rich part of the Fe-Al system according to Kubaschewski [13]

Upon increasing aluminium content within the range of approximately 10–32 wt.%, the ordered B2 phase (FeAl) forms through the ordering of the A2 solid solution. The B2 structure is characterized by a BCC superlattice, in which Fe and Al atoms occupy alternating lattice sites, either with Fe at the cube centre and Al at the corners, or vice versa.

The DO_3 phase (Fe_3Al) is an ordered derivative of the B2 structure, appearing at Al concentrations between 12 and 22 wt.% at room temperature. It emerges via a second-order phase transformation from the B2 phase below 552 °C. The DO_3 structure contains 16 atoms per unit cell, consisting of 12 Fe atoms and 4 Al atoms in a specific superlattice arrangement. Both B2 and DO_3 phases exhibit increased long-range order, which contributes to reduced ductility and increased brittleness at ambient temperatures.

Furthermore, two distinct phase fields, denoted as K1 and K2, are present in the Fe–Al phase diagram and correspond to what is referred to as the K-state. This intermediate state involves complex short-range ordering reactions whose precise nature remains not fully understood. The K-state has been observed in alloys containing between 6.2 and 9.6 wt.% Al at temperatures below 400 °C during cooling. The formation of K-state, along with the presence of ordered B2 and DO3 phases, adversely affects the room-temperature mechanical properties by promoting brittle fracture behaviour and limiting ductility [14].

1.2.2. Addition of Mn and Al in Fe-C system

In the Fe–C binary alloy system, the primary solid phases are ferrite (α, δ), austenite (γ), and cementite (M_3C). The introduction of manganese (Mn) into the Fe–C system induces significant changes in the phase equilibria. With increasing Mn content, the high temperature peritectic reaction progressively shifts toward lower carbon concentrations and eventually disappears entirely when the Mn content exceeds approximately 13 wt.%, as illustrated in Figure 1.3 for the Fe–15Mn–C system. Concurrently, the γ single-phase region is extended to lower temperatures.

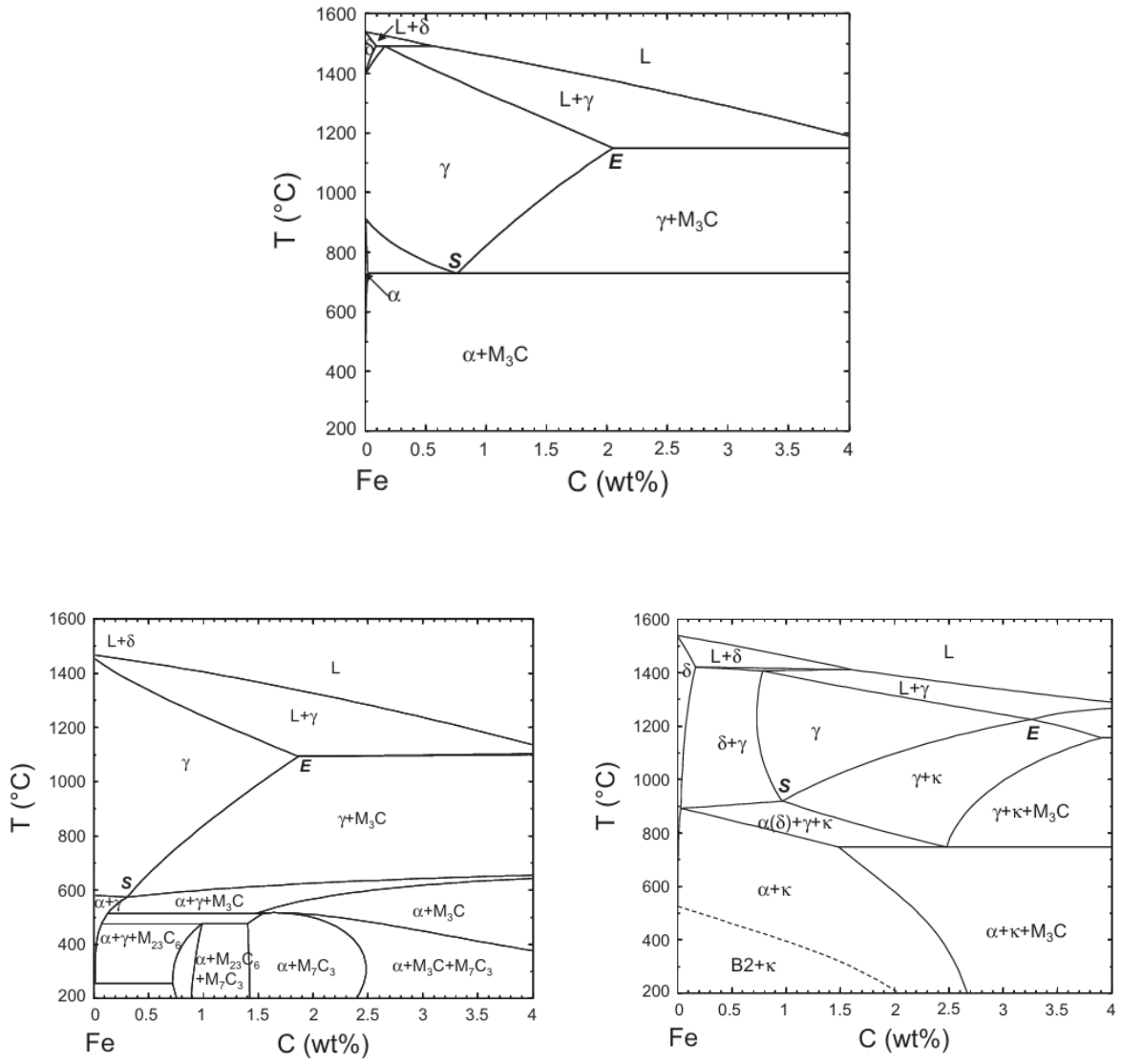

Figure 1.3 The effects of Mn and Al addition on the phase constituent and the phase fields of the Fe-C system [4]. (top) Fe-C; (left) Fe-15Mn-C; (right) Fe-7Al-C.

The eutectoid point, denoted as point S in the Fe–C phase diagram, represents the minimum temperature at which the γ phase remains stable as a single phase. Below this temperature, γ becomes metastable and undergoes decomposition into α-ferrite and carbides. The temperature and carbon concentration at point S decrease with increasing Mn content. For instance, with the addition of 30 wt.% Mn, the eutectoid temperature drops to approximately 386 °C. In contrast, the carbon concentration corresponding to point E, indicating the maximum solubility of carbon in the γ phase, is comparatively less sensitive to Mn content. In Mn-enriched Fe–C alloys, additional carbide phases such as M_7C_3 and $M_{23}C_6$ can form at lower temperatures alongside cementite (M_3C), as shown by comparing Figure 1.3 [15]. Moreover, at Mn concentrations exceeding 20 wt.%, the formation of a new intermetallic phase known as β-Mn may occur, which has a simple cubic A13 crystallographic structure and causing a significant decrease in material toughness [16].

The addition of aluminium (Al) to the Fe–C system exerts a pronounced influence on the stability and distribution of phase fields, as depicted in Figure 1.3. The compositional and temperature ranges associated with the high temperature peritectic transformation are become larger, indicating an increased potential for elemental segregation, during solidification. The (δ + γ) two-phase region is significantly expanded, while the single-phase γ region is shifted toward higher carbon concentrations and elevated temperatures. Consequently, the temperatures and carbon concentrations corresponding to points S and E are both increased. Furthermore, the (γ + M_3C) region typical of the Fe–C system is replaced by (γ + κ) and (γ + κ + M_3C) regions, where the κ phase forms as a result of Al-induced transformations [14].

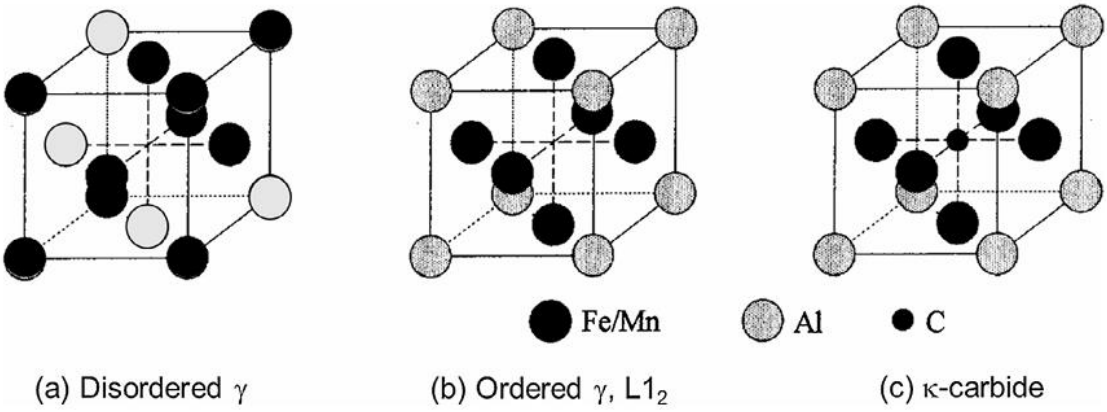

Figure 1.4 Unit cell of disordered γ (a), ordered γ ($L1_2$) (b) and κ-carbide (γ) structure in FCC alloys [17], κ-carbide is with ideal stoichiometry $(Fe,Mn)_3AlC$.

1.2.3. κ-carbide phase

One of the most significant microstructural features in Fe–Mn–Al–C steels is the formation of the κ-carbide phase. These carbides possess a perovskite-type crystal structure, designated as E21 in the Strukturbericht classification, and have an ideal stoichiometric composition of $(Fe,Mn)_3AlC$ [17]. Their presence has been extensively reported across a wide range of compositions and temperatures. In practical systems, metastable κ-carbides with non-stoichiometric compositions, generally expressed as $(Fe,Mn)_3AlC_x$ ($x < 1$), are commonly observed. These metastable carbides, sometimes referred to as κ′-carbides or $L'1_2$ structures, exhibit similar crystallographic features to the ordered $L1_2$ phase and are often associated with short-range ordering (SRO).

The κ-carbide is known to dissolve varying amounts of Mn, which enhances its stability in the Fe–Mn–Al–C system. The formation of κ-carbides has been linked to several transformation mechanisms, including discontinuous precipitation (Area 4 in Figure 1.5, DP: $\gamma \rightarrow \gamma_0 + \alpha$, where γ_0 is carbon-depleted austenite), precipitation transformation (Area 2 in Figure 1.5, PT: $\gamma \rightarrow \gamma_0 + \kappa$), cellular transformation (CT: $\gamma \rightarrow \alpha + \kappa$ or $\gamma \rightarrow \alpha + \kappa + \gamma_0$), and spinodal decomposition (Area 1 in Figure 1.5, SD: $\gamma \rightarrow \gamma' + \gamma'' \rightarrow \gamma' + \text{SRO} \rightarrow \gamma' + \kappa'$). Additionally, κ-carbides may nucleate at grain boundaries between ferrite and austenite, as shown in Area3 of Figure 1.5 (κ′-carbides) [18].

The κ-phase forms coherently with the austenitic matrix due to the close similarity in lattice structure, exhibiting a lattice parameter mismatch of approximately 3%. In contrast, its semi-coherent relationship with ferrite is characterized by a larger mismatch of nearly 6% [4]. This coherence plays a critical role in determining the mechanical behaviour of the steel, as κ-carbides can contribute to strengthening via precipitation hardening, while simultaneously acting as potential sources of embrittlement depending on their morphology, distribution, and interface characteristics [19].

The age-hardening response of Fe–Mn–Al–C steels is strongly influenced by both aluminium and carbon contents. Peak hardness is typically achieved after aging at temperatures between 500 and 550 °C. The earliest report of precipitation hardening in this alloy system is attributed to Kayak (1969) [20], who observed enhanced mechanical properties following quenching from 1150 °C and subsequent aging for 16 hours at 550 °C. This improvement was attributed to the precipitation of iron–aluminium carbides, suspected at the time to have an $L1_2$-ordered structure. Later investigations by Han et al. [21], confirmed that the κ-carbide possesses an ordered $L'1_2$ crystal structure, equivalent to the $E2_1$ perovskite type. In this structure, aluminium atoms occupy the cube corners, Fe and Mn atoms are located at face-centred positions, and carbon atoms are positioned at the centre of the unit cell in octahedral interstitial sites.

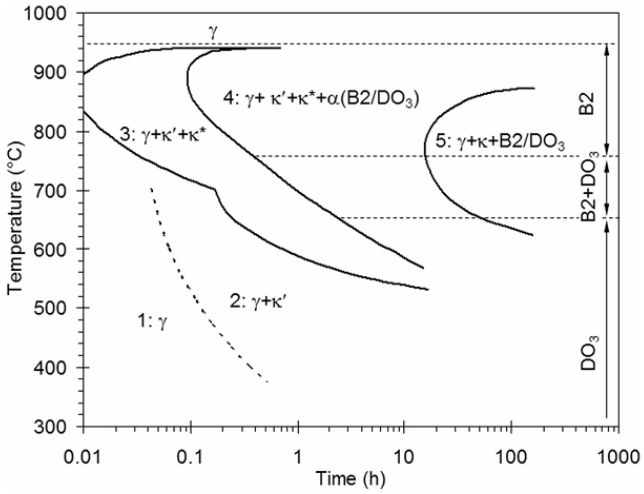

Figure 1.5 TTT diagram of decomposition of c-solid solution in a Fe-28Mn-8.5Al-1C-1.25Si alloy during isothermal aging [22].

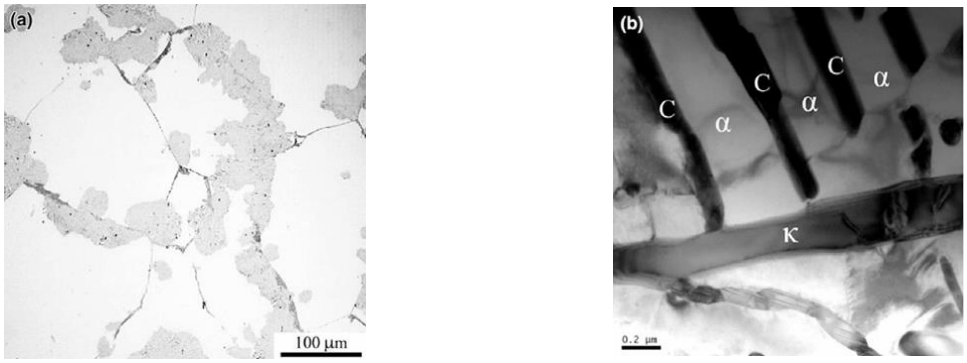

Figure 1.6 Microstructures of a Fe-13.5Mn-6.3Al-0.78C steel after solution treatment at 1000°C followed by aging at 600°C for 100h [23]; (a) optical microscope image showing large κ-pearlite colonies along the austenite grain boundaries; (b) internal portions of various κ-pearlites. C indicates $M_{23}C_6$.

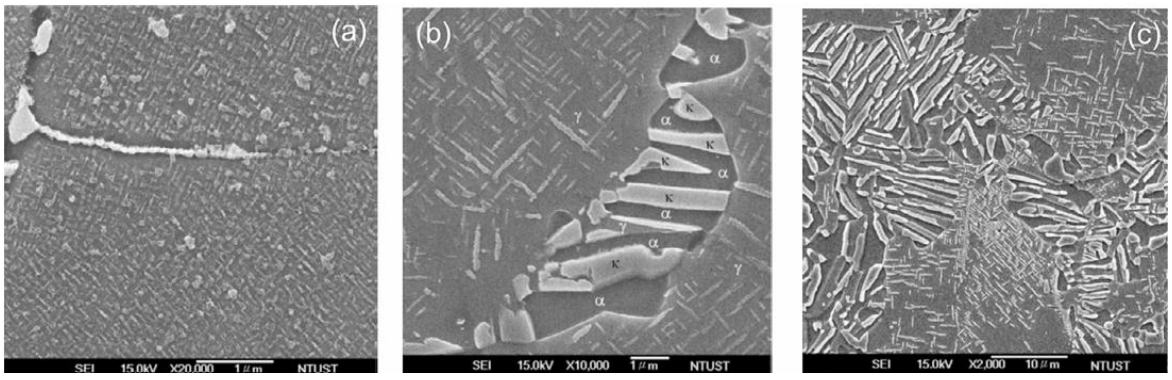

Figure 1.7 Growing feature of κ'-carbides in a Fe-18Mn-7Al-0.85C austenitic steel [24] for periods of time: (a) 1h, (b) 25h, (c) 100h.

1.3. Processing in Fe-Mn-Al-C alloys

The processing of Fe–Mn–Al–C lightweight steels presents both significant opportunities and complex challenges, particularly in terms of phase stability, hot workability, and microstructural control. The austenitic (γ) phase in these steels is not inherently thermally stable at lower temperatures. Nevertheless, the presence of elevated concentrations of manganese and carbon can stabilize the γ-phase, enabling its retention at room temperature. While thermodynamic models allow accurate predictions of equilibrium phase compositions at elevated temperatures, such as during hot working, the actual phase evolution at lower temperatures often deviates from these predictions due to sluggish diffusion kinetics and insufficient driving force for martensitic transformations, unlike in conventional carbon steels [25].

In laboratory-scale research, achieving a homogeneous microstructure in small cast ingots is relatively manageable. However, industrial-scale production introduces complications such as segregation of alloying elements, temperature gradients, and non-uniform heat flux during casting and hot deformation, often leading to cracking and other processing defects. Homogenization of as-cast ingots is typically conducted at 1100–1250 °C for 1–3 hours to alleviate chemical segregation before hot rolling. The slabs are then hot rolled to a final thickness of 2–5 mm at finishing temperatures between 850 and 1000 °C. To reduce cracking risks during deformation, intermediate reheating may be applied between rolling passes.

In practice, hot working of Fe–Mn–Al–C steels are particularly sensitive to thermal and mechanical conditions. The formation of intergranular κ-carbides and the emergence of a banded structure during hot deformation are key factors that deteriorate hot workability. The κ-carbide precipitates can form along grain boundaries if the cooling rate after hot rolling is insufficiently high. Therefore, fast cooling followed by either slow cooling (process 1 in Figure 1.8) or isothermal holding (process 2 in Figure 1.8) is recommended to suppress undesirable precipitation and promote fine-scale, dispersed κ-carbides. Alternatively, isothermal annealing after direct cooling to room temperature can be employed to control precipitation behaviour [26].

Austenitic-based low-density steels can also be produced via cold rolling routes. For age-hardenable grades, cold rolled sheets are solution treated in the single-phase austenite region (900–1100 °C), followed by rapid quenching (process 3 in Figure 1.8). Subsequent aging treatments, typically conducted at 500–700 °C for durations of 5–20 hours, induce precipitation of the metastable κ′ phase, enhancing mechanical strength via precipitation hardening (processes 4 and 5 in Figure 1.8) [27]. Different process variants exist, including direct aging, isothermal aging, or multi-stage aging sequences, each tailored to maximize the strengthening contribution of fine κ-carbide particles.

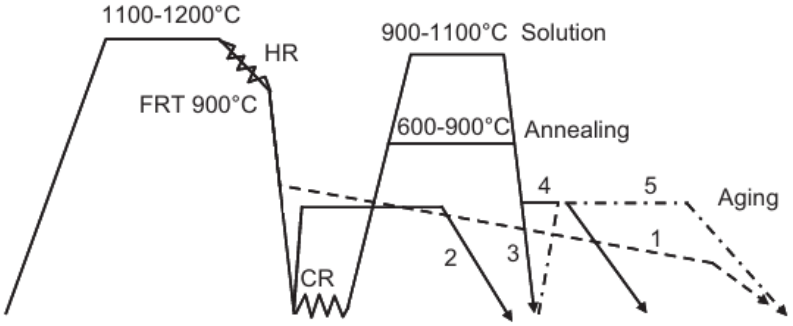

Figure 1.8 Austenitic Fe-Mn-Al-C steel production processes [9].

In contrast, non-age-hardenable austenitic alloys may undergo short-time annealing (1–5 minutes at 600–900 °C) after cold rolling to restore ductility through recovery or recrystallization [28].

For ferritic and ferrite-based duplex steels, conventional hot rolling schedules used in carbon steels are generally unsuitable due to the excessive grain growth and elongation of δ-ferrite during deformation. Consequently, such steels are usually processed by cold rolling followed by recrystallization annealing at 700–1000 °C to refine the ferritic grain structure and induce κ-carbide precipitation [29].

Duplex grades with austenite-dominant microstructures are typically annealed in the intercritical temperature range (700–900 °C) and then austempered to balance the phase fractions and optimize mechanical properties. Ferritic phase, with body-centred cubic (BCC) structures and high stacking fault energy (SFE), favour dislocation climb and cross-slip, promoting continuous dynamic recovery. Austenitic phase, characterized by face-centred cubic (FCC) lattices and lower SFE, exhibit dynamic recrystallization once a critical strain or energy threshold is met due to limited dislocation mobility. In duplex steels, strain incompatibility between ferrite and austenite induces interfacial sliding, which is resisted by semi-coherent interfaces formed according to the Kurdjumov–Sachs orientation relationship. This interface strengthens the material but must be overcome during plastic deformation. Over prolonged deformation, this orientation relationship degrades, reducing the interfacial resistance [30].

Efforts to improve hot ductility and process reliability in Fe–Mn–Al–C steels include adjusting the Al content to control hardenability, employing higher finish rolling temperatures, minimizing central segregation during casting, and reducing variability in thermal mechanical histories [31]. These measures aim to reduce edge cracking, transverse fractures, and other processing defects that compromise productivity and component integrity.

1.4. Mechanical behaviour of Fe-Mn-Al-C alloys

Lightweight steels based on Fe–Mn–Al–C systems exhibit a wide range of mechanical properties, such as yield strength, ductility, hardness, and ultimate tensile strength, which can be engineered through a combination of alloy design, microstructural control, and thermomechanical processing. These steels are broadly categorized based on their matrix structure. Ferritic lightweight steels, typically compared with High-Strength Low-Alloy (HSLA) and High-Strength Steels (HSS), exhibit enhanced strength but reduced ductility with increasing aluminium content. On the other hand, austenitic lightweight steels, closely aligned with Advanced High-Strength Steels (AHSS), display mechanical behaviour ranging between that of Transformation-Induced Plasticity (TRIP) and Twinning-Induced Plasticity (TWIP) steels, with higher ductility and work hardening capacity, as shown in Figure 1.9 [4].

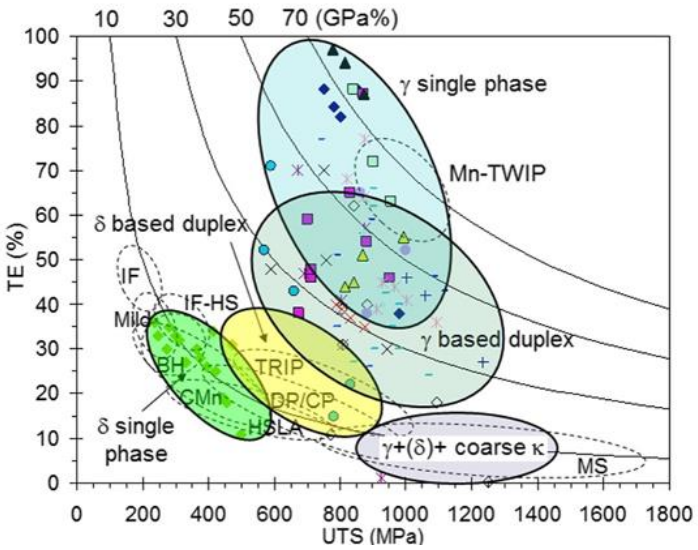

Figure 1.9 Plot of total elongation vs ultimate tensile strength in Fe-Mn-Al-C alloys.

1.4.1. Strengthening mechanisms

Solid Solution Strengthening: In both ferritic and austenitic matrices, solid solution strengthening plays a fundamental role. In ferritic low-density steels, aluminium is the primary alloying element, contributing approximately 40 MPa increase in yield strength per weight percent of Al due to its size misfit and associated lattice distortion. The mechanical behaviour of Fe–Al ferritic alloys demonstrate a continuous strength increase up to ~13 wt.% Al, after which a sharp decrease is observed in the 13–15 wt.% range. This transition corresponds to the formation of long-range ordered superlattices (DO_3 and B2 phases), which introduce brittleness and suppress ductility. For practical

applications, especially in automotive structural components, Al content is commonly limited to 7–9 wt.% to balance strength and ductility [32]. Additional alloying with interstitials such as nitrogen (<30 ppm), and substitutional elements like silicon (<0.3 wt.%), can further enhance mechanical performance. Moreover, microalloying elements such as Ti, Nb, V, and B (in concentrations below 0.1 wt.%) can refine grain structure, enhancing strength via the Hall–Petch relationship [33].

In austenitic Fe–Mn–Al–C steels, carbon provides the most potent solid solution strengthening effect, increasing yield strength by 187–300 MPa per wt.% C, while manganese and aluminium offer more moderate contributions. The effect of manganese is composition-dependent and influenced by the Al content. Al additions typically enhance strength at the cost of ductility across ferritic, austenitic, and duplex microstructures [34].

Precipitation Hardening: Precipitation strengthening in Fe–Mn–Al–C steels is primarily attributed to the formation of nanoscale κ-carbides, which are coherent or semi-coherent with the austenitic matrix and impede dislocation motion. These precipitates are especially effective in highly alloyed compositions, where they are homogeneously dispersed and stabilized under specific aging treatments. Their presence contributes significantly to mechanical strength [35]. In duplex alloys, α-ferrite can precipitate within the austenitic matrix and may transform into intermetallic B2 or DO_3 phases under specific thermal histories, further enhancing strength while promoting ultrafine-grained microstructures [36].

Deformation Mechanisms: The mechanical behaviour of Fe–Mn–Al–C steels are also governed by a variety of deformation mechanisms, including dislocation glide, mechanical twinning (TWIP), transformation-induced plasticity (TRIP), microband-induced plasticity (MBIP), dynamic slip band refinement (DSBR), and shear-band-induced plasticity (SIP). The activation of these mechanisms depends critically on the stacking fault energy (SFE), which is primarily determined by alloy composition—particularly the concentrations of Al and C.

Prior to analysing these mechanisms, it is essential to precisely define the concept of SFE. Stacking fault energy refers to the energy difference between a defect-free face-centred cubic (FCC) crystal and a crystal containing disruptions in its stacking sequence. In an ideal FCC crystal structure, the atomic planes are arranged in a close-packed {111} sequence following an ABCABCABC... stacking order (Figure 1.10). However, under realistic conditions—either due to plastic deformation or phenomena occurring during the solidification process—this ideal FCC stacking sequence is often not maintained. Localized interruptions involving one or more atomic layers can disrupt the regular stacking pattern, leading to the formation of stacking faults [37].

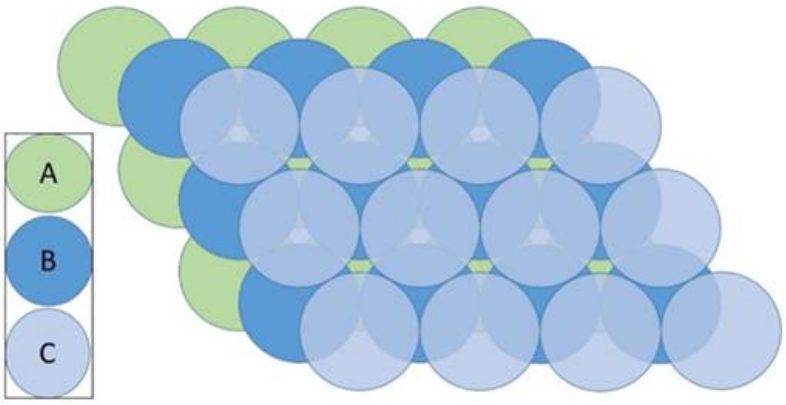

Figure 1.10 Schematic representation of the stacking sequence of a perfect (fcc) structure.

In steels with low Al content (<6 wt.%), SFE is low enough to promote mechanical twinning, resulting in high work hardening rates and ductility. In contrast, higher Al concentrations increase SFE, suppressing twinning and promoting planar dislocation glide as the dominant deformation mode. At high SFE, alternative mechanisms such as MBIP, DSBR, and SIP become active, particularly under high strain rates or complex loading paths [38].

The mechanical stability of austenite, which is predominantly determined by its stacking fault energy, critically influences the activation of deformation mechanisms such as deformation-induced phase transformations, twinning, or dislocation slip. Specifically, the magnitude of the SFE governs the ease with which austenite (γ-phase) transforms into ε-martensite or α'-martensite under applied stress or alternatively undergoes mechanical twinning or slip deformation [37].

Table 1.2: Deformation mechanisms in austenitic Fe-Mn-Al-C as a function of SFE.

SFE (mJ/m^2)	Main deformation mechanism
< 20	TRIP + dislocation glide
20-40	TWIP + dislocation glide
40-60	Cross-slip and activation of slip systems
> 60	MBIP or DSBR or SIP

TRIP, characterized by the stress-assisted $\gamma \rightarrow \varepsilon$ martensitic transformation, typically occurs in steels exhibiting SFEs lower than approximately 20 mJ/m². In contrast, TWIP becomes the dominant mechanism in alloys with intermediate SFEs ranging between 20 and 40 mJ/m². At higher SFE values, generally exceeding 40 mJ/m², deformation is primarily accommodated through the motion of partial or perfect dislocations. For SFEs greater than 60 mJ/m², MBIP tends to dominate the strain accommodation, and more recently, DSBR mechanism has also been reported in steels within this SFE regime [37].

Transformation-Induced Plasticity (TRIP): In steels where the SFE is low, the metastable austenitic phase tends to undergo a stress-assisted phase transformation into ε-martensite once a critical strain threshold is exceeded under tensile loading. This transformation enhances mechanical strength due to the inherently higher strength of martensite relative to austenite and contributes to grain refinement. Furthermore, the progressive formation of martensitic phases elevates the work-hardening rate, thereby improving uniform elongation [39].

Twinning-Induced Plasticity (TWIP): For intermediate SFE values, typically ranging between 20 and 40 mJ/m², plastic deformation is predominantly governed by mechanical twinning. Under increasing tensile strain, specific crystallographic orientations within the austenite matrix initiate the formation of deformation twins and their intersections, which act to subdivide and refine the austenite grains. This dynamic refinement introduces additional barriers to dislocation motion, leading to an increase in both strength and ductility. While TWIP primarily enhances ductility through the formation of twin boundaries, it also contributes to strength by impeding dislocation glide [39].

Shear-Induced Plasticity (SIP): At high SFE values, shear band formation becomes a dominant deformation mechanism. These bands are narrow regions of intense localized shear strain that arise during plastic deformation. The generation of shear bands is associated with the accumulation of dislocations at interfaces such as κ-carbides, where dislocations must overcome obstacles through shear-driven processes [40]. SIP contributes to both the ultimate tensile strength and ductility of the material by promoting localized strain accommodation and enhancing strain hardening.

Microband-Induced Plasticity (MBIP): When the SFE is elevated, the formation of microbands, localized regions of intense plastic deformation, becomes prominent. As strain progresses, dislocation density increases significantly, and these dislocations begin to self-organize into higher-order structures. This collective evolution of dislocation structures gives rise to microband-induced plasticity, which facilitates strain accommodation while maintaining high work-hardening rates [40]. The MBIP mechanism is particularly effective in achieving a favourable balance between strength and ductility.

Dynamic Slip Band Refinement (DSBR): it is a deformation mechanism that occurs in steels with high SFE values. It involves the progressive subdivision of grains due to the repeated activation and refinement of slip bands during plastic deformation. These slip bands evolve dynamically, becoming narrower and more densely spaced as deformation continues, effectively increasing the number of internal barriers to dislocation motion. The DSBR effect enhances mechanical properties by refining the slip structure within grains, thereby contributing to a simultaneous increase in both strength and ductility through continuous strain hardening [41].

1.4.2. Tensile properties

The tensile behaviour of Fe–Mn–Al–C-based lightweight alloys, is influenced by alloy composition, processing route, and specimen geometry. A wide range of tensile properties has been reported for these alloys, with significant variation in total elongation (TE) values across the literature. The tensile properties also depend on surface conditions, particularly in hot-rolled strip samples. Depending on the heat treatment, such as solution treatment and quenching, these steels demonstrate a broad spectrum of mechanical responses. Property maps plotting UTS against TE in Figure 1.9 indicate that the tensile behaviour of Fe–Al ferritic steels is comparable to that of conventional low-alloy C–Mn and high-strength low-alloy (HSLA) steels. Ferrite-based duplex alloys fall near the upper bound of first-generation advanced high-strength steels, while single-phase austenitic Fe–Mn–Al–C alloys occupy a similar region to Mn-based TWIP steels but with broader property distribution.

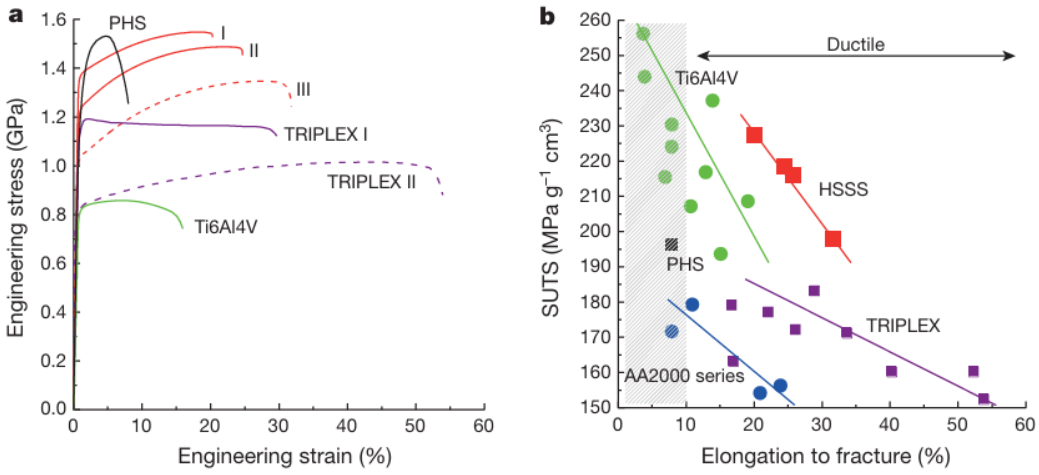

Figure 1.11 Tensile properties of Fe–Mn–Al–C alloys (TRIPLEX) compared with selected metallic alloys of high specific strength: a) Engineering stress–strain curves of κ-carbide strengthened TRIPLEX steels compared with the annealed HSSS (I–III), a commercial titanium alloy and a fully martensitic press hardening steel (PHS). b) plot of specific ultimate tensile strength (SUTS)versus elongation to fracture [42].

Material	Chemical composition, weight%										
	Fe	C	Si	Mn	Al	Ti	Nb	V	Cr	Ni	B
HSSS	Bal.	0.86	0.02	16.1	9.6	0.042	0.004	-	-	4.9	-
PHS	Bal.	0.22	0.24	1.2	-	0.04	-	-	0.2	-	0.0022
Ti6Al4V	0.12	0.01	-	-	6.1	Bal.	-	3.9	-	-	-
TRIPLEX I	Bal.	1.8	-	20	11	-	-	-	5	-	-
TRIPLEX II	Bal.	1.0	-	28	12	-	-	-	-	-	-

Figure 1.12 Composition of materials presented in Figure 1.11

In terms of specific mechanical performance, Figure 1.11a presents a comparison of room-temperature tensile properties for Fe–Mn–Al–C alloys and various other metallic systems with high specific strength. Figure 1.11a displays stress–strain curves for alloys subjected to different annealing conditions, alongside reference materials such as the commercial titanium alloy Ti-6Al-4V and fully martensitic press-hardened boron steel. The flow curves exhibit exceptionally high strain hardening even at yield strengths surpassing 1 GPa, while maintaining substantial ductility, especially for the Fe–Mn–Al–C alloy with the addition of Nichel, called high-specific-strength steels (HSSS). Figure 1.11b illustrates the relationship between specific ultimate tensile strength (SUTS) and elongation to fracture, highlighting the outstanding combination of specific strength and ductility achieved by this alloy in comparison to other high-performance alloys [42].

1.4.3. Corrosion

As discussed earlier, Fe–Mn–Al–C alloys have been investigated as potential alternatives to stainless steels, with the goal of achieving comparable properties at a lower cost. Zambrano [37] reviewed several studies on their electrochemical behaviour, showing that although Fe–Mn–Al–C steels exhibit inferior corrosion resistance compared to stainless steels, their corrosion current densities in seawater environments are markedly lower than those of conventional carbon steels.

Alloying composition strongly influences corrosion performance. Increased aluminium content improves alloy nobility, whereas higher manganese content reduces it. Aging treatments reduced corrosion resistance compared to solution-treated conditions, and austenitic microstructures demonstrated superior resistance relative to duplex counterparts [37].

2 Materials and methods

This chapter outlines the materials investigated and the methodologies employed throughout the course of this study. A novel alloy system was selected and subjected to a comprehensive set of analyses aimed at evaluating its fundamental characteristics. This work including also the application of the novel alloy in a bio inspired structure, followed by its production process and structural testing.

The chapter is structured to present the employed techniques in a systematic manner. It begins with the lightweight approach and the bio-inspirational approach for structure design, followed by a description of the analytical methods with discussion of the numerical and experimental approaches.

2.1. Lightweight design

Even before people fully understood how to calculate stress or design for different kinds of forces, they were already building amazing structures to make life better—like bridges, buildings, and vehicles. These early designs were based mostly on trial and error and were often heavy and overbuilt. That's because engineers didn't yet have the tools or knowledge to make things both strong and light at the same time.

This changed with the rise of lightweight design. This is the idea of building parts, products, or entire structures to be as light as possible, while still being strong and safe. It's about finding the best balance—using less material without losing performance.

Designing for lightweight performance necessitates a constraint driven methodology. Constraints are essential not only for preserving functional integrity but also for avoiding misleading strategies, such as eliminating safety systems purely to save mass.

A valid lightweight design must satisfy multiple concurrent requirements:

- **Mechanical constraints**: Ensuring structural integrity under static and dynamic loading conditions, including fatigue, buckling, and impact resistance.
- **Economic constraints**: Material and manufacturing costs must be viable for the intended application. For instance, high-cost materials such as carbon fiber composites may be justified in motorsports or aerospace but are often economically infeasible for mass-produced consumer products.

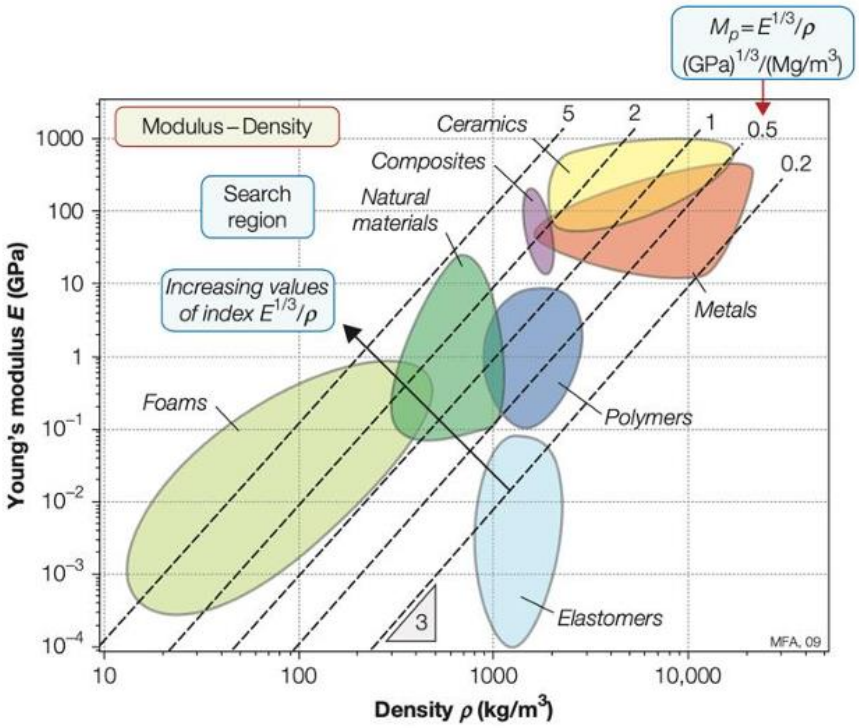

Figure 2. Material selection charts

- **Temporal constraints**: Engineering schedules influence the level of design refinement. Often, suboptimal mass efficiency is tolerated due to tight development timelines.
- **Regulatory constraints**: Legal and industry standards impose minimum safety or environmental requirements, which may restrict material or process selection.

Applications of lightweight design span virtually every engineering field. In the automotive sector, reducing a vehicle's curb weight enhances fuel efficiency, acceleration, and handling. As highlighted by Tempelman [43], a 10% reduction in vehicle weight can yield a 5–7% improvement in fuel economy, depending on the powertrain and use case. Similar principles apply in aerospace, civil engineering, and high-rise architecture, where the self-weight of the structure plays a dominant role in determining feasibility.

To achieve lightweight solutions, two complementary design strategies are employed:

1. **Material Selection**

The selection of materials with high specific properties, properties normalized by density, is fundamental. Pioneering work by Ashby [44] introduced *material selection charts* that graphically represent material families based on combinations of properties such as Young's modulus, yield strength, fracture toughness, and density.

Straight dashed lines in the charts (Figure 2) represent material indices (performance metrics). Optimal materials lie toward the upper-right region of the graph, maximizing performance per unit mass.

In the context of this thesis, lightweight high-strength steels, such as advanced high-strength steels (AHSS), transformation induced plasticity steels (TRIP) or especially Fe–Mn–Al–C alloys (TRIPLEX), are emphasized for their superior mechanical efficiency and high stiffness to weight ratio, exactly what is intended in lightweight design.

2. **Geometric Optimization**

Even the best material won't help if the shape of the structure is inefficient. The structural configuration is equally important. As Ashby and others have emphasized, optimal cross-sectional profiles can vastly improve load-bearing capacity without increasing mass.

Geometric optimization can be categorized into three strategies:

- Topology optimization
- Sizing optimization
- Shape optimization

This thesis explores shape driven optimization through bioinspired structural morphology, specifically drawing inspiration from the cactus skeleton.

By integrating lightweight materials with geometrically efficient, lightweight shapes, it is possible to create innovative structural designs that offer improved strength-to-weight performance, enhanced efficiency, and practical applicability. Achieving this synergy is the central objective of the research presented in this thesis.

2.2. Bioinspired design

To address the structural limitations inherent in conventional engineering designs, bioinspiration has emerged as a viable and innovative strategy. Researchers have introduced a systematic, problem-driven methodology to guide the integration of biological principles into engineering applications. This approach is structured into two main phases, each comprising four distinct steps, as illustrated in Figure 2.1. The complete process, composed of eight stages, leverages a set of analytical and design tools detailed in existing literature and standardized methodologies [45]. The bioinspired design pathway proposed by the authors has been adapted to suit the objectives of this thesis, as outlined below:

1) **Problem Definition**: Identification of the need to improve the physical and mechanical performance, specifically the weight and compressive behaviour, of hollow cylindrical structures, which are widely used yet exhibit room for enhancement.
2) **Functional Abstraction**: Translation of the engineering problem into structural requirements, focusing on increasing stiffness on weight ratio, and optimizing maximum displacement and load-bearing capacity under quasi-static compressive loading.
3) **Biological Transfer**: Exploration of how natural systems withstand similar mechanical stresses, emphasizing structural adaptations found in biological organisms subjected to compressive forces.
4) **Selection of Biological Analogues**: Screening of relevant biological models that exhibit favourable mechanical characteristics. Prominent example is the Cholla cactus frames which display optimized load-bearing features.
5) **Evaluation and Selection of Bioinspired Models**: Among the identified biological templates, a subset is selected based on compatibility with the mechanical objectives and feasibility for further modelling and testing.
6) **Extraction of Structural Principles**: Analysis and abstraction of the underlying biological strategies, with the aim of identifying functional features that can be adapted to meet the defined engineering problem.
7) **Technological Translation**: Assessment of the practicality of implementing the extracted biological strategies using current manufacturing processes and materials, including considerations of scalability and cost-effectiveness.
8) **Application and Validation**: Implementation of the bioinspired concepts within the original engineering context through a combination of numerical simulations and experimental investigations.

While several of these stages have been addressed in previous sections, the following part of this chapter focuses specifically on the natural model selected and utilized in the development of this work. A detailed analysis of their structural characteristics and relevance to the engineering objectives is presented herein.

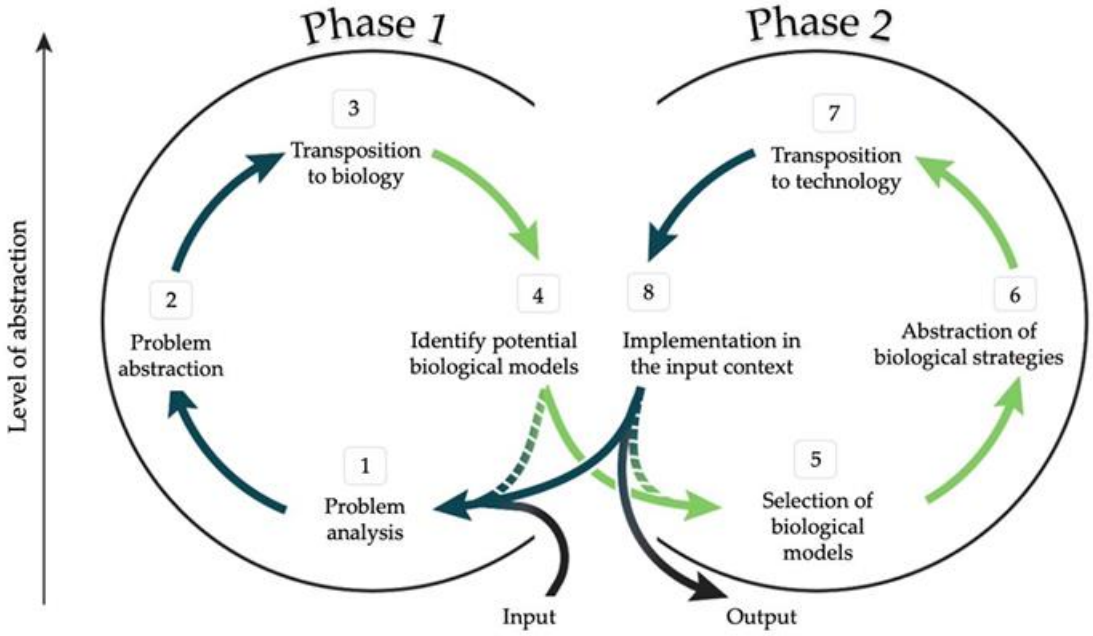

Figure 2.1 Bioinspired design pathway

2.2.1. Bio inspirational sources

In the arid landscapes of the southwestern United States and northern Mexico, one encounters the structural remnants of cholla cactus (genus Cylindropuntia), characterized by intricate lattices of hollow cylindrical wood. These skeletal structures, visible in mature or deceased plants (Figure 2.2), are the lignified remains of the cactus's vascular architecture. Ranging in form from shrub-like to specimens reaching heights of approximately 4.6 meters, cholla cacti possess extensive cylindrical branches that, upon desiccation and decay of softer tissues, reveal a porous, load-bearing wood scaffold [46].

Figure 2.2 Cholla cactus (above) and its wood skeletons (below)

These wooden "skeletons" consist of hierarchically porous, hollow cylinders formed through the activity of the vascular cambium, a meristematic growth layer that generates xylem on the internal surface and phloem on the external surface. The xylem comprises secondary cell walls that are rich in lignin, a highly cross-linked biopolymer known for its high compressive stiffness but inherent brittleness [47]. The mechanical integrity of the skeleton under compressive loads is primarily attributed to this lignified xylem matrix. It not only facilitates fluid but also functions as a stiff load-bearing framework capable of resisting axial compressive forces.

During growth, the cactus develops a reticulated network of vascular bundles embedded within a matrix of soft, unlignified parenchyma cells. Over time, these bundles and the interconnecting bridges undergo lignification, resulting in the rigid porous wood structure observed in mature cholla. The parenchymatous regions

between the vascular bundles remain largely unlignified, creating large, centimetre-scale voids that persist as through-holes in the skeleton. These perforations, while biologically associated with water retention in the fleshy tubercles (protrusions tipped with spines), also play a structural role: they reduce weight without significantly compromising the compressive performance of the overall structure, thereby optimizing the strength-to-weight ratio, a desirable characteristic in natural and engineered cellular solids [48].

A fully developed cholla cactus can reach a mass between 50 and 150 kilograms, while exceptionally large specimens may exceed 200 kilograms. In contrast, the residual wooden skeleton represents only a small fraction of the original mass, highlighting the considerable mechanical strength, particularly under compressive loading conditions, of these skeletal structures. This favourable combination of low weight and adequate load-bearing capacity demonstrates the mechanical efficiency of the structure, offering an excellent example of natural optimization in terms of material usage and structural functionality [48].

Similar structural principles are evident in the giant cardon cactus (*Pachycereus pringlei*), one of the largest cactus species. The cardon achieves larger heights and masses than cholla cactus and yet maintains structural integrity through a robust internal woody skeleton. This skeletal framework, composed of relatively weak material, provides exceptional resistance to self-weight-induced buckling and deformation. Its design allows the cactus to withstand both gravitational and environmental stresses, further highlighting nature's ingenuity in developing lightweight yet mechanically resilient structures.

In species such as Cylindropuntia leptocaulis, the perforations are elongated (Figure 2.2, left), whereas in species with broader tubercles, the holes tend toward a circular morphology (Figure 2.2, right). These geometric variations influence local stress distributions under compressive loading. While botanical studies have postulated functions related to spine packing efficiency or thermal regulation [49], from a mechanical standpoint, finding the pore arrangement and overall architecture, which confer enhanced structural resilience by distributing compressive stresses and mitigating crack propagation through stress redirection around the holes, is an important feature for lightweight structures such as hollow cylindrical beams.

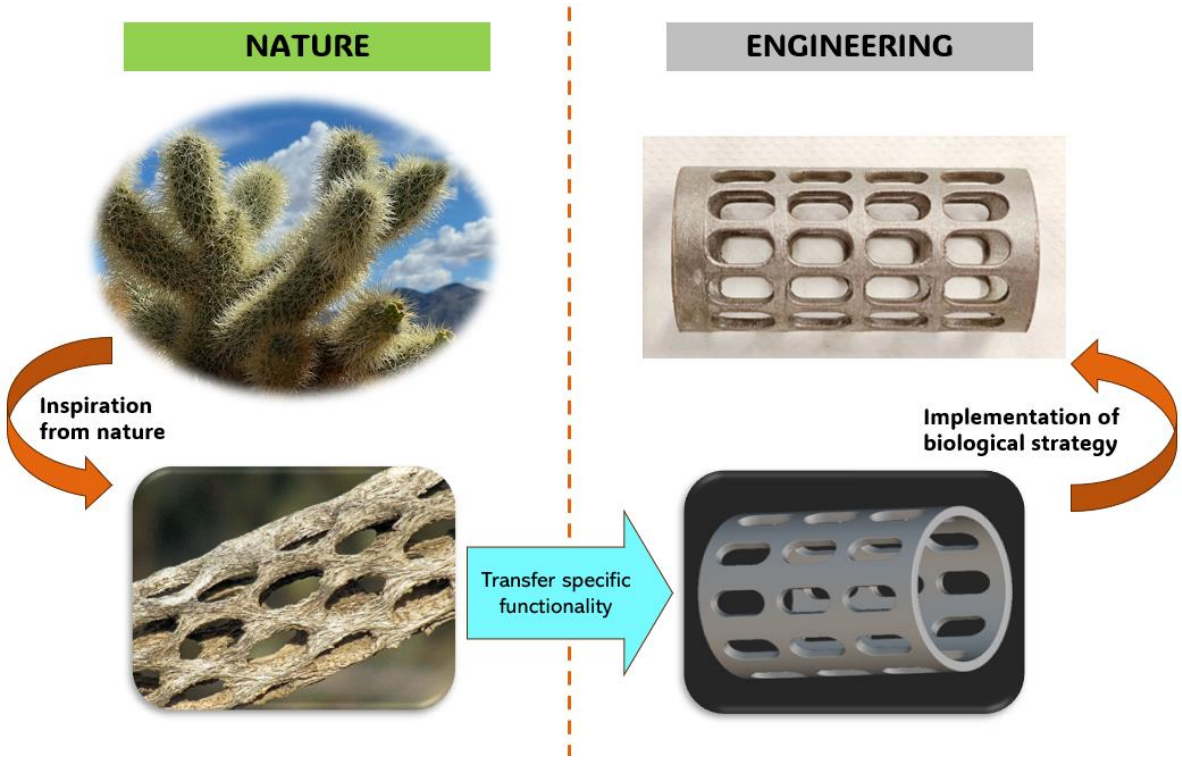

Figure 2.3 Overview of the implemented bio-inspired approach, the inspiration derives from Cholla cactus skeleton for its lightweight arrangement and good mechanical capacity.

2.2.2. Critical aspects

The field of bioinspired design is experiencing rapid advancement, driven by its promising potential and the wide diversity of natural models available for engineering applications. Despite this growth, several critical issues remain. A substantial portion of recent research has focused on investigating the mechanical behaviour of bioinspired structures under various loading conditions. However, these studies often lack direct comparisons with existing engineering structures, which may offer similar or superior performance with simpler and more cost-effective fabrication processes. Other studies have adopted a different approach by integrating bioinspired features into conventional structural geometries, such as hollow tubes, beams, and shells, to evaluate the extent to which specific mechanical properties can be enhanced. These investigations typically compare the modified structure to the original baseline geometry, quantifying both the percentage improvement in performance (e.g., stiffness, strength, or energy absorption) and the corresponding change in volume or mass due to the added features.

In this thesis work, particular emphasis is placed on a more stringent and engineering-relevant comparison: the mechanical performance of the designed bioinspired structures is evaluated against that of a hollow cylindrical shell possessing the same volume. The objective is to demonstrate structural improvements without increasing the overall volume or weight, a criterion that aligns more closely with the principles of lightweight design and structural efficiency. Although this constraint is more restrictive, it provides a clearer and more meaningful benchmark for applications where mass minimization is critical.

Another significant challenge in the application of bioinspired design lies in the limitations of manufacturing technologies. Nature often inspires highly complex geometries and hierarchical features that are not easily reproduced using conventional manufacturing methods. For example, in the case of cylindrical components, several established production techniques are available depending on the required volume and performance: seamless tubing, extrusion, electric resistance welding. However, the integration of intricate bioinspired features into cylindrical walls may significantly complicate the manufacturing process, often necessitating the adoption of additive manufacturing techniques such as 3D printing.

In this thesis work, the bio inspired structures will be created with a novel Fe-Mn-Mg-C alloy using casting process, so too small and complex features will be unfeasible due to the manufacturing constraint, influencing also the scalability (downward) of the structure. One solution to this limitation maybe the creation of metal powder with the same alloy composition and build the component using powder bed fusion (PBF) technology which is more precise, suitable for relatively complex structures and small features.

2.3. Design of the structures

The objective of the design phase is the development of thin-walled cylindrical cellular structures based on a biomimetic methodology, aiming to enhance both weight reduction and compressive performance in comparison to conventional thin-walled cylinders. Among various botanical sources, the internal skeleton of the Cholla cactus was selected as the primary natural model due to its structurally efficient porous architecture. A comprehensive discussion of the biological inspiration underpinning the design is provided in the preceding section.

The following sections detail the design and dimensional specification of the bioinspired structures. The design process begins with configurations featuring uniformly distributed pores and progresses toward more advanced architectures incorporating alternating pore arrangements and tilted pore orientations. All geometrical modelling and structural generation were performed using the Ntopology software platform, which offers robust tools for the creation and manipulation of complex lattice and cellular geometries.

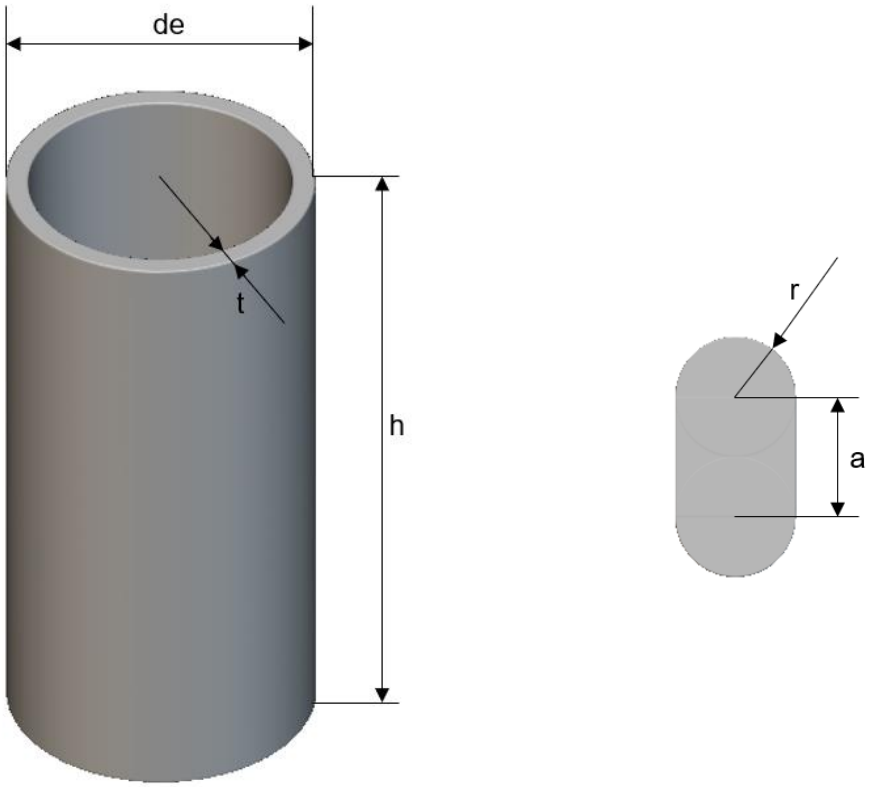

Figure 2.4 Reference hollow cylindrical structure (left); linear slot shape (right)

The design parameters are:

- cylinder height, ***h***
- cylinder external diameter, ***de***
- cylinder wall thickness, ***t***
- pore radius, ***r***
- centre-to-centre distance, ***a***

The value of the cylinder height *h* has been kept fixed to 110 mm respectively during the numerical analyses. Regarding the wall thickness *t* and the external diameter *de*, they will be fixed according to experimental results obtained by researchers which have studied the cactus skeleton. Figure 2.4 (left) shows the model in Ntopology of reference cylinder provided with its geometrical parameters.

For the geometry of the pore, a linear slot shape which is a good approximation of real cactus skeleton's pore shape has been selected as showed in Figure 2.4 (right). The value of the centre-to-centre distance *a* and the radius *r* will be defined in the next stage. Pore circularity was defined as:

$$Circularity = 4 \cdot \pi \cdot \frac{(pore\ area)}{(pore\ perimeter)^2} \tag{2.1}$$

In which a perfect circle has a circularity = 1. According to the research made by L. De Vivo, A.K. Matsushita, D. Kupor et al. [48] on Cholla cactus skeleton inspired cylindrical structures' mechanical performance in relation to geometrical parameters of the structure, specifically the pore circularity and the wall thickness-to-outer diameter ratio, it was observed that for thin walled tubes, a higher pore circularity improved the effective shear stiffness whereas in thicker walled tubes there were diminishing returns past circularity ~0.65. In axial compression loading, the wall thickness-to-diameter ratio had little effect on the effective compressive stiffness while a lower pore circularity improved the effective stiffness, as shown in Figure 2.6.

At approximately the average pore geometry observed in the cholla cactus, an optimal balance between axial and shear stiffness was identified. This mechanical equilibrium suggests that the cactus macrostructure is evolutionarily optimized to withstand both torsional stresses induced by wind and axial loads resulting from gravitational forces acting on its own mass. Nevertheless, as illustrated in Figure 2.5, notable variations in pore geometry are evident even along a single stalk. This spatial heterogeneity implies a potential capability of the cholla cactus to locally modulate pore roundness as a functional strategy for tuning structural stiffness in response to varying mechanical demands [48].

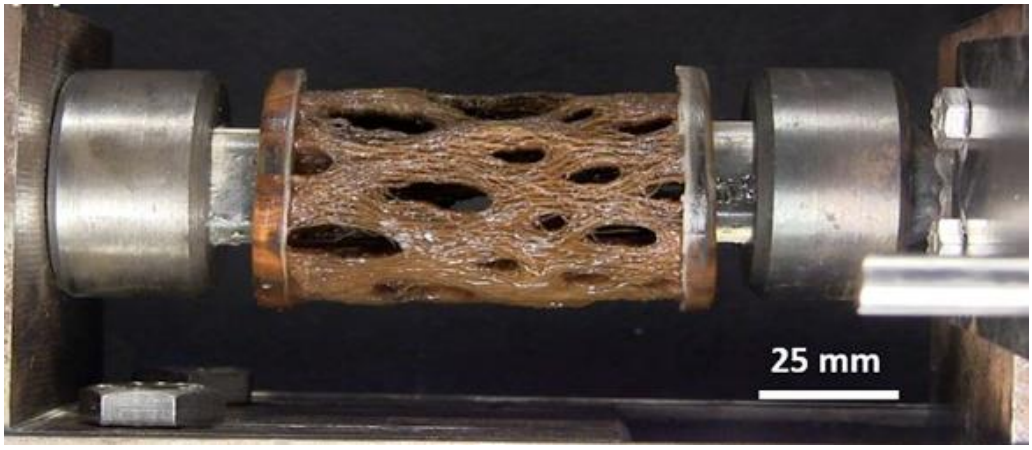

Figure 2.5 Mechanical testing on real Cholla cactus sample [48].

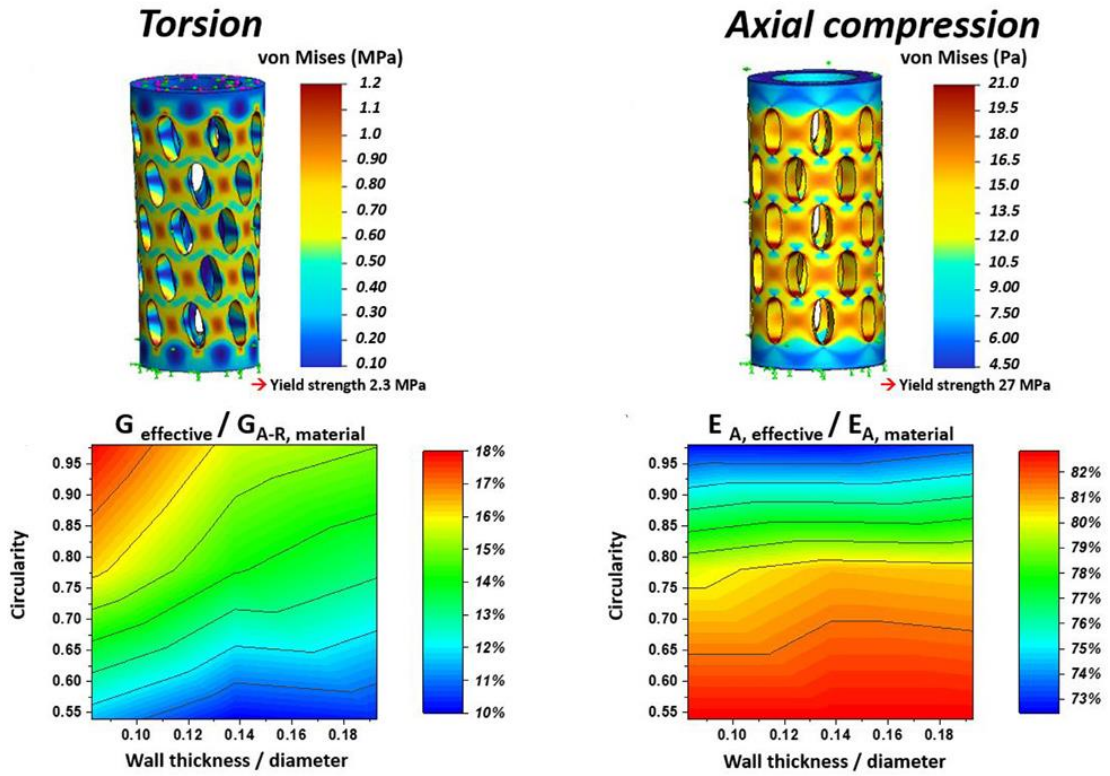

Figure 2.6 Finite element analysis of cactus skeleton inspired structures by varying pore circularity and wall thickness. On the left, results of torsion simulations with the corresponding heat map are shown (the colour intensity reflects the effective stiffness as a percentage of the prescribed material stiffness), while on the right, results of compression simulation are shown [48].

$$pore\ area\ A = r^2 \cdot \pi + a^2 = 178.5mm^2$$
$$pore\ perimeter\ P = 2 \cdot r \cdot \pi + 2 \cdot a = 51.4mm \quad (2.2)$$

The value of the centre-to-centre distance *a* and the radius *r* are respectivly 10 mm and 5 mm, so the circularity of the pore shape has been calculated according to Equation (2.1), after the values of area and perimeter were obtained with Equation (2.2), and is approximately 0.84. This value was guided by the experimental data obtained by L. De Vivo, A.K. Matsushita, D. Kupor et al. [48] presented in Figure 2.6 and the corrisponding value of wall thickness to diameter ratio is 0.08. At this geometric configuration, the cellular structure exhibits a favourable compromise between mechanical performance under compressive and torsional loading conditions. Specifically, the normalized compressive stiffness reaches approximately 78% of the base material's stiffness, indicating efficient load-bearing capacity. Simultaneously, the normalized torsional stiffness is maintained at around 17% of that of the solid material, ensuring adequate resistance to twisting, which could be present in a complex multiaxial loading system.

$$V = \left(r_e^2 - r_i^2\right) * \pi * h = 69080\ mm^3 \quad (2.3)$$

According to the wall thickness to diameter ratio previously defined, the reference geometry under consideration is a hollow cylindrical structure characterized by an external radius of 27 mm and a thickness of 4 mm. Based on the standard geometric formulation for the volume of a hollow cylinder, this configuration has a total volume of 69080 mm^3.

The objective is to design a cellular hollow cylinder which incorporates porosity on cylinder's wall through a periodic arrangement of pores with a previously defined morphology (Figure 2.4 right).

To initiate the design process, an initial target porosity of 50% is selected. This porosity is defined as the ratio between the solid (or real) material volume and the volume of the equivalent non-porous hollow cylinder.

To mimic the cactus skeleton framework, the number of pores and their spatial arrangement is fundamental. At first, the volume subtracted due to the incorporation of pores within the hollow cylinder must be one half of total volume, so as to respect the initial target porosity of 50%. The subtracted volume by a single pore can be

approximately calculated as the pore area multiplied by the cylinder wall thickness: V_{pore} = (pore area) · t = 178.5 · 4 = 714 mm³.

The total number of pores is obtained by one half of hollow cylinder's volume divided by single pore volume: N_{pore} = V / (2·V_{pore}) ≈ 48 pores, which will be arranged in different way on cylinder's wall and described in detail in the following section.

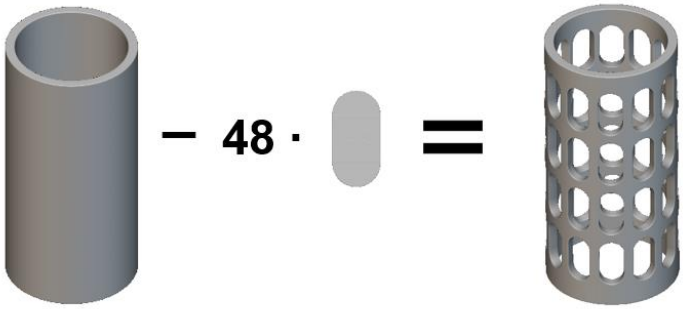

Figure 2.7 Evolution of structural design from initial reference hollow cylinder to cellular bioinspired structure.

2.3.1. Cellular structures

In this thesis work, 3 different arrangements of pores have been developed to obtain the final bioinspired cellular structures, as shown in Figure 2.13.

The primary operations performed in NTop involve the parametric design of the pore geometry and the generation of the main hollow cylindrical structure. Subsequently, a Boolean subtraction operation is applied, where a polar array of pores is systematically subtracted from the main cylinder, as shown in Figure 2.8. This results in the formation of a cellular architecture with a periodic distribution of voids, optimizing the structure for lightweight performance and mechanical efficiency.

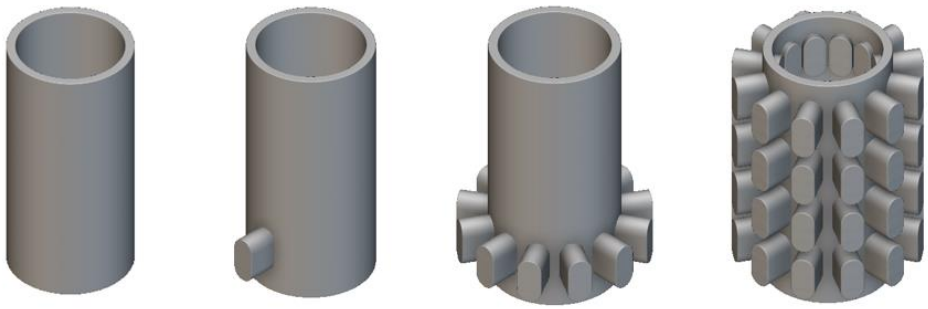

Figure 2.8 Creation of the cellular structure in Ntop using the Boolean Subtract function.

1. **Uniformly distributed pores arrangement A**: in this configuration pores are positioned on the same rows and on the same columns.

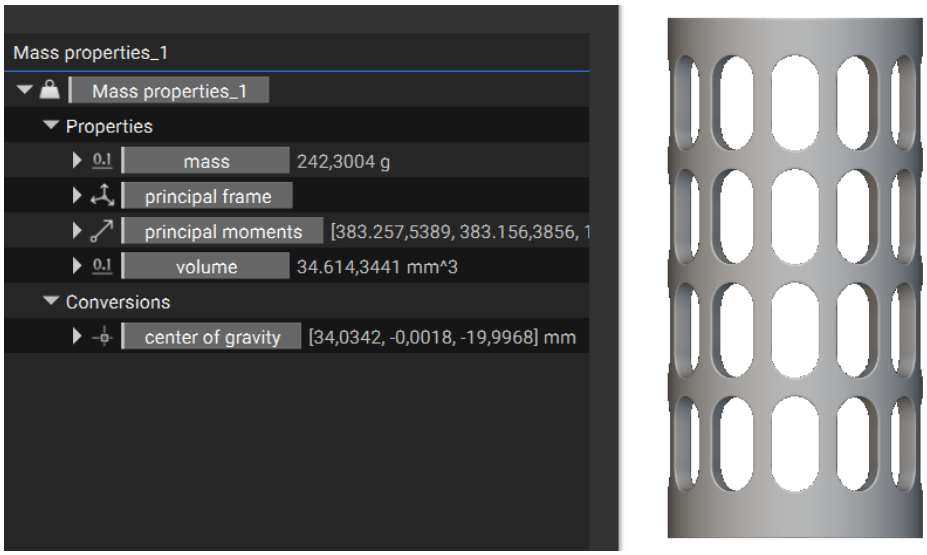

Figure 2.9 Uniformly distributed pores arrangement A and its mass properties

2. **Alternating pores arrangement B**: in this configuration pores are positioned on the same rows, and the columns are tilted.

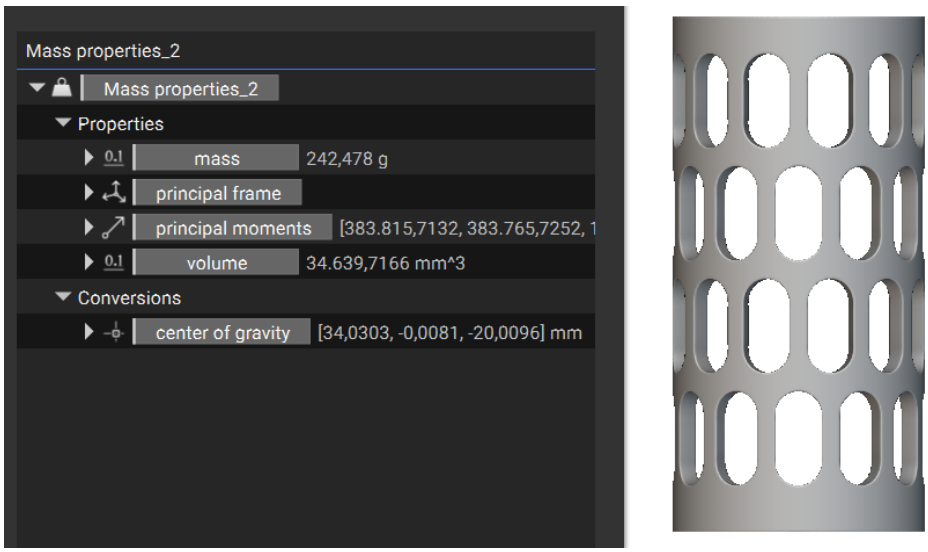

Figure 2.10 Alternating pores arrangement B and its mass properties

3. **Tilted pores arrangement C**: In this configuration, the pores are initially oriented at an angle of 30° relative to the longitudinal axis of the hollow cylinder, as illustrated in the Figure 2.11.

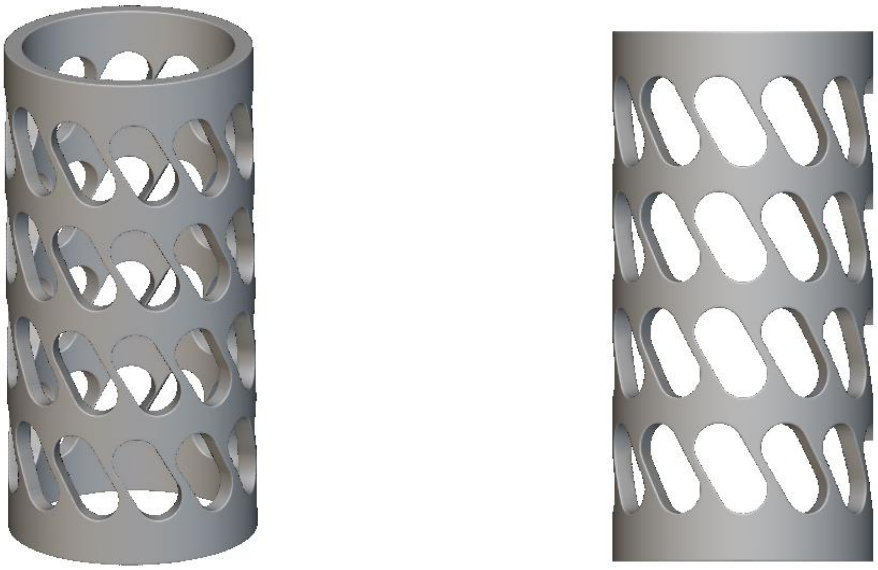

Figure 2.11 First tilted pores arrangement C, in the section image on the left, it can be observed the thin strut of the structure.

However, the initial configuration introduced a notable structural limitation: the inclination of the pores led to the formation of overly slender struts, which were prone to premature deformation under applied loads. The reduced dimension of these elements compromised the overall stiffness, making it more susceptible to localized buckling during compression. To overcome this drawback, an alternative design strategy was implemented. The pore orientation was modified to follow an alternating angular arrangement of +30° and –30° with respect to the cylinder's longitudinal axis. This configuration effectively balanced the distribution of material, resulting in a more uniform strut thickness and enhanced mechanical rigidity while preserving the desired lightweight characteristics. Moreover, the alternating pore orientation contributed to a more homogeneous stress distribution throughout the structure, thereby improving its overall stability and deformation resistance. In addition to the mechanical improvements, this revised geometry also produced a visually balanced and aesthetically refined design. The final configuration derived from this optimization is illustrated in Figure 2.12.

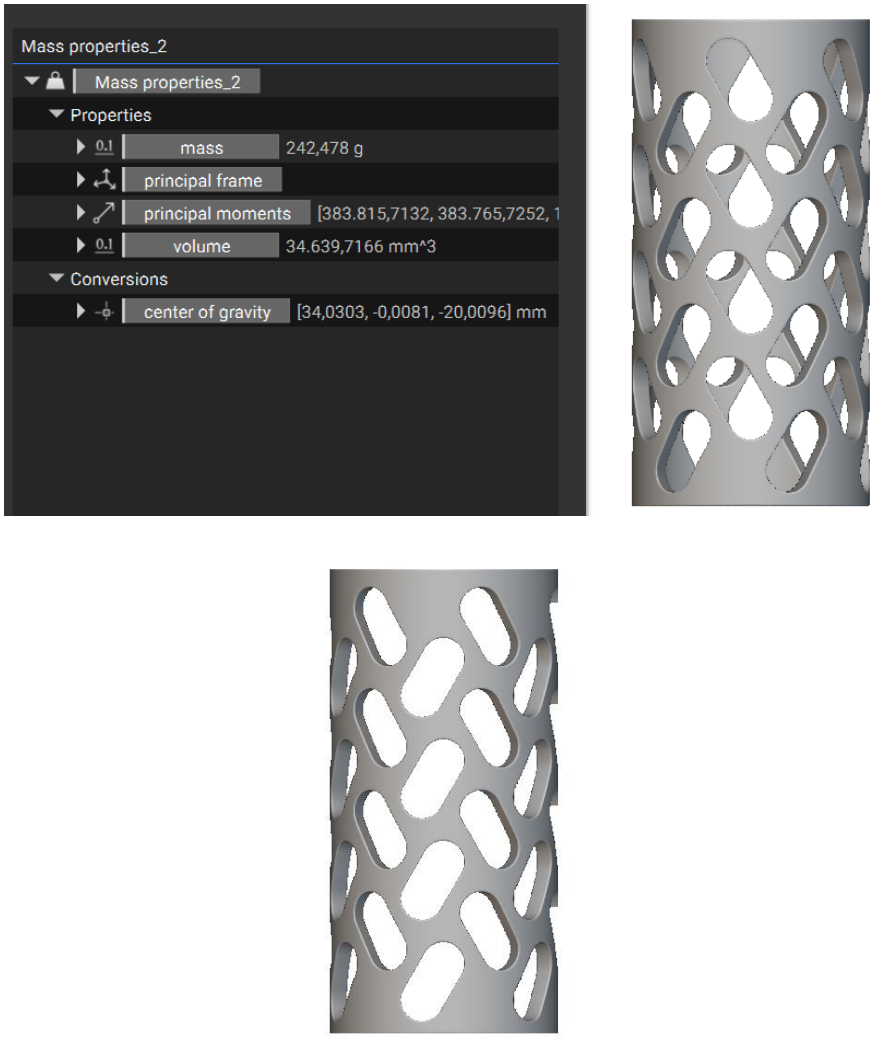

Figure 2.12 Final alternating tilted pores arrangement C and its mass properties

The design phase concludes with the selection of three distinct cellular architectures. The first configuration features a simple arrangement, with pores distributed on a rectilinear grid forming a regular rectangular cell topology. The second structure incorporates pores aligned along uniformly tilted columns, introducing directional anisotropy. The third and most advanced design employs alternatingly tilted pores (+30°/–30°), resulting in a more complex and mechanically balanced cellular lattice.

With these geometries finalized, the next phase will involve numerical simulations, including structural analysis, to evaluate and compare their mechanical performance, such as stiffness, strength, and deformation behaviour under applied loads.

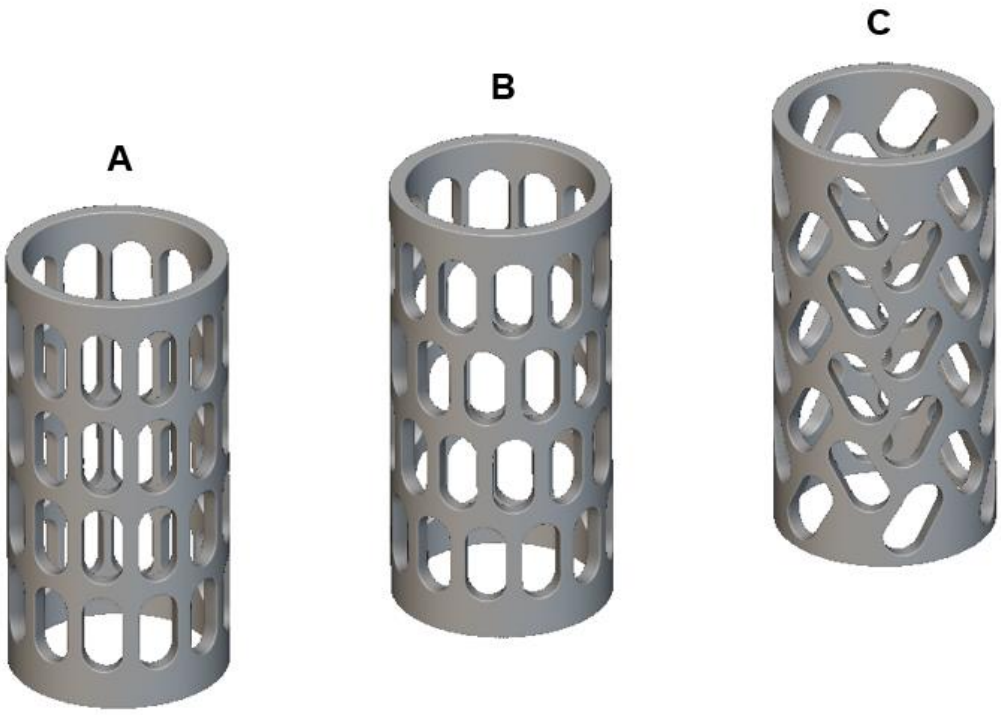

Figure 2.13 Cellular structures created with Ntopology

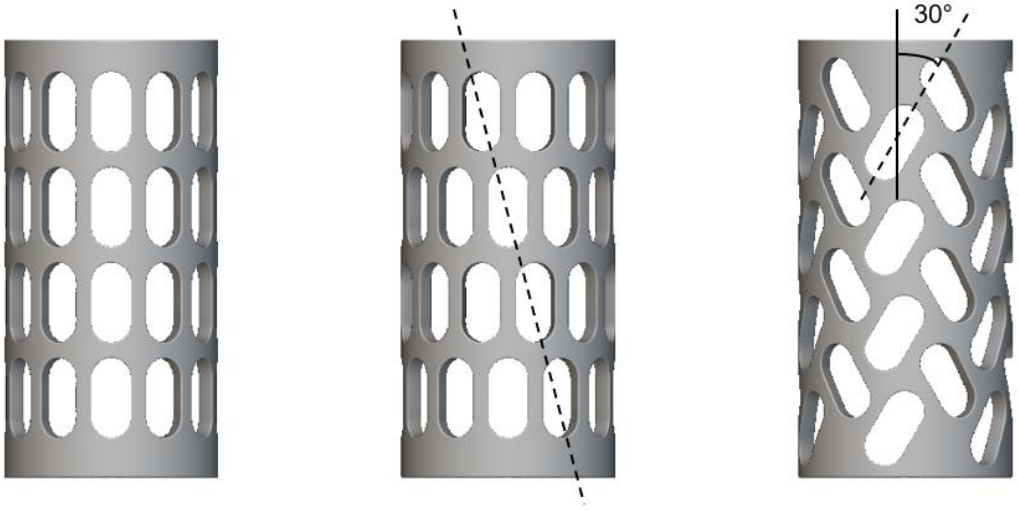

Figure 2.14 Section view: it can be observed that in the configuration B the pores are positioned on a tilted column and in the configuration C pores are inclined with respect of the cylinder axis of 30°.

2.4. Analytical methods

An analytical framework can be employed to approximate the behaviour of the reference geometry, specifically, a hollow cylindrical structure, in order to estimate the order of magnitude of the internal stresses and reaction forces involved. This preliminary assessment serves to establish a baseline for understanding the mechanical response of the structure under axial compressive loading.

The principal objective of the compressive tests, both numerical and experimental, is to investigate the deformation mechanisms and buckling behaviour of such structures when subjected to axial loads. A key aspect of this analysis is the acquisition of the reaction force as a function of displacement, which provides critical insights into the load-bearing capacity of the structure, particularly within the plastic deformation regime and the subsequent failure/instability phase.

Table 2.1 Geometrical parameter of the reference hollow cylinder

Parameter	Value
Initial length, L_0	110 mm
Final length, L_F	105 mm
External diameter, D_e	26 mm
Internal diameter, D_i	24 mm

In this context, consider a hollow cylinder whose geometric parameters are specified in Table 2.1 and depicted in Figure 2.4 (left). The analytical formulation of the compressive test begins with an initial specimen length referred to as L_0, which is subjected to a controlled axial displacement until a final length L_F, is attained. The corresponding true (logarithmic) strain, denoted as ε, is computed according to Equation (2.4).

$$\varepsilon = \ln\frac{L_F}{L_0} \tag{2.4}$$

Once the true strain is determined, two distinct methodologies can be adopted to evaluate the corresponding axial (normal) stress, referred to as σ.

The first approach involves the use of an analytical constitutive model to describe the material's plastic behaviour. For materials exhibiting strain hardening characteristics, as is the case with the one under investigation, the Hollomon equation proves suitable. This model, expressed in Equation (2.5), relates the true stress σ to the true strain ε through the material constants: the strength coefficient, denoted as *K*, and the strain hardening exponent, denoted as *n*.

$$\sigma = K \cdot \varepsilon^n \tag{2.5}$$

Alternatively, the second approach involves directly referencing the experimental true stress–strain curve of the material to extract the value of the normal stress σ corresponding to the calculated true strain ε. Given that both tensile and compressive material characterization tests were conducted within the scope of this study, the second method was adopted to ensure greater accuracy and consistency with empirical data.

$$\sigma = \frac{F}{A_F}$$
$$A_F = \frac{A_0 \cdot L_0}{L_F} \tag{2.6}$$

Once the stress σ has been established, the axial force *F* required to produce the corresponding strain level can be determined via Equation (2.6). This calculation requires knowledge of the final cross-sectional area of the deformed cylinder. Assuming volume constancy during plastic deformation, the final area is derived using Equation (2.6), which relates the initial and final cross-sectional areas, referred to respectively as A_0 and A_F.

2.5. Numerical methods

In this section, the procedure followed to simulate a compression test in Abaqus and then in COMSOL is presented in detail. The entire workflow includes mesh importation, geometry setup, boundary condition assignment, interaction definition, step configuration, and output request setup.

A. Mesh Import from nTop to Abaqus

The initial geometry and meshing of the hollow cylinder were created using nTop. The meshing strategy included the following steps:

- Generation of a mesh directly from the implicit body of structures created in nTop, ensuring geometric accuracy.
- Application of a robust tetrahedral meshing algorithm, which is well-suited for complex geometries. The global mesh length value is 3 mm with minimum feature size of 0.8 mm.
- Selection of second-order finite element mesh (quadratic elements) in FEM Volume Mesh to enhance result accuracy (Figure 2.15), especially important when capturing stress gradients and non-linear deformation behaviour.

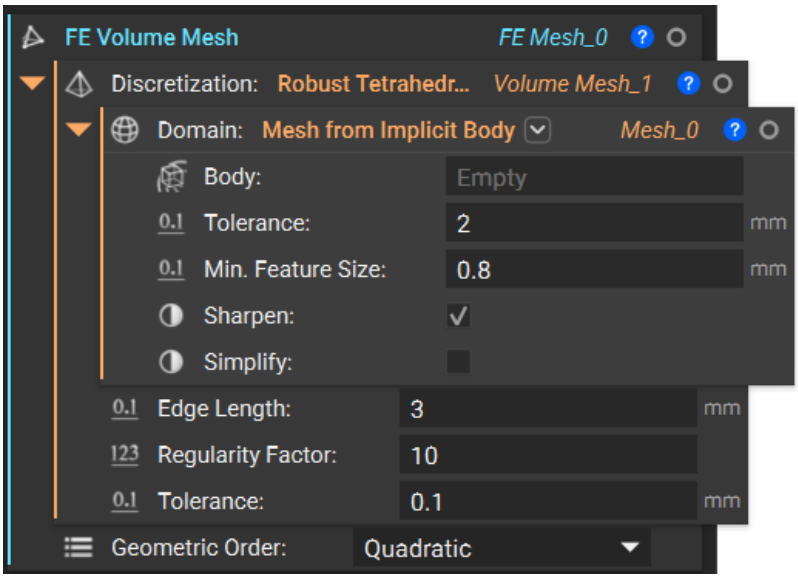

Figure 2.15 FEM Volume Mesh command panel in nTop and the parameters selected for generating the mesh for Abaqus.

Figure 2.16 Assembly of the compression test on Abaqus: Red part is the head (moving plate), white part is the base (fixed plate) and the green one is the sample to be tasted. Both plates are discrete rigid solid with reference point.

After mesh generation, the model was exported using the "Export FEM Mesh" function in nTop, resulting in an inp (Abaqus input) file format. This format is directly compatible with Abaqus and preserves the nodal and element connectivity information required for finite element analysis.

B. Importing the Mesh as Orphan Mesh in Abaqus

The exported .inp file from nTop was imported into Abaqus as an orphan mesh. An **orphan mesh** in Abaqus refers to a mesh that is not associated with any underlying CAD geometry (i.e., it lacks a parametric or sketch-based model). It is a purely mesh-based representation, typically used when models are imported from other software or generated from scan data. While orphan meshes offer limited geometry editing capabilities within Abaqus, they are fully functional for analysis, provided the mesh quality is adequate.

C. Creation of Rigid Compression Fixtures

To replicate the boundary conditions of a compression test, two rigid bodies were created:

- Base (Fixed Plate): Cylindrical shape with a radius of 30 mm and a height of 15 mm.
- Head (Moving Plate): Identical cylindrical rigid body.

For each rigid part, a Reference Point (RP) was defined. In Abaqus, rigid bodies require an associated reference point to define their kinematic behaviour. The RP serves as the control node for applying boundary conditions and loads. It is typically located at the centre of the circular face of the cylinder, coinciding with the axis of compression.

D. Assembly

The assembly stage involves positioning the three components correctly, as shown in Figure 2.16:

- The cylindrical structure is placed between the two rigid platens.
- The base is aligned at the bottom, in contact with the lower face of the cylinder.
- The head is positioned on top of the cylinder, ensuring symmetric alignment along the vertical axis.

All components are assembled using the "Independent" positioning method to allow independent meshing of each part (in this case, the mesh is already fixed, as it is an orphan mesh).

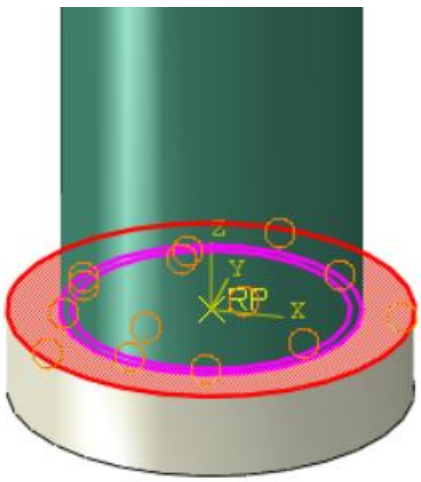

Figure 2.17 Base - Cylinder Interaction: surface-to-surface tie constraints was created

E. Interaction Definition

Two surface-to-surface tie constraints were created:

- Base - Cylinder Interaction: The lower surface of the hollow cylinder is tied to the top surface of the base platen.
- Head - Cylinder Interaction: The upper surface of the hollow cylinder is tied to the bottom surface of the head platen.

The tie constraint ensures no relative motion or separation between the surfaces during the analysis, mimicking the effect of mechanical clamps in a physical compression test setup.

F. Boundary Conditions

The boundary conditions were applied at the reference points of the rigid bodies:

- Base RP: Fully constrained using the “Encastre” condition, which fixes all six degrees of freedom (three translational and three rotational).
- Head RP: Constrained to allow only vertical displacement along the axis of the cylinder (typically the Z-axis), while all other degrees of freedom are fixed. This simulates the compressive action of a testing machine's moving crosshead.

The magnitude of the vertical displacement was varied across simulations to study the structure's response under different loading conditions.

Figure 2.18 Boundary conditions applied at the reference points of the rigid bodies.

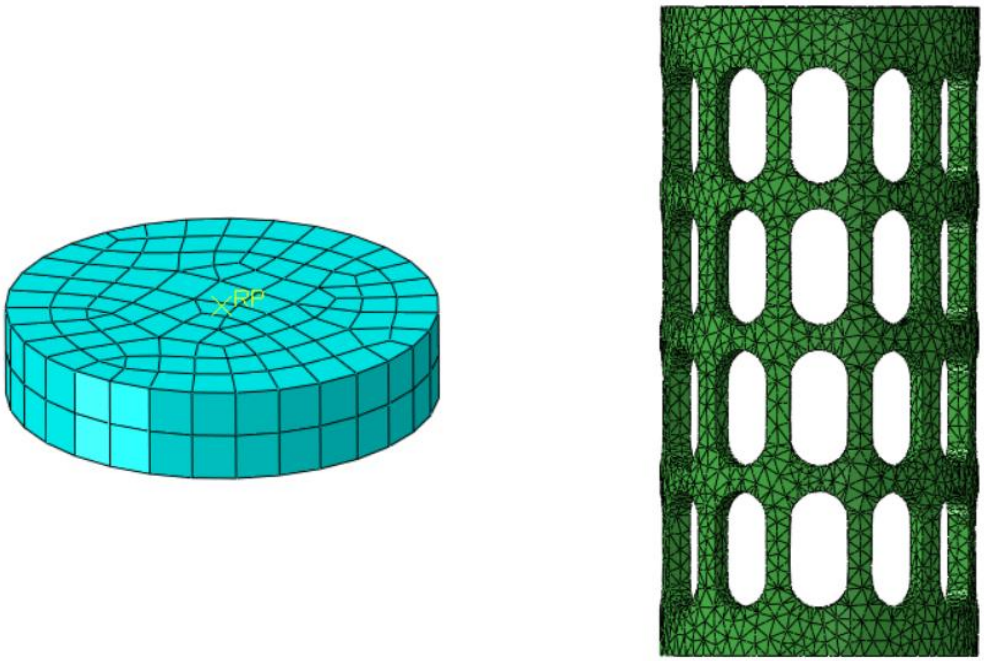

Figure 2.19 On the left: the mesh element of rigid plates is R3D4: a 4-node 3D bilinear rigid quadrilateral; on the right: the orphan mesh with secondary order tetrahedral elements imported from nTop.

G. Step Configuration

A new analysis step was created to model the loading phase. The following settings were used:

- Step Type**:** Static, General with Nonlinear Geometry (NLGEOM = on) enabled, as large deformations and potential plasticity are expected.
- Increment Control Settings:
    - Initial increment size: 0.01 – ensures gradual application of the load to help convergence.
    - Minimum increment size: 1e-5 – allows the solver to reduce step size when encountering convergence difficulties.
    - Maximum number of increments: 1.00 – ensures the analysis can proceed even under complex nonlinear responses.

These values were chosen to balance accuracy, stability, and computational efficiency, particularly important in simulations where plastic deformation or contact may lead to convergence issues.

H. Material Assignment

A material was defined and assigned to the cylinder part, with properties obtained by the material characterization which will be implemented in the chapter "Results and Discussions". At a minimum, the following properties were assigned:

- Young's modulus (E)
- Poisson's ratio (ν)
- Plasticity model

The rigid platens were assigned as analytical rigid surfaces and therefore do not require material properties.

I. History Output Request

To analyse structural performance, a history output was defined to track the displacement of the head's reference point. This data, in conjunction with stress and strain outputs from the cylinder, enables the post-processing of:

- Force Displacement curves
- Von Mises stress vs. displacement
- Equivalent plastic strain vs. displacement

These plots are essential for understanding the load-carrying capacity, stiffness, and deformation mechanisms of the structure.

J. Job Submission

After verifying the assembly, boundary conditions, material assignment, and step configuration, a job was created and submitted. The simulation results were subsequently visualized using the Visualization Module, where stress contours, deformation plots, and quantitative graphs were extracted for analysis.

2.5.1. Convergency analysis

In finite element method (FEM) simulations, convergence analysis is an essential process used to evaluate the accuracy and stability of numerical results. It involves refining the mesh and observing how key solution variables—such as displacements, stresses, or strain energy—respond to increased mesh resolution or element order. A solution is considered converged when these variables exhibit minimal change with further mesh refinement, indicating that the discretization error has been reduced to an acceptable level.

The zero-size extrapolation method with h-refinement is commonly employed as part of convergence analysis to estimate the theoretical exact solution of a numerical model. In this method, the domain is successively discretized using increasingly finer meshes, a process referred to as h-refinement, where the element size (denoted by "h") is systematically reduced. For each mesh level, a specific quantity of interest is computed. By plotting these results against the characteristic element size and extrapolating the trend toward zero element size, it is possible to estimate the solution that would be obtained with an infinitely fine mesh. This approach is particularly useful when an analytical solution is not available for comparison. It allows engineers to assess the accuracy of the FEM solution and to quantify discretization error.

Table 2.2 Convergence analysis table

Mesh Size h (mm)	Stress (MPa)	h^2	Relative Error %
3,6	485	12,96	3,61
3	496	9	1,43
2,4	501	5,76	0,43
2	503	4	0,04

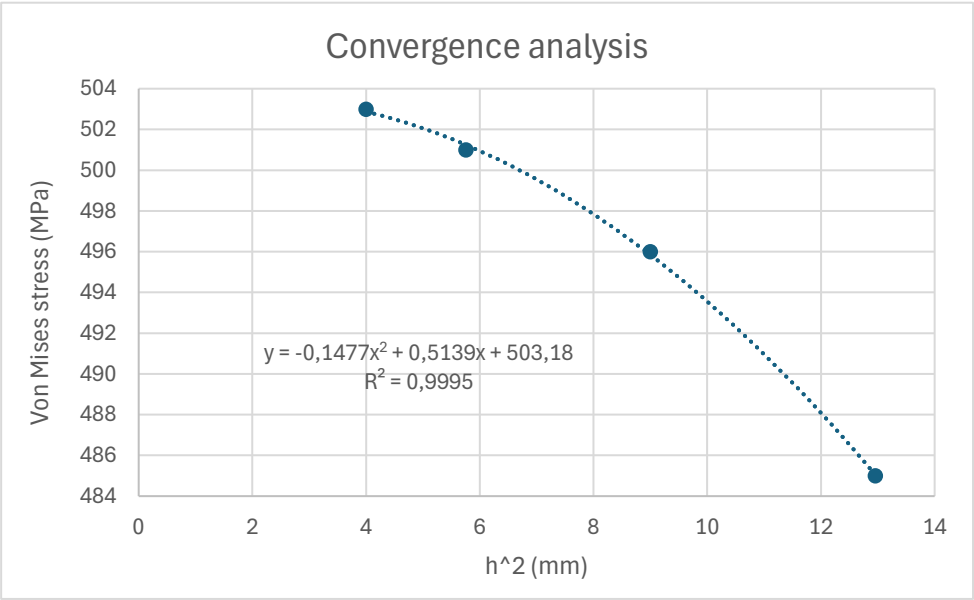

Figure 2.20 Convergence analysis table

$$\sigma(h^2) = -0.1477(h^2)^2 + 0.5139(h^2) + 503.18 \quad (2.7)$$

In this thesis work, convergence analysis was conducted on the structure featuring the first pore arrangement. The analysis involved varying the global mesh size h, with values selected as 3.6 mm, 3.0 mm, 2.4 mm, and 2.0 mm. For each mesh, the von Mises stress was evaluated at the most highly stressed element located adjacent to a pore, where stress concentration is most critical. The corresponding stress values obtained were 485 Mpa, 496 Mpa, 501 Mpa, and 503 Mpa, respectively. Using the zero-size extrapolation method, where a second-order polynomial fit is applied with respect to h^2, the estimated stress value at h=0 was determined to be 503.18 Mpa, as shown in Equation (2.7). The relative errors associated with each mesh size, when compared to the extrapolated value, were calculated to be approximately 3.6%, 1.4%, 0.4%, and 0.04%, respectively. Based on this analysis, a global mesh size of 3.0 mm was selected for the final simulations, as it provides a sufficiently accurate result with a relative error close to 1%, while also significantly reducing computational cost compared to finer meshes.

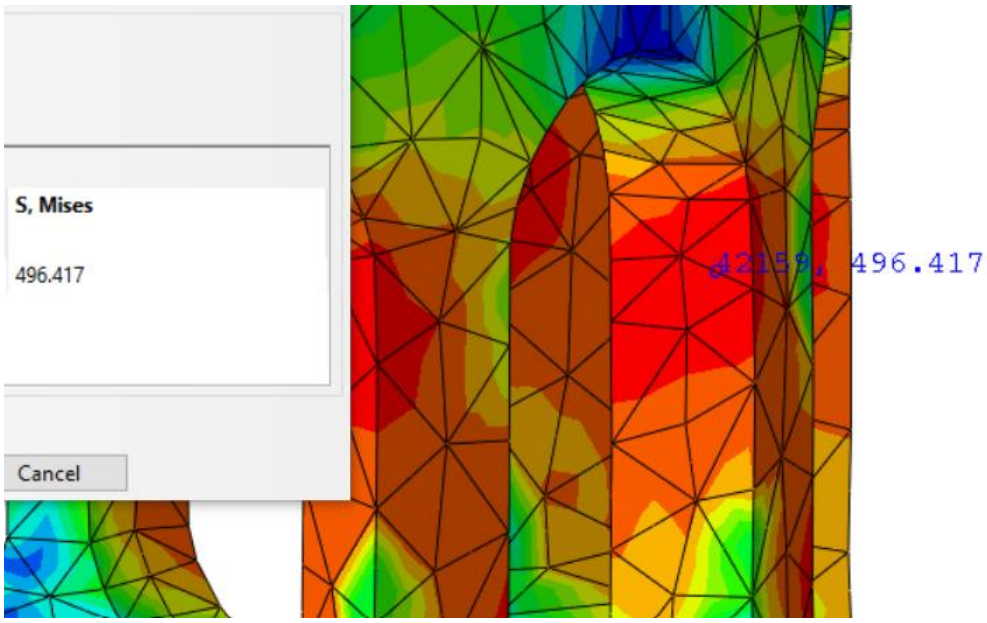

Figure 2.21 Most highly stressed element located adjacent to a pore.

2.5.2. COMSOL

In this section, the complete procedure followed to simulate the compression test using *COMSOL Multiphysics* is described in detail. The workflow was carefully structured to ensure that the numerical model accurately represented the physical behaviour of the tested material under compressive loading. The main steps of the procedure are summarized below.

The simulation begins with the importation of the geometry in STL format. After importing, the geometry is checked for integrity to confirm that no defects or inconsistencies are present that could affect meshing or computation. To improve mesh quality and ensure smooth transitions between elements, the imported geometry undergoes a remeshing process, specifically at edges and faces. Edge remeshing refines the discretization along the specimen boundaries where stress concentrations are expected, while face remeshing provides a more uniform surface mesh and minimizes element distortion in subsequent meshing steps.

Following this preparation, the solid mesh is generated using the Free Tetrahedral meshing option, which is suitable for complex three-dimensional geometries. Mesh parameters such as element size, curvature refinement, and minimum element quality are adjusted to obtain an optimal balance between computational efficiency and result accuracy.

After the mesh is finalized, the Solid Mechanics physics interface is introduced to define the mechanical behaviour of the model. The material properties are specified by assigning the density, Young's modulus, and Poisson's ratio, which collectively describe the elastic characteristics of the material. To capture the nonlinear behaviour observed during the compression test, plasticity is incorporated within the solid mechanics' interface. The initial yield stress is defined to represent the onset of plastic deformation, and an isotropic hardening model is employed to describe the uniform expansion of the yield surface as the plastic strain increases.

The boundary conditions and loading configuration are then defined. One surface of the specimen is fully constrained to prevent rigid body motion, while the opposite surface is subjected to a prescribed displacement to simulate the experimental loading conditions.

To conduct the numerical analysis, a time-dependent study is created. The geometric nonlinearity option is activated to account for large deformations that may occur during compression. A ramp time function varying linearly from 0 to 1 is defined to gradually apply the load throughout the simulation, ensuring smooth convergence and numerical stability of the solver. Once all settings are defined, the simulation is launched, and COMSOL automatically performs the iterative solution process.

2.6. Experimental methods

In this section, the experimental procedures for testing the bio-inspired structures and fabricating these structures using the novel alloy are presented. The discussion begins with an overview of the 3D printing technology highlighting the one employed to create the initial polymeric prototypes, Fused Deposition Modelling (FDM). Details regarding the specific 3D printer, filament composition, printing parameters are provided. This is followed by a comprehensive description of the casting process, which was used to translate the 3D-printed models into metal components. Finally, the design of experiments (DOE) is presented, outlining the methodologies adopted for metallographic characterization of the bio-inspired metallic structures involving standard sample preparation steps, the compression testing, and the subsequent analysis of crystal structure. Microstructural evaluation was performed using Light Optical Microscopy (LOM) for initial phase assessment and Scanning Electron Microscopy (SEM) for high-resolution analysis of the microstructure

2.6.1. Additive manufacturing

3D printing is an innovative fabrication process that builds components by successively adding material layer by layer—contrary to traditional subtractive methods that involve removing material from a solid block. This layer-wise manufacturing approach enables the creation of highly complex geometries that would be difficult or impossible to achieve using conventional techniques.

Over the past few decades, AM has seen rapid growth and adoption across a wide range of sectors including biomedical engineering, aerospace, automotive industries, as well as art, design, and architecture. Its increasing popularity is largely due to its intrinsic advantages: reduced material waste, cost-effectiveness in prototyping, design flexibility, and the ability to fabricate intricate structures with relative ease

According to the ISO/ASTM 52900:2015 standard, AM technologies are classified into seven primary categories based on the method of material deposition, each of these methods offers unique capabilities suited to different materials and applications:

- Material Extrusion (ME)
- Material Jetting (MJ)
- Binder Jetting (BJ)
- Sheet Lamination (SL)
- Vat Photopolymerization (VP)
- Powder Bed Fusion (PBF)
- Directed Energy Deposition (DED)

Despite the diversity of AM techniques, the core process generally follows a standardized workflow:

1. **Digital Model Creation**

   A 3D digital model of the desired component is generated using CAD (Computer-Aided Design) software. Alternatively, Reverse Engineering or 3D scanning can be employed.

2. **File Conversion to STL Format**

   The CAD model is converted to an STL (Standard Tessellation Language) file, which encodes the surface geometry of the object using triangular facets.

3. **Slicing**

   The STL file is processed by slicing software, which divides the model into thin horizontal layers and generates a G-code. This code includes detailed instructions for the printer, such as the path of the print head, material flow, and speed.

4. **Printing**

   The printer interprets the G-code and begins material deposition according to the specified parameters. Depending on the technology, post-processing may be required to achieve the final desired properties or surface finish.

For the fabrication of test specimens in this study Fused Deposition Modelling (FDM) was selected. FDM falls under the Material Extrusion category and was chosen due to its [50]:

- High resolution (up to 20 microns)
- Capability to print multiple materials simultaneously
- Competency in producing complex geometries
- Cost-effectiveness of both equipment and feedstock

The production chain begins with the design of the component using nTop. Once the model is finalized, it is exported in STL format and imported into *Ultimaker Cura*, a slicing software compatible with the printer used. This software allows users to slice the model into horizontal layers, visible in the final product, generate and customize the extruder's tool path for each layer, adjust key printing parameters (e.g., speed, temperature, infill), which influence the surface finish, dimensional accuracy, and mechanical integrity of the final printed prototype. The software additionally provides a visual preview of the build sequence, facilitating the detection of potential printing anomalies prior to fabrication. All this information is compiled into a G-code file and sent to the printer to begin fabrication.

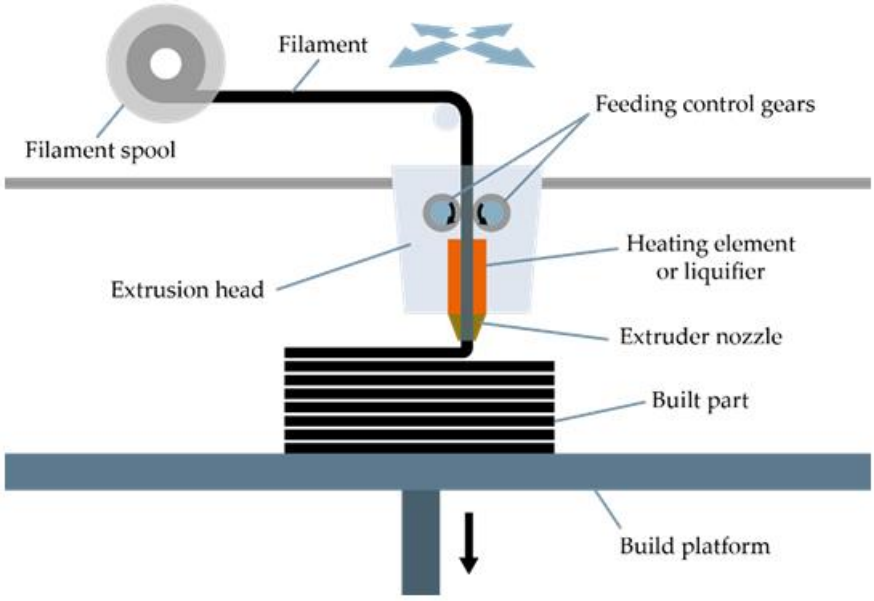

Figure 2.22 A simplified diagram of a Fused Deposition Modelling 3D-printer.

The printer employed for specimen fabrication is the Ultimaker S3™, selected for its versatility and compatibility with a wide range of filament materials. A diagram of the FDM setup is provided in.

The Ultimaker S3™ operates using thermoplastic filament feedstock, typically in diameters ranging from 1.75 mm to 2.85 mm, depending on the nozzle size. The filament is fed into the extruder by a system of drive gears controlled by stepper motors. Once inside the extrusion head, the filament is heated above its glass transition temperature in a liquefier and then extruded through a fine nozzle [51].

The molten polymer is deposited layer by layer onto a heated build platform, where it solidifies. After each layer is completed, the build plate lowers incrementally to accommodate the next layer, repeating the process until the full part is completed.

FDM offers several advantages, making it an accessible and cost-effective additive manufacturing method. The process is characterized by its simplicity of operation, requiring relatively low technical expertise and minimal setup time, while still enabling the fabrication of geometrically complex and topologically optimized structures that would be difficult or impossible to achieve using conventional subtractive or formative methods. A wide range of thermoplastic materials can be used, and the process is clean and environmentally friendly, as it involves no harsh chemicals or hazardous waste. In this study, FDM was preferred over traditional manufacturing methods due to its efficiency and reduced cost, particularly for prototyping.

Figure 2.23 Ultimaker S3™

However, FDM also presents notable limitations. The mechanical properties of printed parts are highly anisotropic due to weak interlayer bonding, especially when loaded perpendicular to the filament orientation. Surface quality is often poor, with visible layer lines and roughness, making it unsuitable for applications requiring high fatigue resistance or aesthetic finishes. Dimensional accuracy can be limited, and complex or fine features may not be precisely reproduced, even at 100% infill. Warping can occur if the length-to-thickness ratio is too high, and support structures are often necessary for overhangs exceeding 45°, which can further degrade surface quality and increase print time.

2.6.2. Casting

Casting is a primary manufacturing route in which a molten material (typically a metal or alloy) is introduced into a mould cavity and allowed to solidify, producing parts that range from simple forms to highly complex, near-net-shape components. Casting is valued for its geometric freedom, ability to incorporate internal features, and suitability for both low- and high-volume production; it also often reduces the need for extensive machining or joining operations [52].

Major categories of casting processes include:

- Sand casting.
- Shell moulding.
- Investment (lost wax) casting.
- Die casting (gravity, hot-chamber and cold-chamber).
- Permanent mould casting.
- Centrifugal casting.
- Continuous casting.
- Vacuum, squeeze casting and other advanced techniques (e.g., ablation casting, tilt casting).

Each method differs in tooling cost, surface finish, achievable tolerance, part size range, cycle time, and suitability for particular alloys or production volumes; for example, sand casting is inexpensive for large parts and short runs, while investment casting provides superior surface finish and fine feature reproduction for medium to high precision applications.

Investment casting (commonly called lost-wax casting) is especially appropriate for manufacturing bio-inspired structures that require highly intricate geometries and good surface finish. The method allows the direct translation of a detailed pattern, traditionally sculpted in wax or, increasingly, produced by additive manufacturing (3D printing of castable resins), into a refractory ceramic mold. Investment casting therefore supports the fabrication of biomimetic components where morphological accuracy and surface detail are important to structural performance or aesthetic function [53]. An investment casting workflow comprises the following stages:

1. **Design and Pattern generation** — produce the master geometry as a wax or castable resin pattern; when using additive manufacturing (rapid investment casting), the pattern can be 3D-printed to eliminate tooling and accelerate iteration.
2. **Assembly (treeing)** — multiple patterns are attached to a central sprue (a "tree") for batch casting when appropriate, and additional gating is designed to control metal flow and feeding.
3. **Investment (ceramic coating)** — the assembly is dipped repeatedly into a refractory slurry and coated with stucco (fine particulate refractory) to build a robust ceramic shell; layer thickness and slurry composition are selected to match alloy, casting size and thermal requirements.
4. **Drying** — the ceramic shell is dried and cured to develop sufficient strength for dewaxing and pouring.

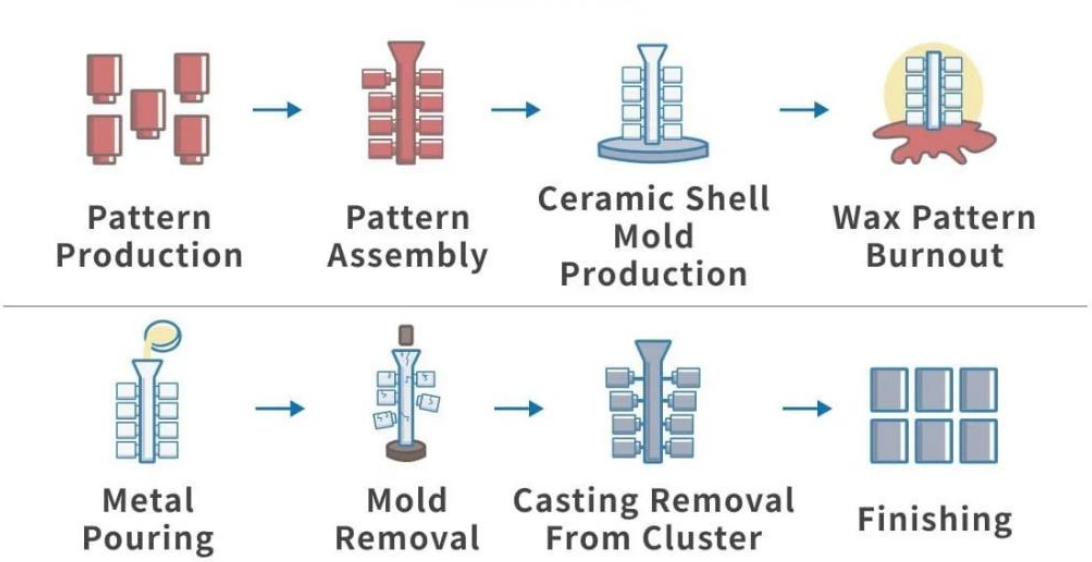

Figure 2.24 Investment casting process flow diagram

5. **Dewaxing/ Burnout** — the wax or sacrificial resin is removed thermally (autoclave or kiln) leaving a clean cavity; burnout schedules are controlled to avoid shell cracking and to remove organic residues that could cause defects.
6. **Preheat / Shell conditioning** — the empty shell is heated (sintered) to the appropriate temperature to reduce thermal gradients and to prevent thermal shock when the molten metal is introduced.
7. **Pouring / Casting** — molten metal is introduced into the hot shell by gravity, vacuum, pressure or centrifugal methods depending on alloy and design constraints; the controlled fill and solidification strategy reduces porosity and shrinkage defects.
8. **Cooling** — after the alloy has sufficiently solidified, the assembly is allowed to cool under controlled conditions to minimize residual stresses and ensure metallurgical quality.
9. **Shell removal (divestment)** — the ceramic shell is mechanically broken away (vibratory, water blasting or chemical dissolution depending on shell system) to expose the cast parts.
10. **Inspection and post-processing** — non-destructive testing (NDT), dimensional inspection and any surface treatments (coating, polishing, machining) complete the production cycle.

2.6.3. Design of experiments

The experimental design was structured around two distinct batches of cast specimens, each serving a specific purpose in the material characterization process. The first batch was dedicated to preliminary microstructural evaluation of the alloy in its as-cast condition. Samples were extracted from various regions of the casting to account for potential heterogeneity arising from solidification gradients. These specimens underwent standard metallographic preparation, including sectioning, mounting, grinding, polishing, and etching, followed by examination under Light Optical Microscopy (LOM) to assess the phase distribution, grain morphology, and potential casting defects and Scanning Electron Microscopy (SEM) to identify the composition of each phase. The second batch was reserved for mechanical testing to evaluate the alloy's response under compressive loading. The bio-inspired structures were subjected to uniaxial compression tests, after which the most deformed regions were sectioned for detailed post-deformation analysis. These deformed samples were then subjected to identical sample preparation procedures and subsequently analysed using Electron Backscatter Diffraction (EBSD). This technique enabled a more comprehensive assessment of microstructural evolution, with particular attention to the potential formation of ε-martensite or other deformation-induced phases.

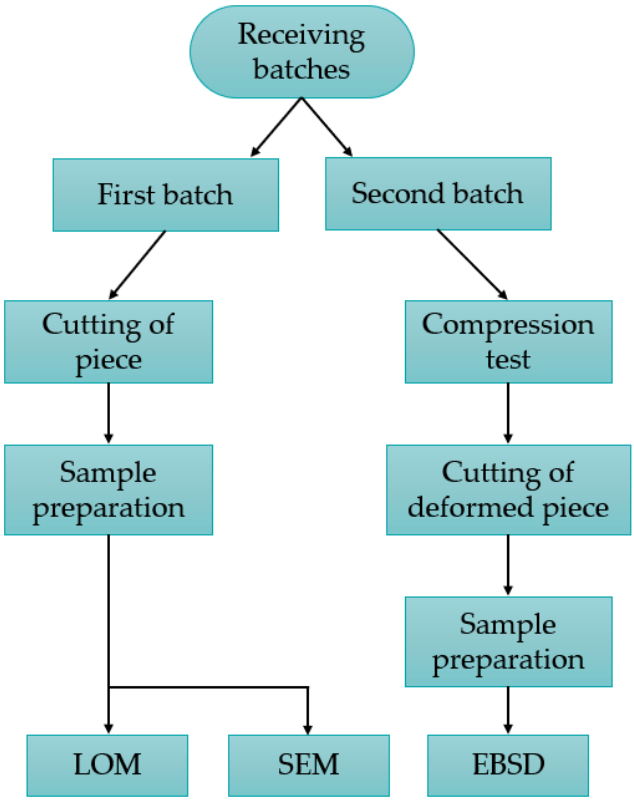

Figure 2.25 Design of experiment diagram

2.6.4. Compression test

To evaluate the real behaviour of the cast samples, a compression test was performed using a servo-hydraulic testing machine. The equipment used was an MTS model equipped with a 150 kN load cell. Prior to testing, two steel plates larger than the base area of the specimens were positioned and securely fixed at the upper and lower ends of the compression machine to ensure uniform load distribution during testing.

Figure 2.26 MTS servo-hydraulic testing machine

2.6.5. Metallographic analysis

Surface preparation began with grinding, starting with P60 grit sandpaper to create a rough surface, followed by sequential refinement up to P2500 grit. Polishing was then carried out using a rotating cloth plate. The initial polishing stage employed a 6-micrometer cloth, while the final step used a 1-micrometer cloth to achieve a mirror-like finish. All procedures were performed in accordance with *ASTM E3* standards. Samples were subsequently treated with a specific etchant selected based on the microstructural features to be revealed. For the analysed alloy, a 1:1:1 mixture of nitric acid, hydrochloric acid, and distilled water was used on the surface for approximately 10-15 seconds. Immediately after surface preparation, the samples were examined using a *Nikon ECLIPSE LV150NL* Light Optical Microscope to analyse their microstructures. Images were captured at 50× magnification to provide an overall view of each sample's microstructure and at 200× magnification for a more detailed observation of the material's features. The Scanning Electron Microscope (SEM) was utilized to perform a detailed analysis of the material's phases, including the identification and characterization of precipitates. This analysis provided valuable insights into their morphology, distribution, and interaction with the matrix.

3 Material characterization

Material characterization is the process of systematically analysing the structure, composition, and properties of materials to understand their behaviour and performance under various conditions. This involves a combination of microstructural and mechanical evaluations. Metallographic analysis, using techniques such as Light Optical Microscopy (LOM), allows for the examination of the grain structure and phase distribution within the material. Scanning Electron Microscopy (SEM) provides high-resolution images of the material's surface and microstructural features, while Electron Backscatter Diffraction (EBSD), often used in conjunction with SEM, allows users to correlate local crystal orientation with a sample's microstructure. Mechanical tests, including hardness and tensile testing, are performed to assess the material's strength, ductility, and toughness.

In this thesis, an alloy previously studied by other students in their thesis work [54] has been cited, because that alloy is similar to the new one studied in this thesis and its material property will be used for the preliminary numerical simulation on Abaqus and COMSOL.

3.1. High-Mn stainless steel

In the thesis work of Alessandro Capitanio and Giorgio Carlesso [54], two distinct high manganese alloys for structural components in Lead-cooled Fast Reactors were investigated (Table 3.1). Mn is particularly valuable as a partial substitute for nickel in austenitic stainless steels, reducing costs while maintaining phase stability. In high concentrations, it fosters a fully austenitic microstructure at room temperature. Furthermore, manganese improves hot ductility and contributes to solid solution strengthening. Mn enhances work hardening behavior and mechanical strength, which are crucial for maintaining structural integrity under the extreme conditions of nuclear reactors. Cr content in these alloys promotes the formation of a stable and protective oxide layer, thereby mitigating the effects of lead-induced corrosion.

Considering the actual chemical composition of Alloy 1, the Schaeffler diagram was utilized to estimate the expected microstructure and the calculations yielded Cr_{eq} = 20.3% and Ni_{eq} = 6.75%. For Alloy 2, the results were Cr_{eq} = 17.86% and Ni_{eq} = 9.53%.

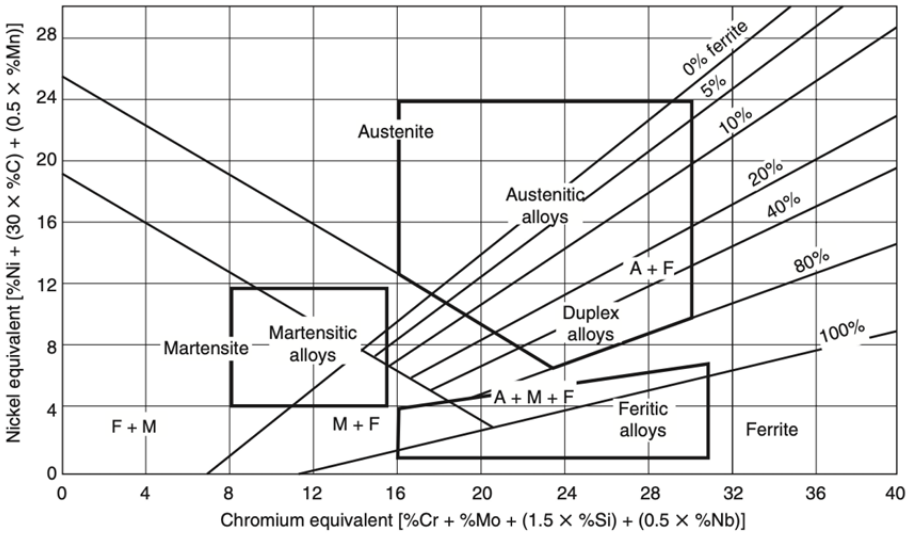

Figure 3.1 The Schaeffler–Delong diagram

Alloy 1 was designed as a ferritic alternative to traditional materials, replacing nickel with manganese. Alloy 2 was developed as a counterpart to conventional austenitic stainless steels. It maintains an austenitic microstructure but substitutes nickel with manganese, aiming to achieve comparable properties through a different elemental approach.

Alloy 2 is similar to the newly developed alloy, in the following paragraph its characterization will be presented, and its tensile test curve will be used in next chapter to simulate the material property of numerical analysis made on Abaqus.

Table 3.1 Chemical compositions of alloy 1 and alloy 2

%wt.	Cr	Mn	Ni	Si	C	N	Nb	P	S	B
Alloy1	19.31	11.09	0.155	0.648	0.035	0.070	0.021	0.027	0.0052	<0.002
Alloy2	14.72	12.22	0.385	1.961	0.101	0.088	0.349	0.034	0.0040	0.029

Thermo-Calc simulations predicted a predominantly austenitic microstructure for Alloy 2 at room temperature, with minor ferrite and possible sigma phase formation depending on the thermal history. At solubilization temperatures (950°C–1050°C), austenite remains the main phase, with increasing ferrite content at higher temperatures.

Experimental results confirmed these predictions. Samples solubilized for 30, 60, and 120 minutes exhibited an austenitic matrix with varying ferrite content, lowest at 950°C and increasing with temperature. Precipitates, initially distributed along grain boundaries, became more localized and less abundant at higher temperatures, with near-complete dissolution at 1050°C. Longer holding times promoted grain growth and further precipitate dissolution, while increasing ferrite slightly, particularly at prolonged durations like 240 to 2880 minutes, an effect attributed to the slow diffusion of ferrite-stabilizing elements such as chromium, silicon, and niobium.

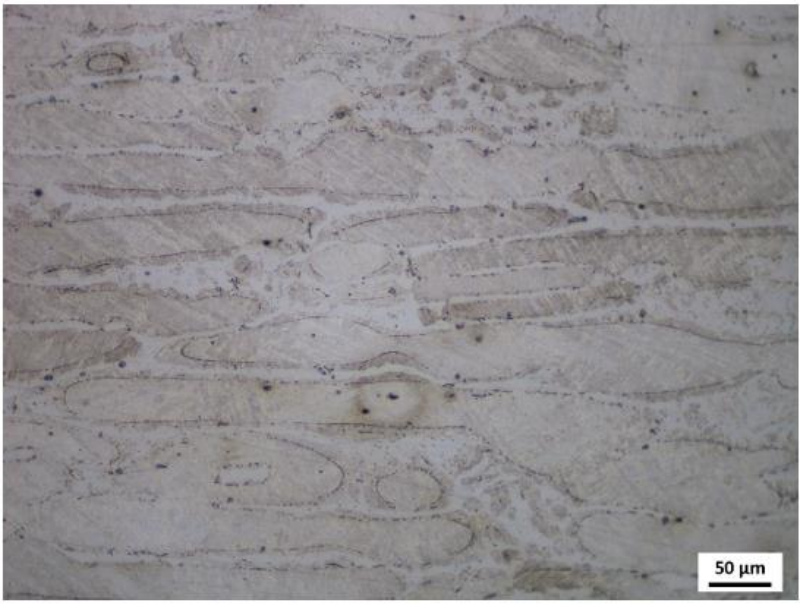

Figure 3.2 Hot rolled and solubilized Alloy 2 microstructure image taken with optical microscope.

In the as-cast condition, precipitates are abundant along grain boundaries, but after solubilization, their quantity decreases and they form localized clusters. In the hot-rolled solubilized condition (Figure 3.2), these precipitates are found within austenite grains, likely due to prolonged high-temperature exposure, which promotes both grain growth and the incorporation of boundary-associated precipitates into the matrix. The observed microstructure was consistent with LOM findings, confirming the coexistence of two phases (ferritic and austenitic) and the variations in grain size, shape, and precipitate distribution as a function of the material's processing conditions. A slight difference was observed between the as-cast condition and the solubilized and hot-rolled solubilized states. In particular, in the ferrite phase, chromium and manganese concentrations were lower in the as-cast condition compared to the solubilized and hot-rolled solubilized samples.

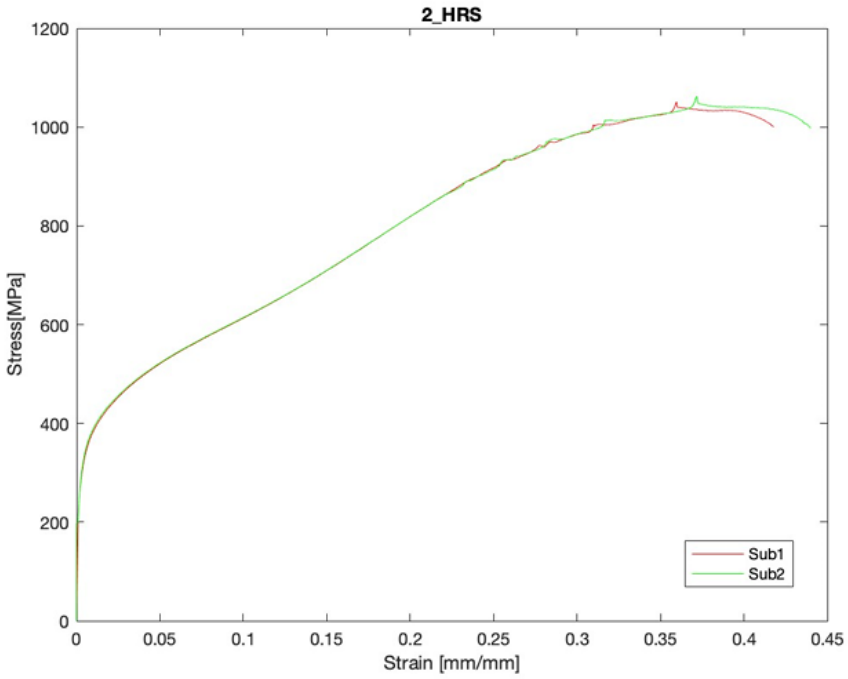

Figure 3.3 Stress vs strain curves obtained from tensile tests on hot-rolled and solubilized Alloy 2

The mechanical characterization of the material began with hardness analysis, with a primary focus on assessing the influence of holding time and temperature during solu tion heat treatment. Vickers hardness tests showed that higher temperatures reduced hardness due to precipitate dissolution, despite increased ferrite. Holding time had minimal impact, as grain growth and precipitate evolution appeared to offset each other. Solubilized and hot-rolled solubilized samples showed similar hardness, both higher than the as-cast condition due to the elimination of residual stresses and solid solution strengthening.

Tensile testing was conducted on specimens that underwent hot rolling and subsequent solubilization. The results demonstrated high elongation percentages alongside elevated UTS. Additionally, the material exhibited a significant difference between Rp02 and UTS, highlighting its strong strain-hardening capability. Tensile tests on hot-rolled solubilized samples revealed excellent ductility (43.4% elongation) and high strength (UTS = 1056.5 MPa), with significant strain-hardening (Figure 3.3). Fractographic analysis showed predominantly ductile fracture with dimple formation from void nucleation. However, the presence of microcracks in localized regions pointed to increased brittleness due to secondary phases or defects, which may contribute to crack initiation after necking.

3.2. The new High Mn alloy

Table 3.2 Chemical composition of the new High manganese alloy

%wt	Fe	C	Mn	Cr	Si	Ni	V	Nb	Mo
Alloy	60.19	0.22	21.47	17.57	0.47	0.23	0.084	0.104	0.046

In this section, the newly developed high-manganese, high-chromium alloy employed for the casting of the bio-inspired structures is presented. The components were received in the as-cast condition and subsequently subjected to a solution heat treatment at 1050 °C for 30 min in an electrical resistance furnace, followed by water quenching. The nominal chemical composition of the alloy is reported in Table 3.2. Compared with Alloy 2 investigated by Alessandro Capitanio and Giorgio Carlesso, the present composition is characterized by an increased manganese and chromium content, with the aim of enhancing austenite stability, corrosion resistance, and solid-solution strengthening.

Thermodynamic calculations performed using Thermo-Calc under equilibrium conditions (Figure 3.4) indicate that the alloy behaves as a highly alloyed austenitic system with a marked tendency for ferrite and intermetallic phase formation. At low temperatures, the predicted microstructure is dominated by a mixture of ferrite (BCC_A2) and σ (SIGMA_D8B) phases, together with a minor fraction of $M_{23}C_6$ carbides. This phase assemblage reflects the strong partitioning of chromium into the σ phase and carbides and highlights the high thermodynamic stability of Cr-rich intermetallic compounds in this compositional range. As the temperature increases from room temperature up to approximately 400–450 °C, ferrite remains the prevalent phase while the σ phase is still present in significant amounts. A rapid phase transition occurs in the temperature interval between about 450 °C and 500 °C, where austenite becomes thermodynamically stable and progressively replaces the ferritic matrix. Above this temperature, austenite represents the dominant phase over a wide temperature range, whereas the σ phase gradually dissolves and the carbide fraction becomes negligible. This behavior is particularly relevant from a processing standpoint, as it defines the temperature window in which detrimental intermetallic phases can be effectively dissolved. At higher temperatures (approximately 850–900 °C), the BCC_A2 phase reappears due to the expansion of the ferrite phase field, leading to an austenite–ferrite two phase region. With further temperature increase, the ferrite fraction progressively grows at the expense of austenite, while secondary phases such as σ and $M_{23}C_6$ are almost completely dissolved.

At the selected solution treatment temperature of 1050 °C, the alloy is therefore located in the austenite–ferrite two phase field, consisting of austenite as the major phase and a significant fraction of ferrite, with a minimal portion of carbides (2-3%). The choice of this temperature ensures the dissolution of brittle intermetallic compounds and promotes chemical homogenization of the as-cast microstructure.

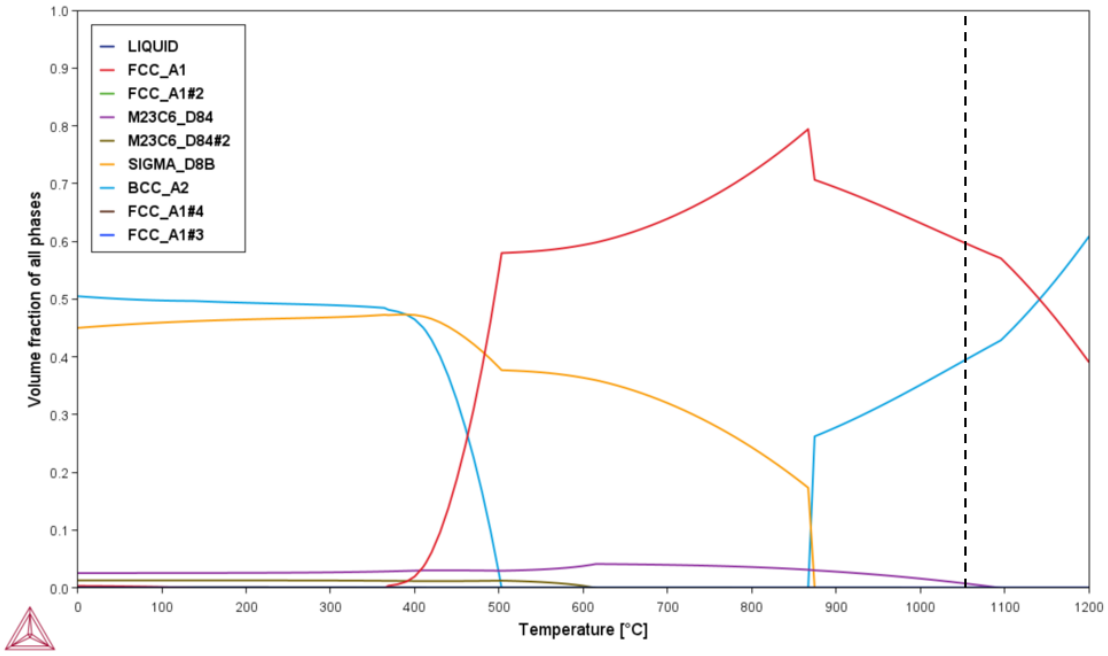

Figure 3.4 Novel alloy phase volume ratio with ThermoCalc software.

3.2.1. LOM

This section presents the results of the microstructural analysis of the new High Mn steel conducted using an optical microscope. The samples are cutted from the first batch, in as-cast solubilized condition.

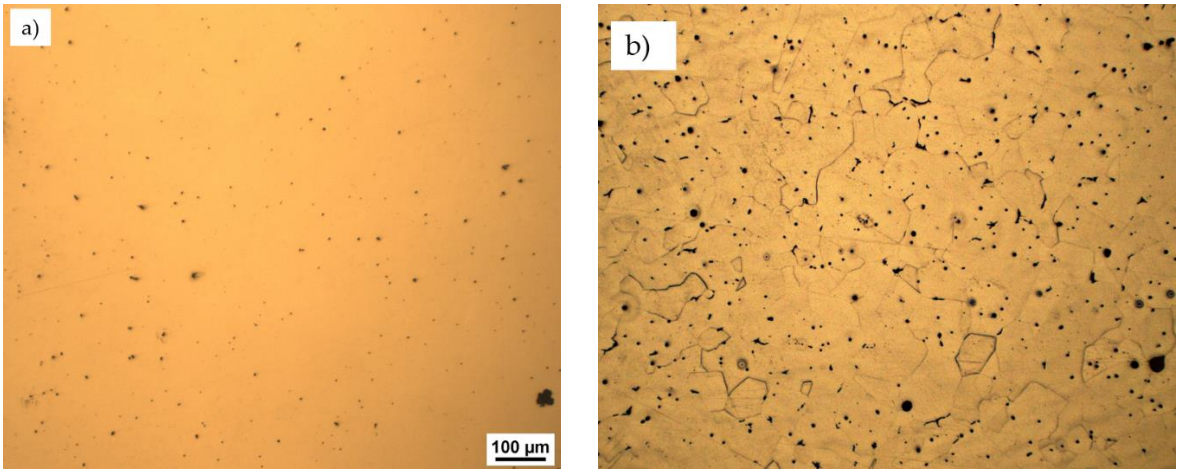

Figure 3.5 Novel alloy microstructure images taken with optical microscope at 20x.

In Figure 3.5 a) the sample is cutted from the column part of the bioinspired structure, no etching is applied and it shows the porosity of this steel in an as-cast solubilized conditon. Through this image, a value of porosity can be calculated. The image dimensions are 1147 × 960 pixels, so the total number of pixels is 1,101,120. Using image analysis to count the black pixels (representing pores/voids), the result is 10,287 black pixels. Porosity is the ratio of the pore area to the total image area, so the calculated porosity of the steel sample from this optical micrograph is approximately 0.94%. This value is an estimate based on the analysis of this single 2D cross-section. For a more accurate porosity measurement, analysis of multiple images at different locations and magnifications is recommended.

In Figure 3.5 b), the microstructure observed by LOM reveals a predominantly single-phase matrix characterized by equiaxed polygonal grains with well-defined grain boundaries. Considering the chemical composition of the alloy, the matrix can be identified as austenitic, as the high manganese content strongly stabilizes the austenite phase at room temperature. The solution heat treatment at 1050 °C followed by cooling promotes the dissolution of thermodynamically predicted secondary phases, resulting in a chemically homogenized microstructure and the absence of a continuous intermetallic network along grain boundaries. A homogeneous grain size distribution is observed throughout the field, indicating effective recrystallization and grain growth during the solubilization treatment. In addition to the austenitic matrix, a significant number of dark, rounded features with different size scales are visible and are uniformly distributed within the microstructure. These features are attributable to casting porosity and/or non-metallic inclusions.

While light optical microscopy provides a valuable initial assessment of the macroscale morphological features, it is inherently limited in its ability to resolve the true nature of the constituent phases, their chemical compositions, and the crystallographic orientations of individual grains. The contrast observed in LOM images arises primarily from differences in etching response and light reflectivity, which can lead to ambiguous interpretations, for instance, dark intragranular regions may be attributed to either microsegregated alloying elements, secondary phase precipitates, or even microvoids, without definitive confirmation.

3.2.2. SEM

While Light Optical Microscopy (LOM) provides an initial overview of the microstructure and reveals the presence of distinct morphological regions, it does not allow for precise elemental identification. Therefore, Scanning Electron Microscopy (SEM) combined with Energy Dispersive X-ray Spectroscopy (EDS) is employed in this study to investigate the chemical composition of the different microstructural constituents previously observed by LOM.

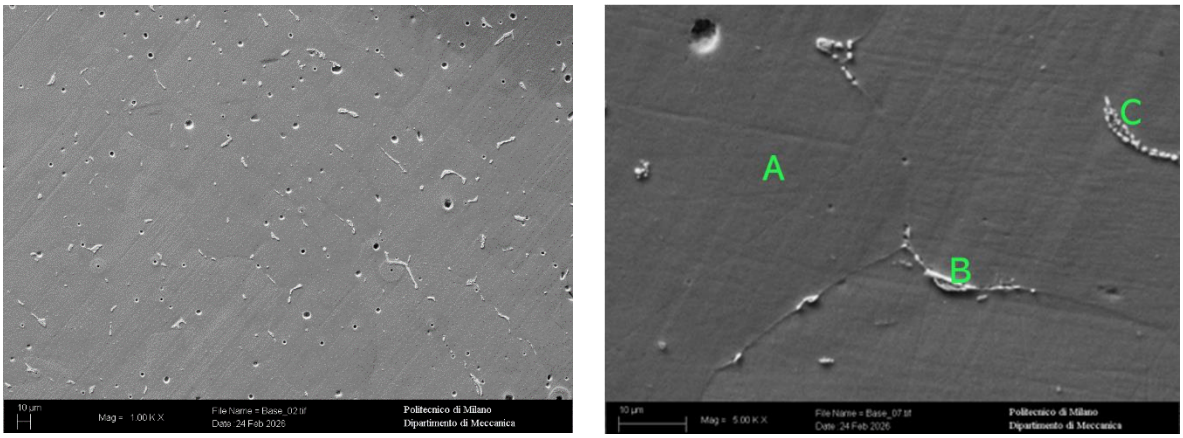

Figure 3.6 SEM images: 1000x magnification (left), 5000x magnification (right)

The SEM micrographs of the novel high-manganese steel reveal a heterogeneous microstructure composed of a continuous matrix phase (A), grain-boundary segregations (B), and finely dispersed intragranular precipitates (C). Quantitative EDS measurements indicate that the extended matrix region (A) contains approximately 21.02 wt.% Mn and 17.31 wt.% Cr, values that are in very good agreement with the nominal alloy composition. This chemical homogeneity, together with the morphology observed, confirms that the matrix is a γ-austenitic solid solution stabilized by the high manganese content. In contrast, the coarser blocky particles located preferentially along grain boundaries (B) exhibit a marked chromium enrichment, reaching about 33.996 wt.% Cr, accompanied by 19.45 wt.% Mn. This strong Cr partitioning relative to the surrounding matrix is characteristic of intermetallic phase formation in high Cr systems and is consistent with the presence of the σ phase. The smaller, more uniformly distributed intragranular particles (C) show a moderate chromium enrichment (≈24.06 wt.% Cr). Their size, morphology, and chemical signature suggest that they correspond to secondary precipitates, most likely a combination of $M_{23}C_6$ carbides and fine σ-phase particles.

Table 3.3 Chemical composition of particles observed from the SEM inspection

Name	Analysed Point	%Mn	%Cr	%Si	%Ni
As cast solubilized					
	A (austenite)	21.022	17.314	0.654	0.396
	B	19.445	33.996	-	0.486
	C	19.209	24.057	0.697	0.171

4 Results and discussion

This chapter presents and analyses the outcomes of both the numerical simulations and experimental investigations conducted in this work. The first section focuses on the finite element analyses performed using *Abaqus*, in which key mechanical and structural parameters were evaluated through simulation plots. These results are then compared with those obtained from *COMSOL Multiphysics*.

Subsequently, the chapter presents the results of manufacturing process regarding with the cast samples, beginning with pattern fabrication via 3D printing, followed by the investment casting procedure. The resulting cast components are then examined to evaluate their dimensional accuracy and surface quality. Finally, the experimental compression tests performed on the cast specimens are presented and discussed, enabling a direct comparison between the numerical predictions and the measured mechanical performance of the samples.

4.1. Numerical simulation results

From the numerical simulations, it is possible to obtain a preliminary prediction of the deformation behaviour of the loaded structure as well as an estimation of the reaction forces developed during loading. To define the material properties used in the simulations, the stress–strain data were extracted from the tensile test curve provided by *Alessandro Capitanio* and *Giorgio Carlesso* (Figure 3.3). These data were imported into *Microsoft Excel* for further analysis.

Upon examining the tensile curve, it was observed that the isotropic hardening behaviour of the material can be reasonably approximated as linear, since the stress–strain relationship increases linearly beyond the yield point. For a linear isotropic hardening model, the two principal parameters are the initial yield stress and the isotropic tangent modulus, which corresponds to the slope of the plastic portion of the tensile curve.

Through a linear interpolation of the data in the plastic region, these parameters were determined to be approximately 400 MPa for the initial yield stress and 2 GPa for the isotropic tangent modulus, as shown in Figure 4.1. Regarding the boundary conditions, a vertical displacement of 5 mm was applied to the upper surface of the specimen to simulate the loading condition during the compression test.

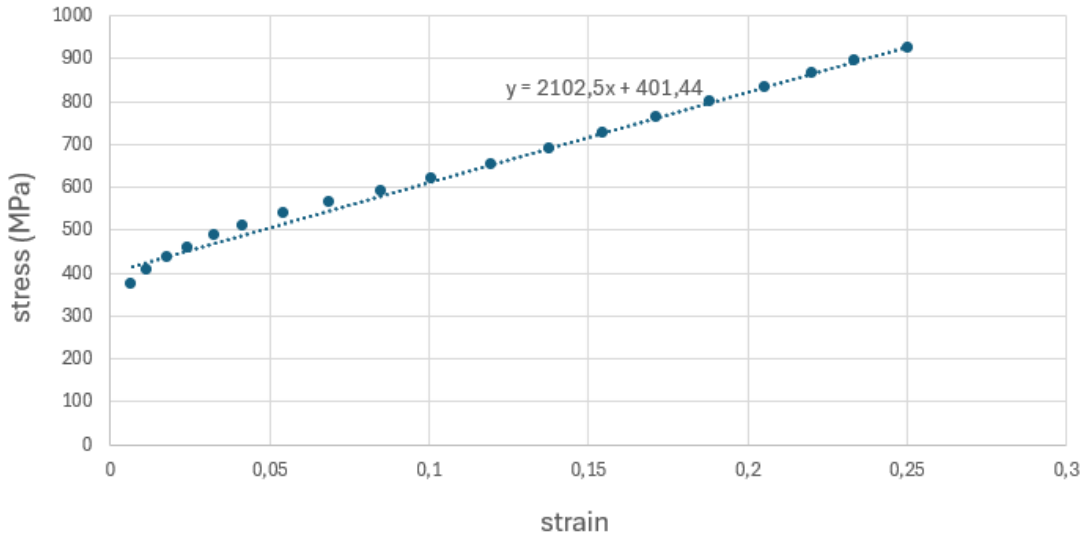

Figure 4.1 Plastic hardening curve of High Mn stainless steel.

4.1.1. Configuration A

In Figure 4.2, corresponding to the loading condition near the yielding point, the von Mises stress reaches values up to approximately 350 MPa, which is close to the assumed yield stress of the material (~ 400 MPa). The stress distribution reveals that the highest values are localized along the thin vertical columns, particularly around the edges of the openings. These regions represent the critical load-bearing elements of the structure, where plastic deformation is expected to initiate as the applied load increases.

The Figure 4.3 (left) shows the structure subjected to the full 5 mm vertical displacement imposed in the simulation. In this case, the von Mises stress rises significantly, with peak values reaching 1331 MPa, far above the material yield limit. The colour scale highlights the strong stress gradients along the slender columns. In Figure 4.4, highlight of the most stressed point in the deformed structure is shown.

The Figure 4.3 (right) illustrates the distribution of the equivalent plastic strain (PEEQ) in the deformed configuration. It represents the accumulated plastic strain in a material point, that is, how much permanent plastic deformation the material has undergone, regardless of the direction. The PEEQ values reach up to approximately 0.38, indicating significant accumulated plastic strain in localized areas. The highest concentrations are observed at the extremities of the buckled columns, where bending and local compression interact most intensely. These regions correspond well with the previously identified stress concentrations, predicting that failure initiation is likely to occur in these zones.

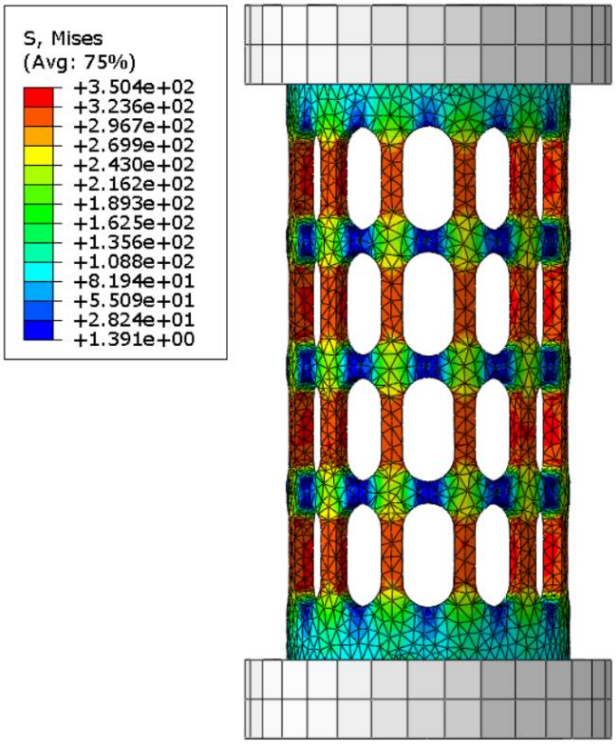

Figure 4.2 Compressed structure near the yielding point (configuration A)

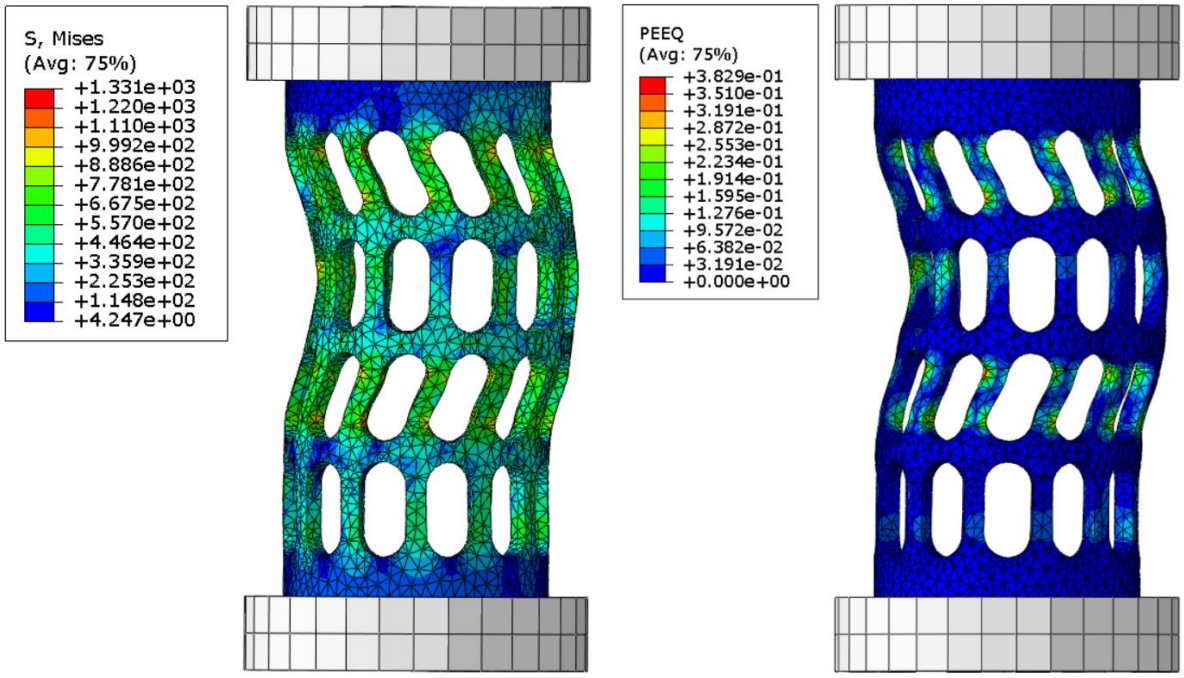

Figure 4.3 Deformed structure under 5mm vertical displacement: Von Mises stress (left); PEEQ - Equivalent Plastic strain (right).

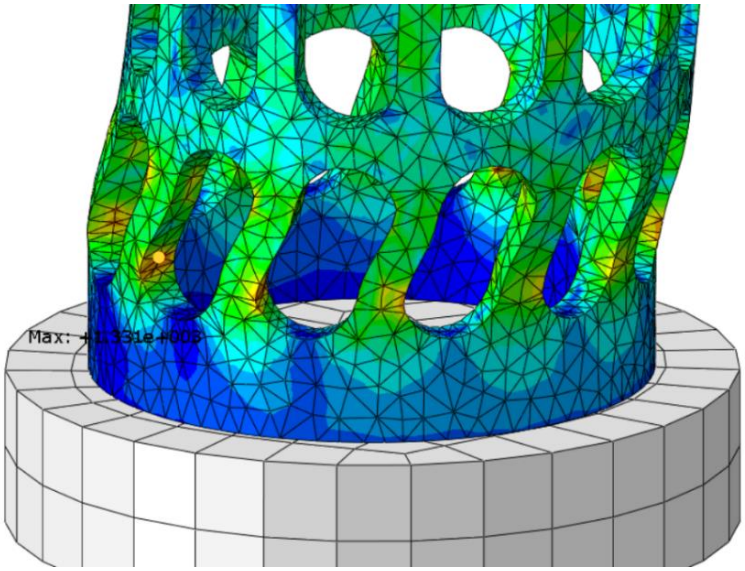

Figure 4.4 Highlight of the most stressed point in configuration A

The reaction force measured at the upper plate was extracted from the simulation results and plotted as a function of the imposed vertical displacement, as illustrated in Figure 4.5. The initial portion of the curve exhibits an approximately linear behaviour, corresponding to the elastic response of the structure, up to a load of about 46.7 kN. Beyond this point, the slope of the curve gradually decreases, indicating the onset of plastic deformation within the material. The reaction force continues to increase until reaching a maximum value of approximately 67.7 kN at a displacement of 1.85 mm, which represents the peak load capacity of the structure. After this maximum point, the applied load begins to decline, signifying the initiation of global buckling and the progressive loss of structural stiffness.

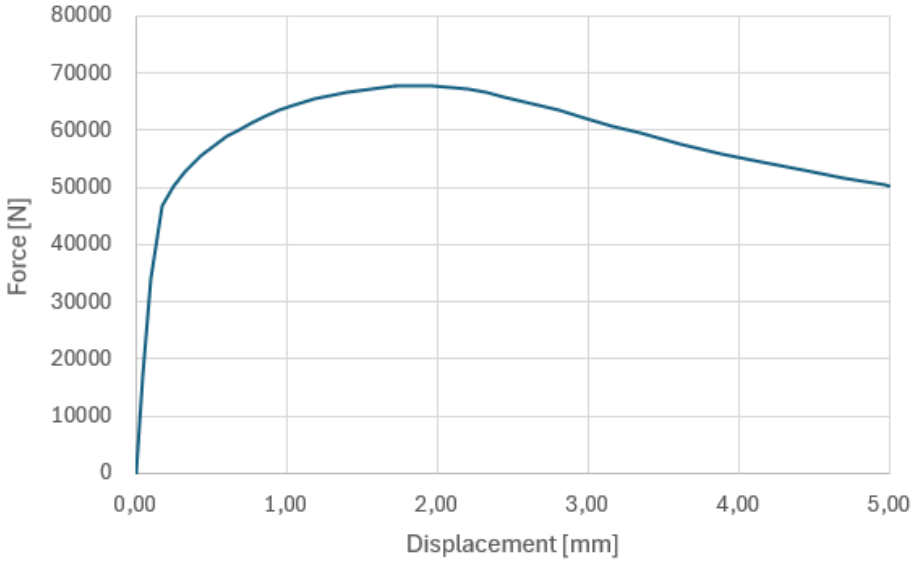

Figure 4.5 Reaction force curve obtained by numerical compression test (Configuration A)

4.1.2. Configuration B

In Figure 4.7, corresponding to the loading condition near the yielding point, the von Mises stress reaches 355 MPa, which is slightly lower than the assumed yield stress of the material (~ 400 MPa) so the structure is still in the elastic deformation region. The stress distribution reveals that the highest values are localized along the thin vertical columns, similar to previous configuration. These regions represent the critical load-bearing elements of the structure, where plastic deformation is expected to initiate as the applied load increases.

The Figure 4.8 (left) shows the structure subjected to the full 5 mm vertical displacement imposed in the simulation. In this case, the von Mises stress rises significantly, with peak values reaching 1296 MPa, slightly lower than configuration A. The colour scale highlights the strong stress gradients along the slender columns. In Figure 4.6, highlight of the most stressed point in the deformed structure is shown.

The Figure 4.8 (right) illustrates the distribution of the equivalent plastic strain in the deformed configuration. The PEEQ values reach up to approximately 0.417, indicating significant accumulated plastic strain in localized areas. The highest concentrations are observed at the extremities of the buckled columns, where bending and local compression interact most intensely. These regions correspond well with the previously identified stress concentrations, predicting that failure initiation is likely to occur in these zones.

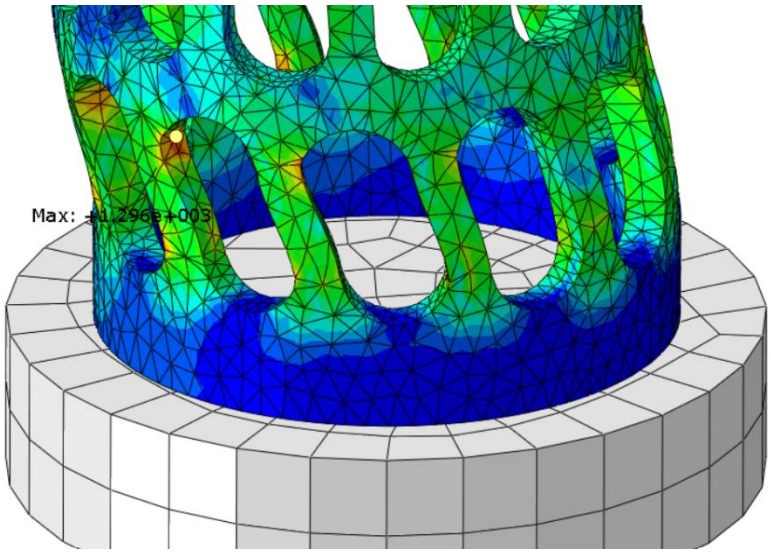

Figure 4.6 Highlight of the most stressed point in configuration B

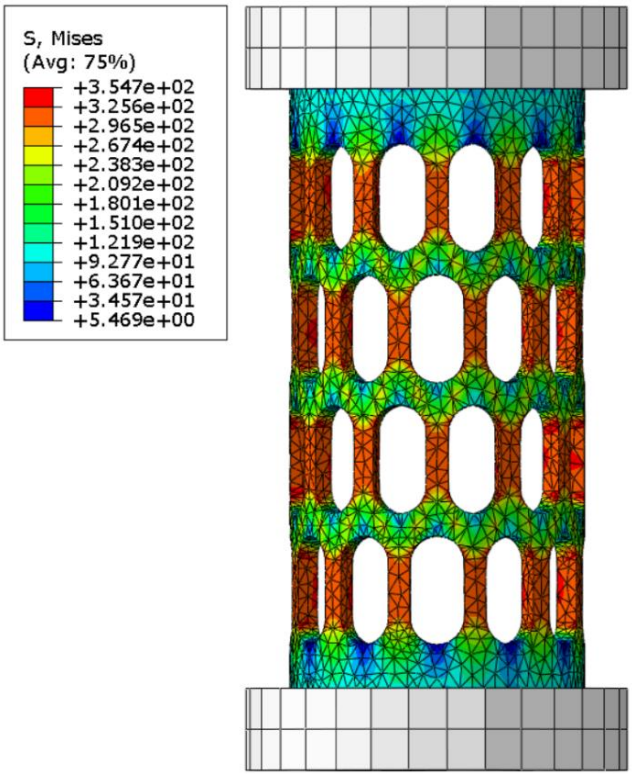

Figure 4.7 Compressed structure near the yielding point (configuration B)

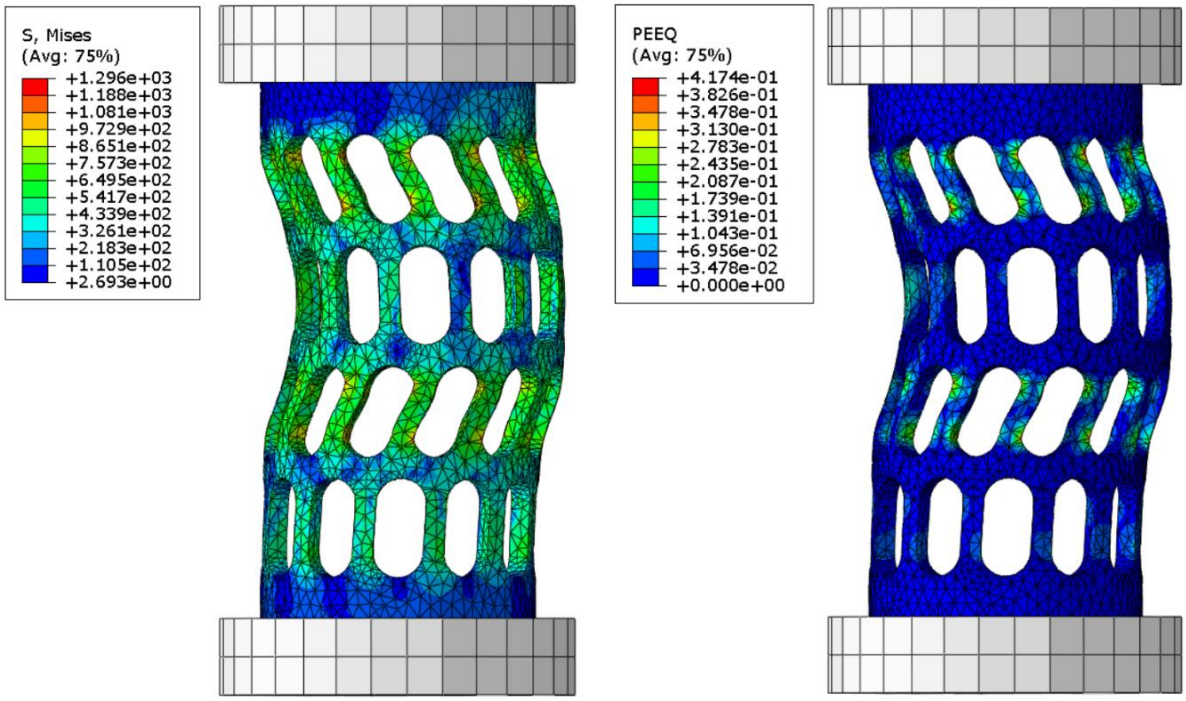

Figure 4.8 Deformed structure under 5mm vertical displacement: Von Mises stress (left); PEEQ - Equivalent Plastic strain (right).

The reaction force curve is similar to previous configuration, as shown in Figure 4.9. The initial portion of the curve exhibits an approximately linear behaviour, corresponding to the elastic response of the structure, up to a load of about 46.3 kN. Beyond this point, the slope of the curve gradually decreases, indicating the onset of plastic deformation within the material. The reaction force continues to increase until reaching a maximum value of approximately 67.7 kN at a displacement of 1.90 mm.

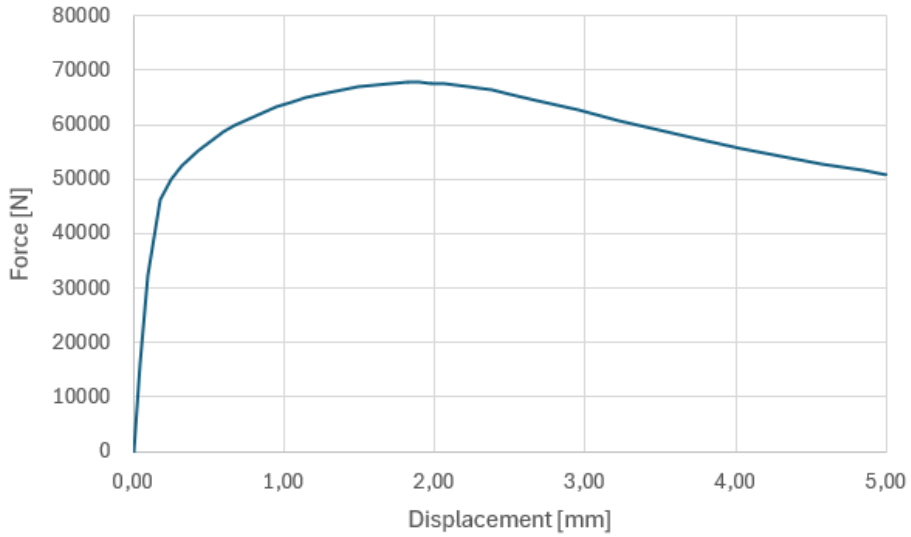

Figure 4.9 Reaction force curve obtained by numerical compression test (Configuration B)

4.1.3. Configuration C

In Figure 4.10, corresponding to the loading condition near the yielding point, the von Mises stress reaches 387 MPa. The stress concentration is primarily located at the extremities of the slotted holes, where the geometry induces localized stress amplification. Unlike the previous configurations, no global buckling is observed; instead, the inclined members behave like springs, effectively absorbing deformation and preventing out-of-plane instability.

Figure 4.11 (left) shows the structure subjected to the full 5 mm vertical displacement imposed in the simulation. In this case, the von Mises stress remains well distributed, with the highest value reaching 944 MPa. The stress gradients are mainly concentrated near the connection regions between the inclined columns, where local bending occurs. Figure 4.12 highlights the most stressed region of the deformed structure.

Figure 4.11 (right) illustrates the distribution of the equivalent plastic strain in the deformed configuration. The maximum PEEQ reaches approximately 0.24, indicating moderate plastic deformation localized in specific regions. These areas correspond to the zones of highest stress concentration, particularly where the inclined columns intersect, predicting that failure initiation is likely to occur in these zones.

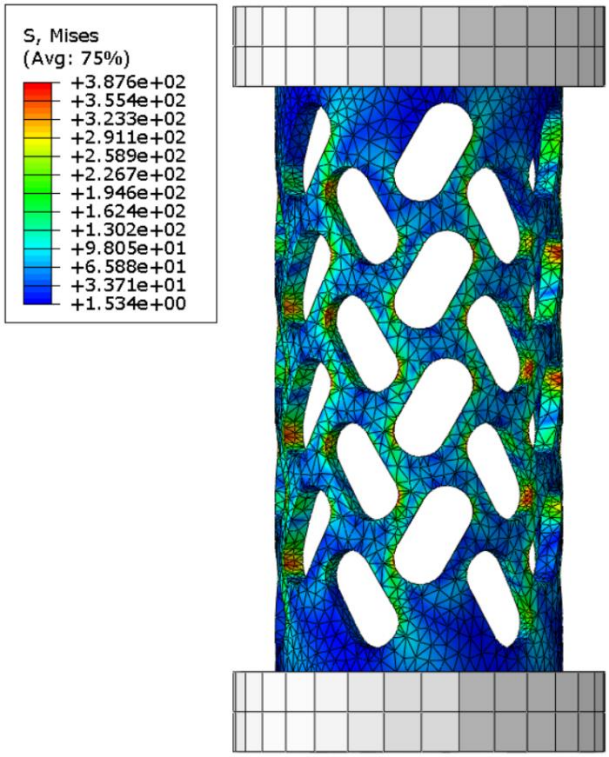

Figure 4.10 Compressed structure near the yielding point (configuration C)

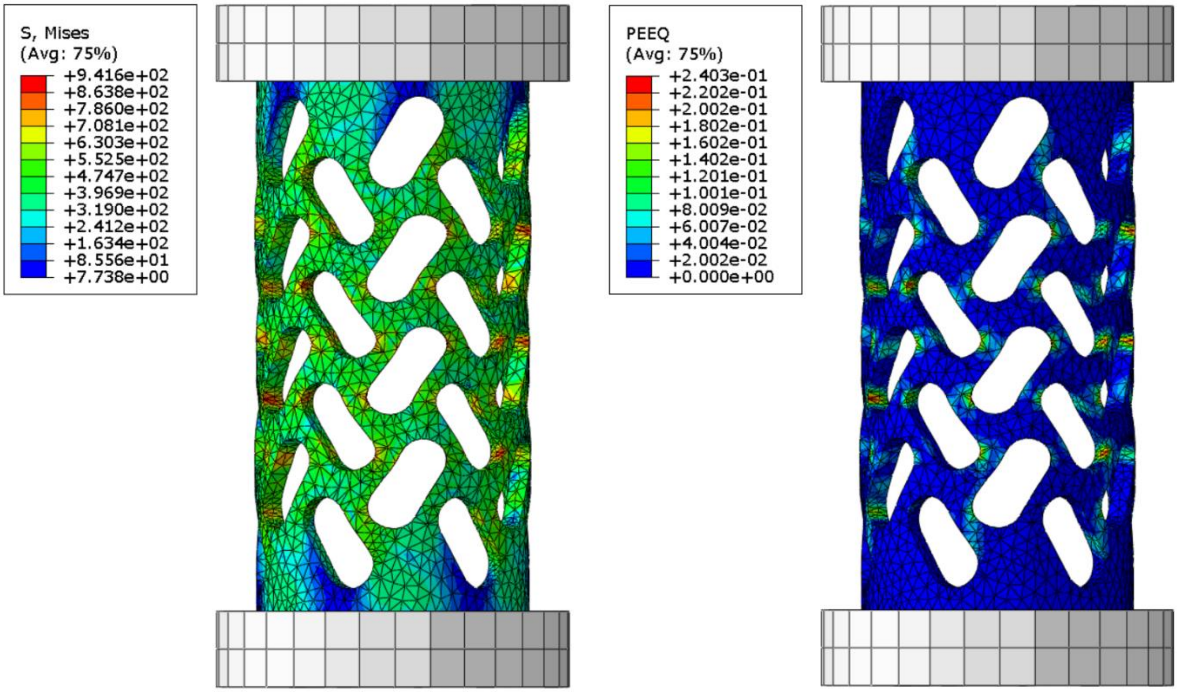

Figure 4.11 Deformed structure under 5mm vertical displacement: Von Mises stress (left); PEEQ - Equivalent Plastic strain (right).

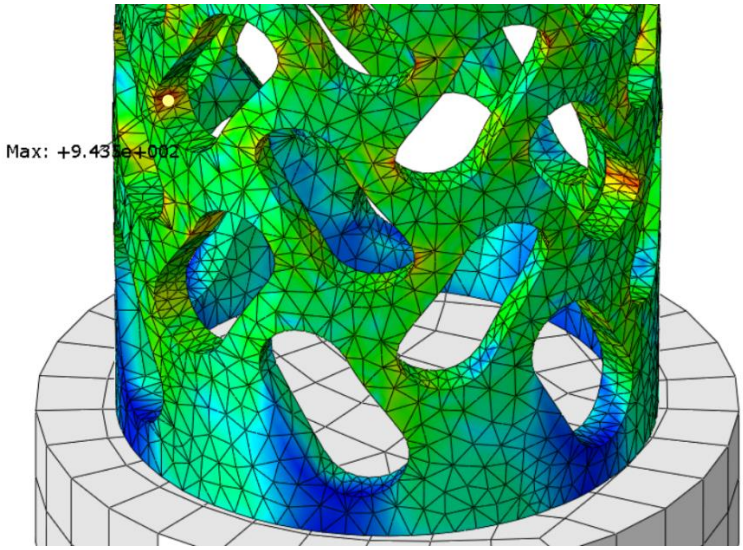

Figure 4.12 Highlight of the most stressed point in configuration C

The reaction force-displacement curve, shown in Figure 4.13, demonstrates a stable and continuous load-carrying capacity. The initial portion of the curve exhibits a nearly linear elastic response, followed by a gradual nonlinear increase as plasticity develops. The maximum reaction force is 34 kN and it is reached at an elongation of 5 mm, but the curve suggests that the structure could continue to sustain increasing loads beyond this point.

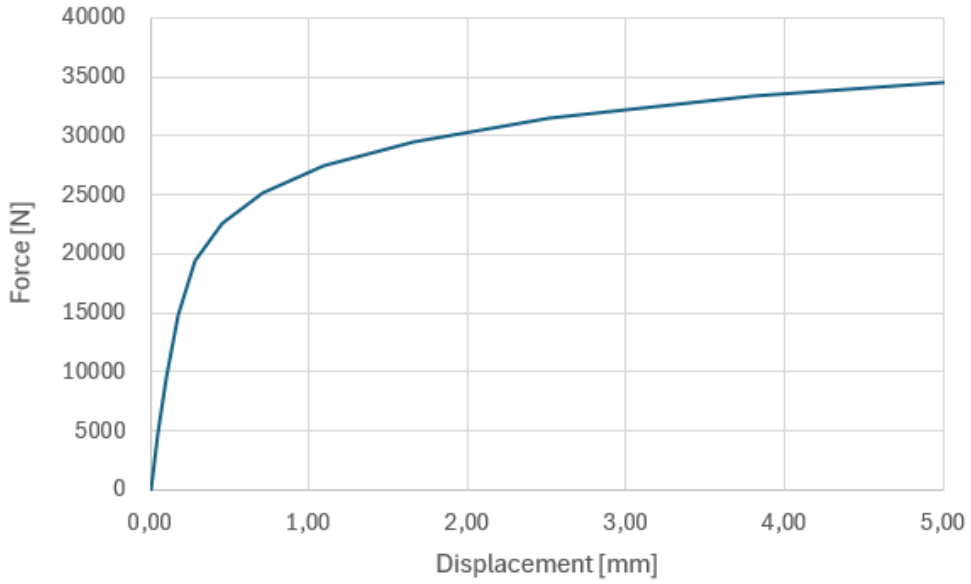

Figure 4.13 Reaction force curve obtained by numerical compression test (Configuration C)

4.1.4. Comparison

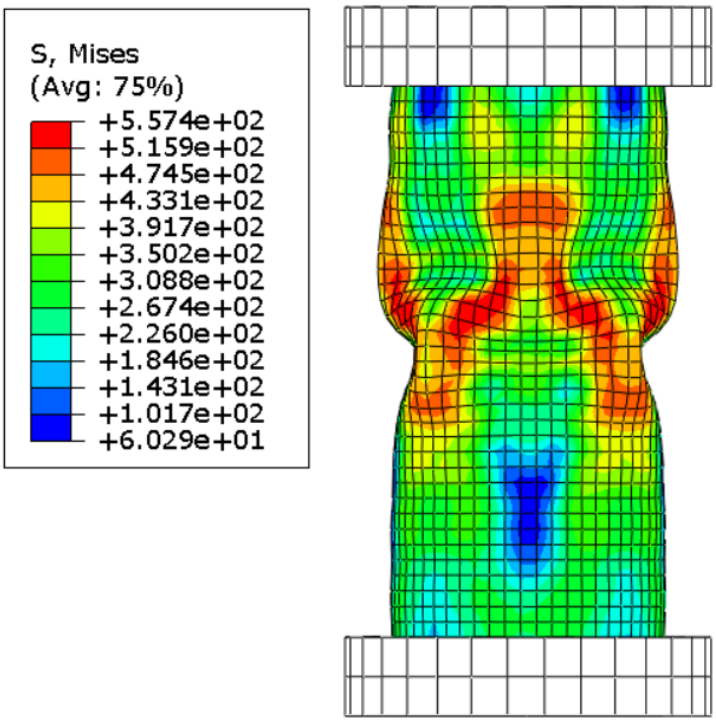

Figure 4.14 Von Mises stress distribution of a deformed hollow cylinder with the same volume of bioinspired structures.

In order to provide a direct benchmark for the compression behaviour of the bioinspired structures, an additional numerical simulation was performed on a hollow cylinder having the same height, the same external diameter and an equivalent material volume. The deformed configuration of the hollow cylinder under the same 5 mm imposed displacement used in the compression tests is shown in Figure 4.14. The comparison between the reaction force-displacement curves of the different structures (Figure 4.15) highlights a markedly different mechanical response. Although the hollow cylinder exhibits a higher initial reaction force, indicating a greater initial stiffness, once the material reaches the yielding point the curve becomes highly unstable after approximately 1 mm of displacement. This behaviour is attributed to the buckling of the thin cylindrical wall, which leads to a sudden loss of load-bearing capacity and to pronounced oscillations in the reaction force, in contrast with the more stable response observed for the bioinspired configurations.

Furthermore, the comparison among the bioinspired configurations highlights distinct mechanical responses. Configurations A and B exhibit a very similar behaviour in the initial and intermediate stages of loading, both reaching the same peak reaction force of approximately 68 kN at a displacement of 1.8 mm.

This result indicates a comparable load-bearing capability in the early deformation regime, which can be attributed to their analogous load transfer mechanisms and structural topology. Beyond this point, their responses begin to diverge: after about 3 mm of displacement, configuration B shows a more gradual reduction in reaction force, whereas configuration A undergoes a more pronounced decrease, suggesting an earlier onset of localized instability or damage. Additionally, these two configuration exibit a clear, asymmetric lateral buckling mode at final stage of loading. Configuration C, on the other hand, is characterised by a significantly lower reaction force throughout the simulated displacement range and does not reach a maximum value within the imposed 5 mm compression. This behaviour is strongly governed by its geometry, which promotes a more compliant response and allows the structure to deform in a manner similar to a spring, progressively storing deformation without exhibiting buckling effect.

In order to fully capture the mechanical response of these 3 configurations and to identify their actual maximum load and compression behaviour, experimental compression tests are performed. The corresponding results and their discussion are presented in the “Experimental Results” paragraph.

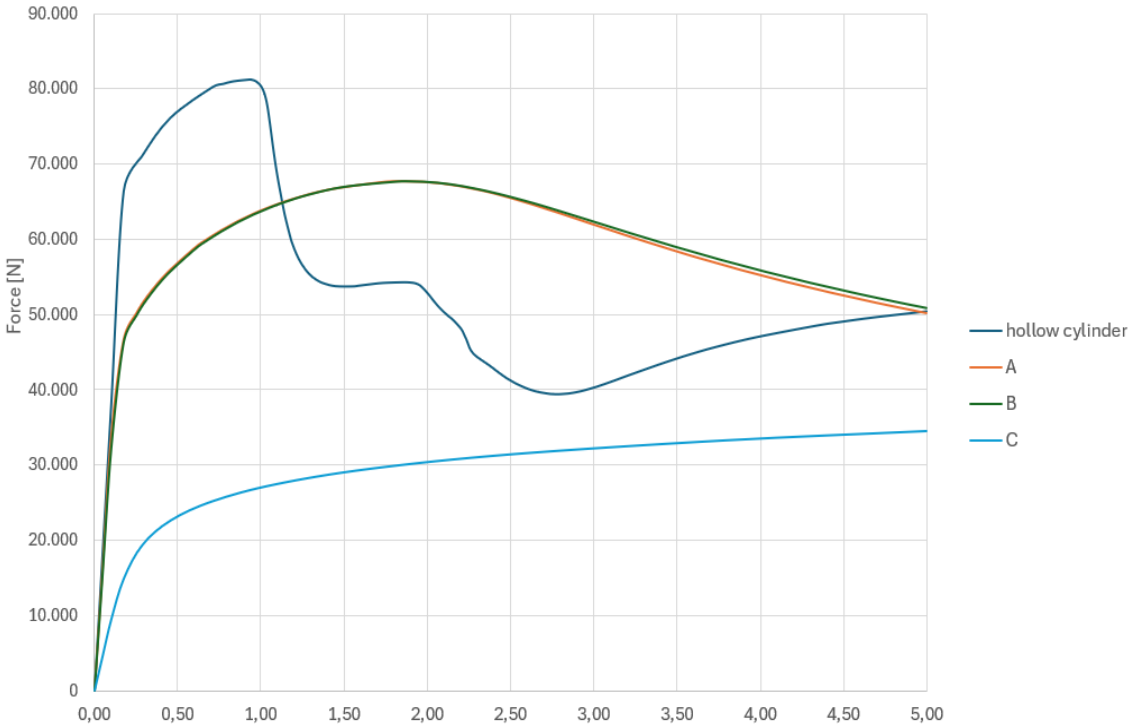

Figure 4.15 Reaction force curves of the hollow cylinder and the 3 different configurations.

4.1.5. COMSOL results

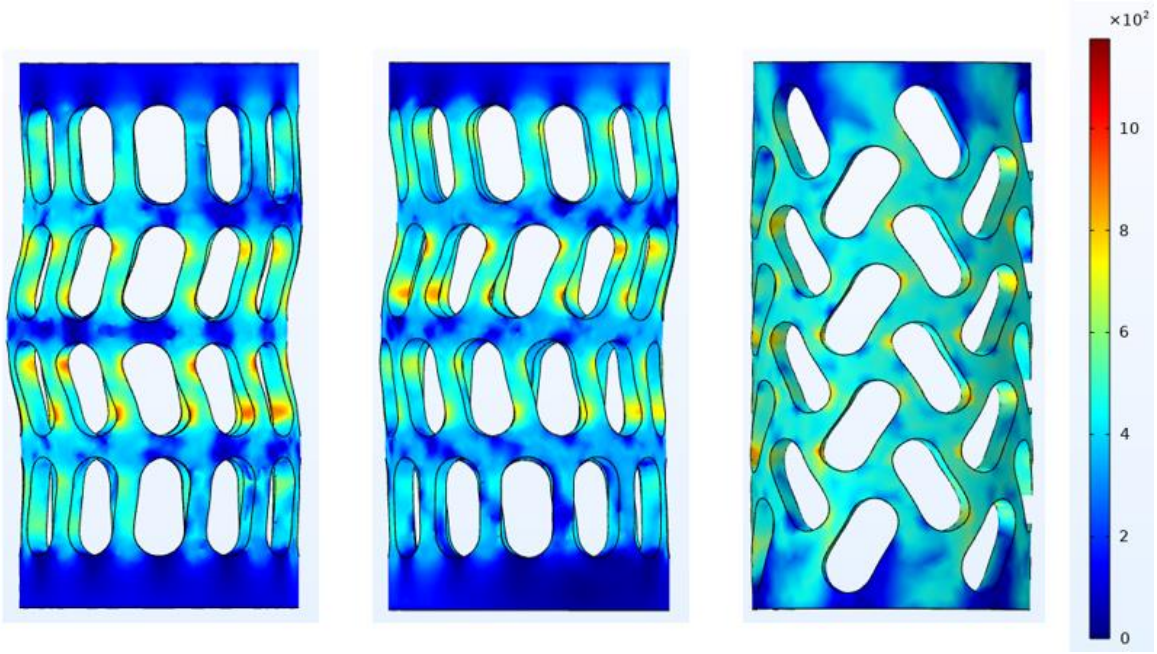

Figure 4.16 Deformed shapes obtained on COMSOL (values expressed in MPa)

In COMSOL Multiphysics, the same numerical compression test as previously implemented in Abaqus was reproduced. A vertical displacement of 5 mm was applied to the structures. However, in this simulation, the boundary conditions were directly imposed on the top and bottom surfaces of the specimen, without the inclusion of the pressing plates used in the Abaqus model.

As illustrated in Figure 4.16, the first two configurations exhibit different buckling behaviours compared to the Abaqus results. Specifically, the Abaqus simulations showed a C-shaped buckling mode, while in COMSOL, the deformation developed into an S-shaped buckling mode. This discrepancy can be attributed to the difference in boundary condition implementation: in Abaqus, the contact interaction with the rigid plates constrained the specimen's motion and influenced the deformation pattern, whereas in COMSOL the displacement and fixed constraints were directly applied to the specimen's surfaces, allowing for a different deformation response. The third configuration, on the other hand, did not exhibit any noticeable buckling, consistent with the behaviour observed in the Abaqus analysis.

The von Mises stress distribution confirms that the highest stress concentrations occur in the curved regions of the deformed pores. For configurations A and B, the maximum von Mises stress reached approximately 1200 MPa, while in configuration C, it was about 950 MPa.

4.2. Experimental results

The numerical simulations provided a first prediction of the mechanical response of the proposed bioinspired structures; nevertheless, an experimental validation is essential to assess their real behaviour. This chapter therefore presents the results of the experimental campaign conducted on the structures manufactured by investment casting. Initially, the geometrical fidelity of the cast components was evaluated by comparing the measured dimensions of the real specimens with the original CAD geometry, in order to quantify possible deviations introduced during the manufacturing process. The surface quality was assessed through a visual inspection, providing a qualitative evaluation of the overall surface finish and the presence of casting defects. Subsequently, the experimental compression tests were used to validate the Abaqus simulations. The compression tests were first performed under an imposed displacement of 5 mm, consistently with the numerical model, analysing both the deformation modes and the reaction forces. The investigation was then extended to compression up to failure for all three structural configurations, allowing the assessment of their actual load-bearing capacity and collapse mechanisms. Finally, a microstructural analysis of the deformed specimens was carried out to identify the active deformation mechanisms, such as slip bands, TWIP and/or TRIP (ε-martensite) effects, by means of light optical microscopy (LOM), with final confirmation provided by EBSD analysis to determine the crystallographic orientations and the corresponding phases present after deformation.

4.2.1. Casting results

The production of the real bioinspired structures in high-Mn steel was carried out by F.G.S. Foundry. The cast components were delivered in the as-cast condition and subsequently subjected to a solution heat treatment in an electric furnace at 1050 °C for 30 min, followed by water quenching in order to homogenise the chemical segregation generated during solidification. After the thermal treatment, the specimens were geometrically characterised by measuring their main dimensions and comparing them with the nominal values of the CAD models. The observed dimensional deviations between the cast products and the designed geometry can be attributed to several factors inherent to the investment casting process, such as solidification shrinkage, thermal contraction during cooling, wax pattern expansion, shell mould deformation at high temperature, and local variations in cooling rate caused by differences in section thickness.

In addition, the patterns used for the investment casting process are manufactured by Fused Deposition Modelling (FDM) 3D printing, the typical staircase effect and the filament deposition tracks characterising this process are transferred to the ceramic mould and consequently replicated on the surface of the final castings.

As a result, the produced structures exhibit a characteristic wave-like surface morphology, which can influence the overall surface quality.

Figure 4.17 Surface quality of casting product.

4.2.1.1. Configuration A

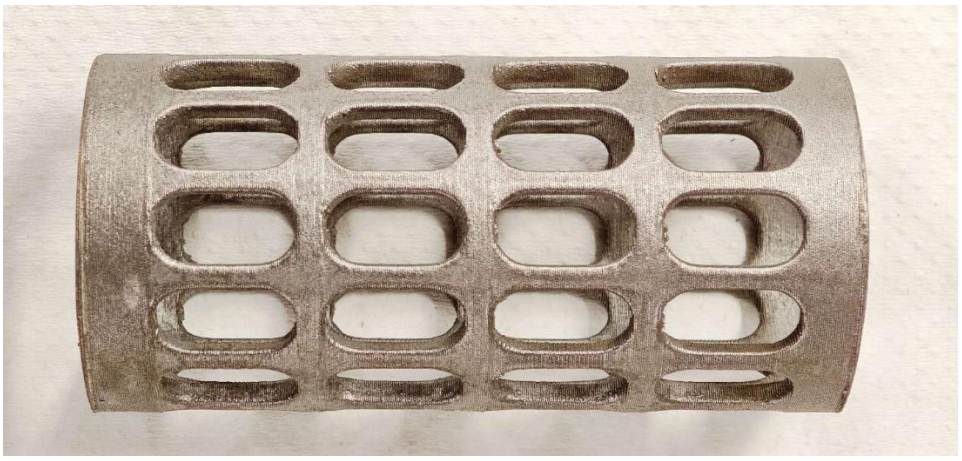

Figure 4.18 As cast bioinspired lattice structures (Configuration A)

For each characteristic dimension, multiple measurements were taken at different locations along the structure in order to account for possible local geometrical variations and to improve the reliability of the data. The acquired values were then averaged to obtain a representative mean dimension for each feature, reducing the influence of local surface irregularities and measurement uncertainty. These mean values were subsequently compared with the nominal dimensions of the CAD model and systematically reported in the corresponding tables.

The dimensional comparison reveals key insights into the fidelity of the investment casting process for such complex geometries.

The overall height of the casting (111.25 mm) exhibited a 1.14% increase relative to the CAD model (110 mm), while the external diameter (54.20 mm) showed a smaller deviation of 0.37% from the nominal 54 mm. In contrast, the wall thickness of the lattice structure demonstrated the most significant discrepancy, with the as-cast thickness (3.80 mm) being 5% thinner than the designed 4 mm. This variation in dimensional accuracy across different geometric features highlights the influence of process parameters on the final part geometry.

Table 4.1 Geometric accuracy analysis of cast product (Configuration A)

	CAD model	Casting	Relative error (%)
Height	110mm	111.25mm	+1.14
External diameter	54mm	54.20mm	+0.37
Thickness	4mm	3.80mm	-5

4.2.1.2. Configuration B

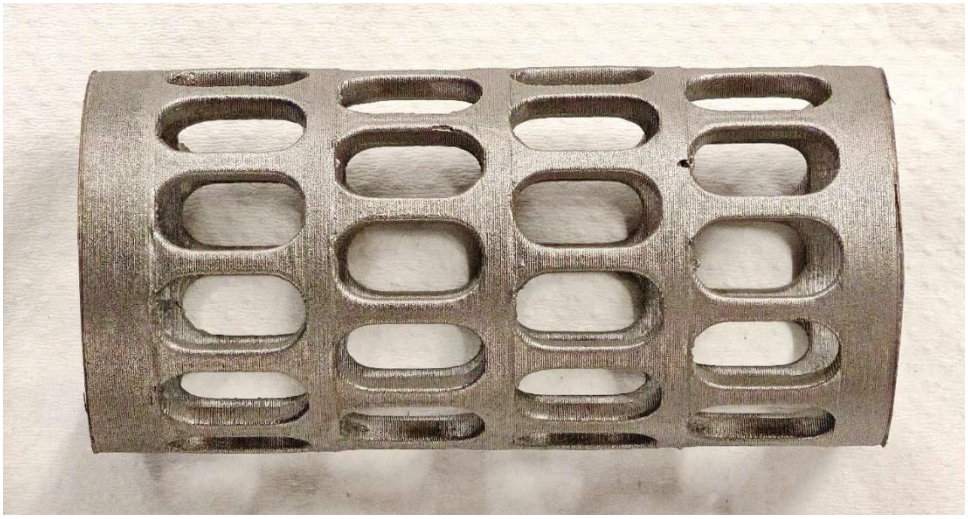

Figure 4.19 As cast bioinspired lattice structures (Configuration B)

The dimensional analysis reveals distinct accuracy trends: the overall height of the casting (110.95 mm) exhibited a 0.86% increase from the CAD design (110 mm), a lower relative error than observed in Configuration A. Conversely, the external diameter (54.75 mm) showed a more pronounced deviation of 1.38% from the nominal 54 mm, indicating greater radial expansion during solidification. Most notably, the thickness of the hollow cylinder's wall (4.30 mm) exceeded the designed 4 mm by 7.5%.

Table 4.2 Geometric accuracy analysis of cast product (Configuration B)

	CAD model	Casting	Relative error (%)
Height	110mm	110.95mm	+0.86
External diameter	54mm	54.75mm	+1.38
Thickness	4mm	4.30mm	+7.5

4.2.1.3. Configuration C

Figure 4.20 As cast bioinspired lattice structures (Configuration C)

The dimensional analysis reveals notable deviations: the overall height of the casting (108.50 mm) is 1.36% shorter than the CAD design (110 mm), representing the largest shrinkage error in height among all configurations. The external diameter (53.45 mm) exhibits a 1.02% reduction from the nominal 54 mm, indicating radial contraction. Most significantly, the thickness (3.75 mm) is 6.26% thinner than the designed 4 mm. These results highlight that the complex, interconnected topology of Configuration C introduces unique challenges to mold filling and solidification, leading to differential shrinkage and thickness reduction in the lattice struts.

Table 4.3 Geometric accuracy analysis of cast product (Configuration C)

	CAD model	Casting	Relative error (%)
Height	110mm	108.50mm	-1.36
External diameter	54mm	53.45mm	-1.02
Thickness	4mm	3.75mm	-6.26

4.2.2. Compression test results

To evaluate the real mechanical behaviour of the cast specimens, quasi-static compression tests were carried out using a servo-hydraulic testing machine. The experimental campaign was performed on an MTS system equipped with a 150 kN load cell. Prior to testing, two rigid steel plates with a surface area larger than the base of the samples were carefully positioned and fixed at the upper and lower ends of the machine. This configuration guaranteed proper alignment of the specimens and a uniform distribution of the compressive load, minimising local stress concentrations and preventing premature failure due to boundary effects.

Figure 4.21 Real compression test setup.

The experimental procedure was divided into two stages. In the first stage, the structures were compressed up to an imposed vertical displacement of 5 mm, in order to directly compare the experimental response with the numerical results obtained under the same loading condition. In the second stage, the tests were continued until failure, which was identified by the appearance of the first visible crack and the corresponding load drop in the force-displacement curve. This second set of tests allowed the identification of their compression behaviour and actual collapse mechanisms.

4.2.2.1. Configuration A

In the first stage, the structures were compressed up to an imposed vertical displacement of 5 mm. The specimen exhibits a clear, asymmetric lateral buckling mode, characterized by a significant lateral deflection along one primary axis. The struts show visible bending and localized deformation, particularly in the bottom section and upper section of the cylinder where the curvature is most pronounced. The middle section remain relatively undeformed.

The struts in the compressed side of the buckle show signs of plastic deformation, while those on the tensioned side appear stretched. The force-displacement response shows an initial linear elastic region up to approximately 1 mm displacement, followed by a peak force of around 53 kN at 1.5 mm, indicating the onset of plastic yielding and strut buckling. After the peak, the force gradually decreases, signifying progressive collapse of the lattice structure as displacement increases to 5 mm.

Figure 4.22 Deformed structure under 5mm compression displacement; Right: close-up view of deformed struts. (Configuration A)

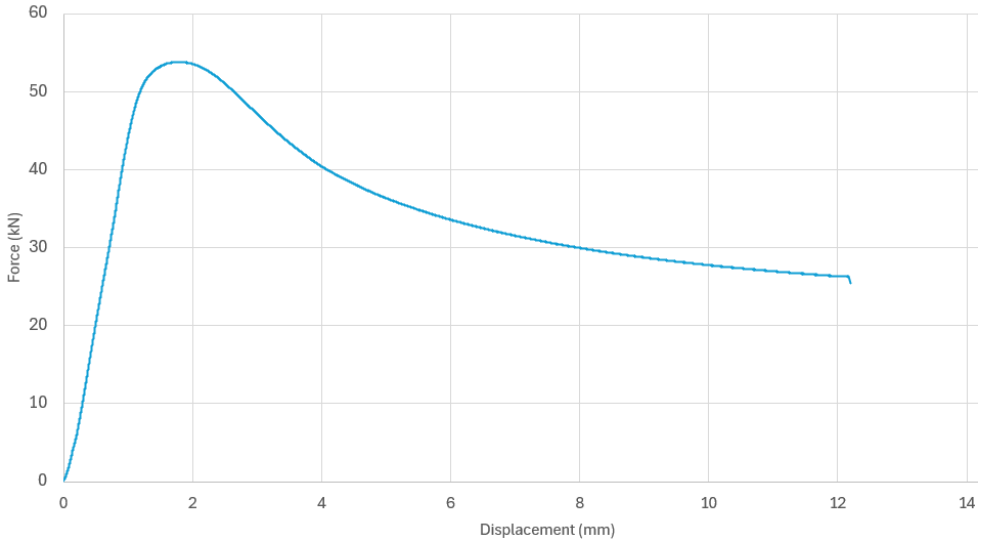

Figure 4.23 Reaction force curve up to failure (Configuration A)

In the second stage, the force gradually decreases until final failure at around 12.3 mm displacement, with a residual force of 26 kN. A close-up (Figure 4.24) reveals a clear crack at a strut-node junction, marking the onset of brittle fracture after significant plastic deformation.

Figure 4.24 Right: deformed structure at failure; left: close-up view of crack. (Configuration A)

4.2.2.2. Configuration B

Figure 4.25 Deformed structure under compression: 5mm displacement (left); 12mm displacement (right). (Configuration B)

In the first stage, the structures were compressed up to an imposed vertical displacement of 5 mm. The specimen exhibits a distinct lateral buckling mode, with asymmetric curvature developing along the cylinder's length. The struts show visible bending and localized deformation, particularly the bottom row and the third row counting from below of the cylinder where the curvature is most pronounced. The struts in the compressed side of the buckle show signs of plastic deformation, while those on the tensioned side appear stretched. Figure 4.25 (right) shows the deformed structure under 12mm compression displacement and conferms that struts of the bottom row and the third row are the most stressed. The force-displacement response (Figure 4.26) shows an initial linear elastic region up to approximately 1.7 mm displacement, followed by a peak force of around 55 kN at 2.2 mm, indicating the onset of plastic yielding and strut buckling. After the peak, the force gradually decreases, signifying progressive collapse of the lattice structure as displacement increases to 5 mm.

In the second stage, the force continues to decline until a secondary rise is observed around 22 mm displacement, followed by final failure at approximately 27 mm, with a residual force of 28 kN. As the lattice undergoes large-scale buckling and plastic deformation, initially bent struts may reorient and come into contact with adjacent struts. This contact creates new load paths and increases the effective cross-sectional area resisting compression, leading to a temporary increase in stiffness and reaction force. The deformed structure at failure (Figure 4.27) shows severe, localized buckling, with a close-up view revealing a clear crack at a strut-node junction, marking the transition from ductile buckling to brittle fracture after significant plastic deformation.

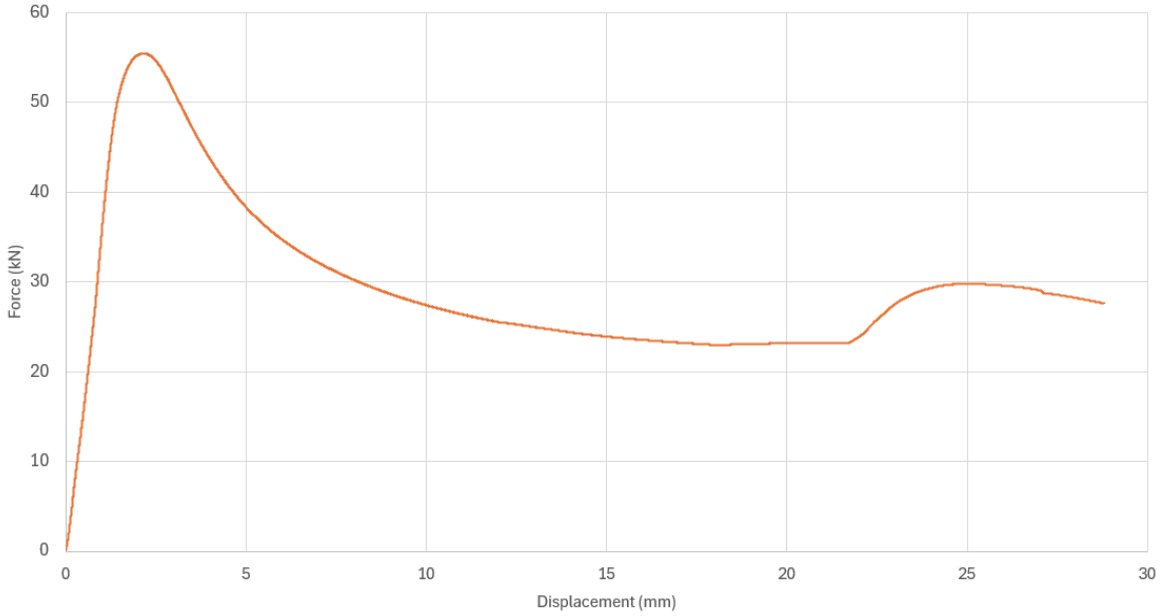

Figure 4.26 Reaction force curve up to failure (Configuration B)

Figure 4.27 Right: deformed structure at failure; left: close-up view of crack. (Configuration B)

4.2.2.3. Configuration C

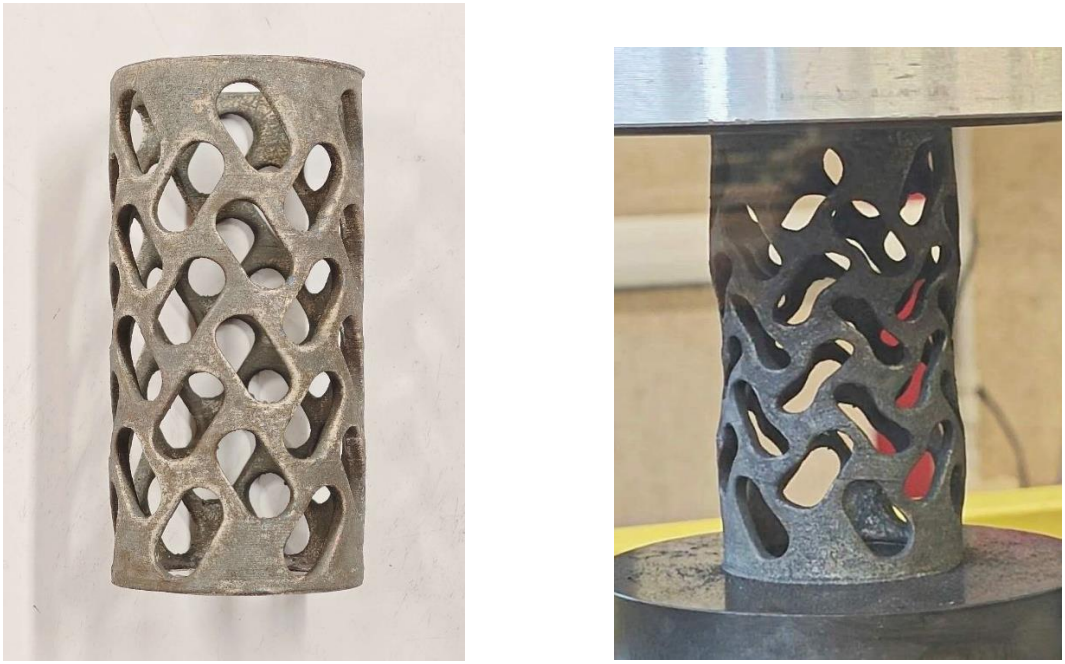

Figure 4.28 Deformed structure under compression: 5mm displacement (left); 12mm displacement (right). (Configuration C)

In the first stage, the structure was compressed up to an imposed vertical displacement of 5 mm. The specimen (Figure 4.28, left) exhibits a uniform, symmetric deformation mode, with the lattice struts bending in-phase making pores to form a cushion-like shape. This contrasts with the asymmetric buckling seen in Configurations A and B, a result of Configuration C's tilted pores arrangement. The force-displacement response (Figure 4.29) shows an initial linear elastic region up to approximately 1 mm displacement, followed by a gradual rise to a first plateau of 32 kN at 12 mm. The global buckling of this cylinder is characterized by a symmetric, multi-lobed deformation mode that forms two distinct protruding sections at the top and bottom, with a central shrunken waist. This creates a "hourglass" shape.

In the second stage, the structure continues to deform symmetrically, with struts folding and reorienting to maintain load-bearing capacity. The force curve shows a gradual decline to 28 kN at 21 mm, followed by a distinct secondary rise to a peak of 36 kN at 26 mm. This secondary rise is attributed to strut reorientation, contact between adjacent struts, and material strain hardening, which create new load paths and increase the effective stiffness of the deformed lattice.

Crack occurs at approximately 23 mm displacement, with a residual force of 35 kN. The deformed structure at failure (Figure 4.30) shows severe, symmetric folding of the lattice, with struts undergoing significant plastic deformation. A close-up view reveals a clear crack at the middle of a strut, marking the transition from ductile folding to brittle fracture after extensive plastic deformation. The overall behavior of Configuration C is characterized by a more gradual, distributed failure mode compared to Configurations A and B.

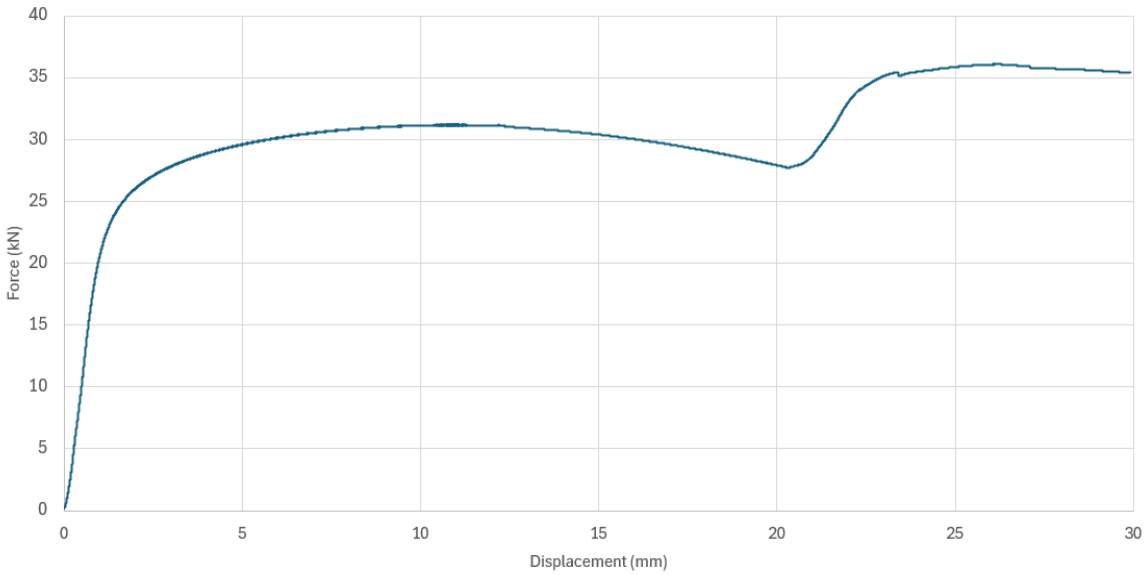

Figure 4.29 Reaction force curve up to failure (Configuration C)

Figure 4.30 Right: deformed structure at failure; left: close-up view of crack. (Configuration C)

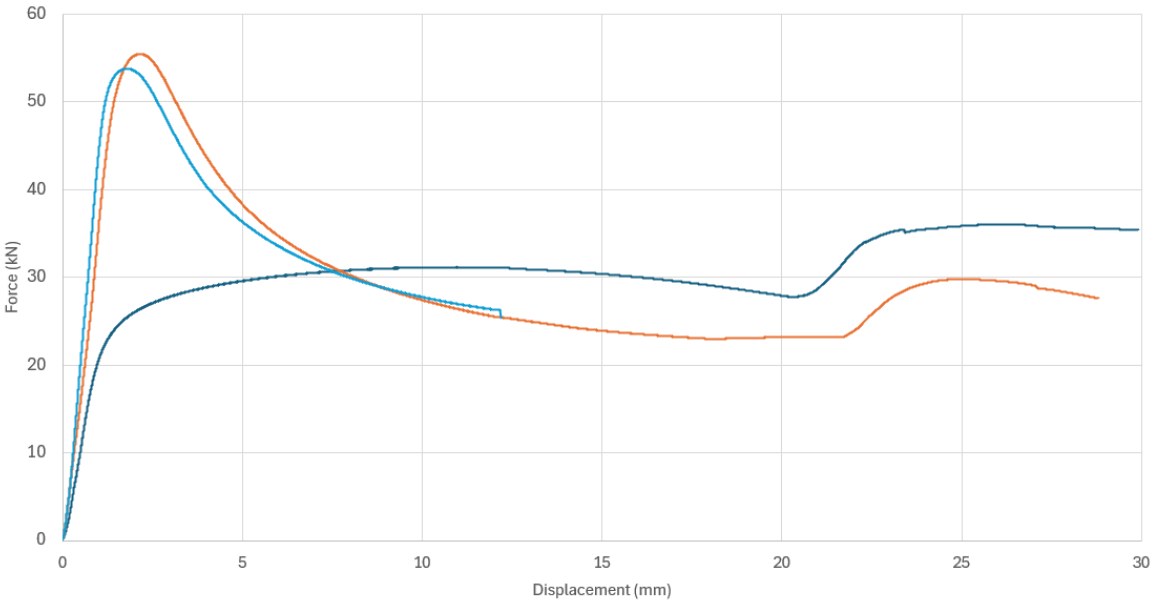

Figure 4.31 Comparison of reaction force curves of 3 configurations: Configuration A (light blue); Configuration B (orange); Configuration C (blue)

4.2.3. Microstructural analysis

Following the compression tests that revealed the mechanical behaviour of the structures under load, a microstructural analysis was conducted to examine the grain deformation mechanisms activated within specific regions. 5mm compression displacement deformed Configurations B and C were selected for this investigation, with two critical regions analysed for each: the base of the cylindrical structure, characterised by minimal stress exposure during compression, and the most severely deformed strut, which experienced the highest stress levels. Firstly, optical microscopy (LOM) was employed to assess grain size and shape qualitatively and identify potential deformation mechanisms. Subsequently, for the strut sample of Configuration B, scanning electron microscopy (SEM) was utilised to obtain higher-resolution observations of the microstructural features and electron backscatter diffraction (EBSD) was performed to check the phanses and structural evolution of the material following deformation.

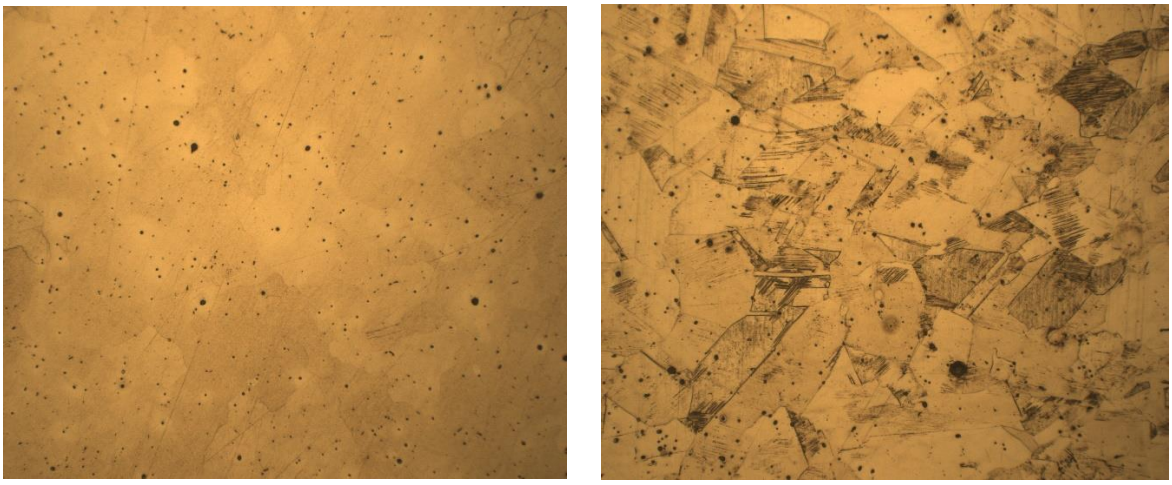

Figure 4.32 LOM images at 20x of deformed Configuration B: base sample (left), strut sample (right).

Figure 4.32 represent two distinct regions of deformed Configuration B. The left image shows the base sample of the cylindrical structure, which was exposed to minimal stress during compression. Its microstructure is relatively homogeneous, with large, mostly equiaxed grains and only a few scattered dark inclusions, reflecting limited deformation. In contrast, the right image depicts the strut sample, which experienced the highest stress levels. This region shows a highly deformed microstructure, characterized by elongated, flattened grains, extensive internal slip lines, and deformation bands, indicating significant plastic deformation and the activation of slip or twinning mechanisms. The stark contrast between the two images highlights the localized nature of deformation within the structure, where the strut underwent far more pronounced microstructural changes than the base.

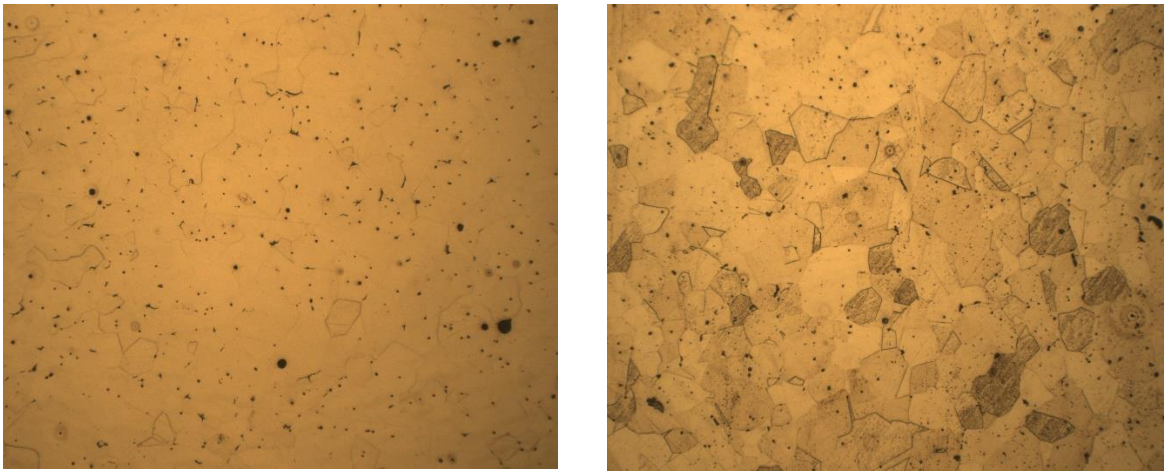

Figure 4.33 LOM images at 20x of deformed Configuration C: base sample (left), strut sample (right).

Configuration C exhibits a lower overall degree of deformation, which is reflected in both its base and strut samples. In the strut sample of Configuration C, the grains are more uniform in size and shape, with fewer pronounced deformation features, indicating that fewer deformation mechanisms were activated. In contrast, the strut sample of Configuration B shows a highly heterogeneous microstructure, characterized by extensively elongated and flattened grains, prominent slip lines, and deformation bands, which are clear signs of more intense plastic deformation and a greater variety of activated deformation mechanisms. This difference suggests that Configuration C experienced less severe localized strain during compression, leading to a more homogeneous microstructural response in the strut region.

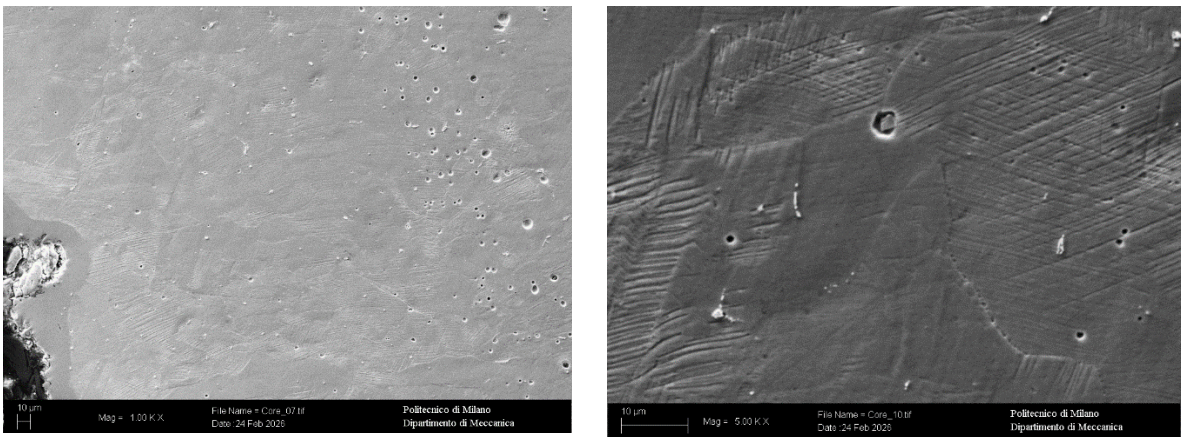

Figure 4.34 SEM images of strut's sample of Configuration B at most deformed point: 1000x magnification (left), 5000x magnification (right).

The 5000× magnification SEM image provides a detailed view of the deformation mechanisms active in the strut sample of Configuration B.

It clearly reveals a dense network of fine, parallel slip lines traversing the grain interior, these slip lines are well-defined and uniformly distributed, indicating extensive plastic deformation and the movement of dislocations along specific crystallographic planes. Additionally, subtle deformation bands can be observed, further confirming the intense localized strain experienced by this region.

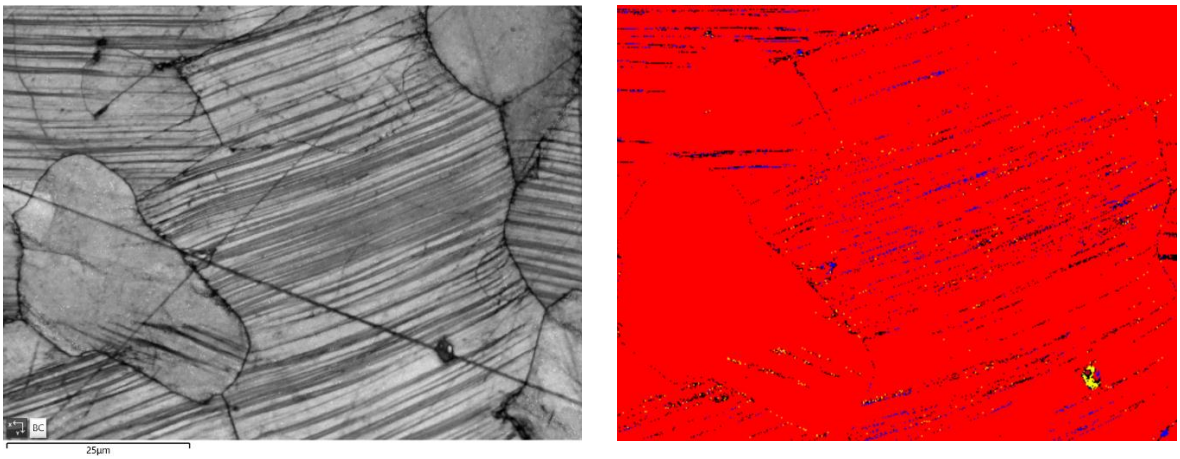

Figure 4.35 EBSD images at 3500x magification of strut's sample of Configuration B at most deformed point: phase color map (left), band contrast map (right).

The EBSD analysis of the strut sample from Configuration B provides critical insights into the material's microstructural evolution. The band contrast map (left) clearly reveals the presence of extensive deformation bands, which appear as dense, parallel linear features traversing the grain interiors and aligning with the slip lines observed in prior SEM analysis. The phase color map (right), predominantly red, confirms that the material remains primarily austenitic (FCC), but also identifies small, isolated regions of ε-martensite. The detection of this small amount of ε-martensite, formed via a deformation-induced phase transformation, indicates that after a 5 mm compression displacement, the deformation has triggered a Transformation-Induced Plasticity (TRIP) mechanism.

5 Conclusions

This thesis has investigated two complementary strategies for the development of lightweight high-manganese steels, addressing both alloy design and structural optimization in order to overcome the intrinsic density limitation of these materials. The study was motivated by the growing demand for structural solutions capable of combining high mechanical performance with mass reduction, particularly for applications in extreme environments where conventional alloying approaches are constrained. Through the integration of materials science, bioinspired design, numerical modelling, and experimental validation, the work has demonstrated that lightweight design in high Mn steels can be effectively achieved by acting simultaneously at the compositional and geometrical scales.

The first part of the research focused on the role of aluminium in Fe–Mn–Al–C steels as a means of reducing density while maintaining favourable mechanical properties. The analysis of the microstructural evolution and phase constitution confirmed the complex balance between austenite stabilization, κ-carbide precipitation, and the competing ferrite-forming tendency of aluminium. The experimental characterization of the newly developed alloy highlighted how the addition of Al leads to a significant reduction in density and enables high specific mechanical properties, although it also introduces critical aspects related to phase stability and microstructural control. These results underline that alloy design remains a powerful tool for lightweight engineering, but its applicability is strongly dependent on service conditions. In environments such as lead-cooled nuclear systems, where aluminium cannot be used due to its chemical reactivity and high-temperature behaviour, density becomes a fixed parameter and weight reduction must be achieved through structural design.

For this reason, the second part of the thesis explored the use of bioinspired geometries derived from the hierarchical structure of the cholla cactus skeleton as an alternative strategy for lightweight design in dense, Al-free high-Mn steels. The finite element simulations demonstrated that the introduction of a cellular architecture allows a significant improvement in stiffness-to-weight ratio and energy absorption compared to conventional hollow cylinders with the same volume. The numerical investigation made it possible to identify the influence of the different geometrical configurations on the mechanical response, highlighting the role of wall thickness distribution and pores arrangement in determining the global compressive behaviour.

A fundamental aspect of this work is the experimental validation of the numerical models. The structures were successfully manufactured through additive manufacturing and subsequent investment casting, proving the technological feasibility and scalability of the proposed design. Despite the geometrical complexity and the thin-walled configuration, the casting process produced components with good structural integrity, demonstrating the compatibility of high Mn steels with advanced manufacturing techniques for lightweight applications. The compression tests showed a remarkable agreement with the numerical predictions. In particular, the deformed shapes at a displacement of 5 mm were perfectly replicated in the real experiments, confirming that the simulation accurately captured the collapse mechanisms and the progressive deformation of the cellular architecture.

A very good correlation was also observed in the reaction force-displacement curves. The numerical and experimental curves exhibited the same overall trend, including the initial elastic response, the onset of instability, and the subsequent progressive collapse. The difference in the absolute force values, with the experimental results showing lower forces, can be attributed to the different material properties used in the simulations and in the real tests. In the numerical model, the constitutive behaviour of the high-Mn stainless steel (alloy B) taken from *Alessandro Capitanio* and *Giorgio Carlesso*'s previous work was adopted, whereas the experimentally tested structures were produced using a newly developed high-Mn steel. This difference in mechanical properties naturally led to a dissimilarity in the measured force levels, while preserving the overall mechanical response and deformation mode.

Overall, the results of this thesis demonstrate that the combination of advanced alloy development and bioinspired structural design represents a versatile and effective approach for achieving lightweight, high-performance components. When aluminium can be used, alloy design enables a direct reduction in density while maintaining excellent mechanical properties. When aluminium is not allowed and the material density is fixed, bioinspired geometrical optimization provides a powerful alternative, allowing significant mass reduction without compromising load-bearing capacity.

Future research could further refine the constitutive models for the new alloy, extend the investigation to dynamic and cyclic loading conditions, and explore the optimization of hierarchical geometries to fully exploit the synergy between material and structure.

Bibliography

[1] R. Singh, "Applied Welding Engineering," pp. 7-11, 2012.

[2] M. Lin, Y. Wang, Z. Yu, Z. Zhao, Y. Li and C. Chen, "A novel high-Mn steel with high corrosion resistance," *Journal of Materials Research and Technology,* vol. 38, p. 3387–3400, 2025.

[3] S. Allain, O. Bouaziz, T. Lebedkina and M. Lebyodkin, "Relationship between relaxation mechanisms and strain aging," *Scripta Materialia,* vol. 64, p. 741–744, 2011.

[4] S. Chen, R. Rana, A. Haldar and R. K. Ray, "Current state of fe-mn-al-c low density steels," *Progress in Materials Science,* vol. 89, p. 345–391, 2017.

[5] D. Raabe, C. C. Tasan and E. A. Olivetti, "Strategies for improving the sustainability of structural metals," *Nature,* 2019.

[6] R. Tucker, "Trends in automotive lightweighting," *Met Finish,* 2013.

[7] D. W. Suh and N. J. Kim, "Low-density steels," *Scripta Materialia,* vol. 68, p. 337–338, 2013.

[8] Frommeyer G. , Drewes EJ. and Engl B., "Physical and mechanical properties of iron-aluminium-(Mn, Si) lightweight steels," *Rev Met Paris,* vol. 97, p. 1245–1253, 2000.

[9] R. R. Jom, "Low-density steels," *SpringerR RanaJom,* vol. 66, p. 1730–1733, 2014.

[10] Chu CM., Huang H., Kao PW. and Gan D., "Effect of alloying chemistry on the lattice constant of austenitic Fe-Mn-Al-C alloys," *Scripta Metall Mater,* vol. 30, p. 505–508, 1994.

[11] C.H. Seo, K.H. Kwon, K. Choi, K.H. Kim and J.H. Kwak, "Deformation behaviour of ferrite–austenite duplex lightweight Fe–Mn–Al–C steel," *Scr. Mater,* vol. 66, p. 519–522, 2012.

[12] H. Kim, D.W. Suh and N.J. Kim, "Fe–Al–Mn–C lightweight structural alloys: A review on the microstructures and mechanical properties," *Sci. Technol. Adv. Mater,* vol. 14, p. 1–11, 2013.

[13] Kubaschewski O., "Iron—binary phase diagrams," *1st ed. Berlin: Springer-Verlag,* 1982.

[14] N.S. Stoloff, "Iron aluminides: Present status and future prospects," *Mater. Sci. Eng,* vol. A258, p. 1–14, 1998.

[15] Koster W. and Tonn W., "The iron corner of the iron-manganese-aluminum system," *Arch Eisenhüttenwes,* vol. 7, p. 365–6, 1933.

[16] J. Benz and H. Leavenworth Jr, "An assessment of fe-mn-al alloys as substitutes for stainless steels," *Jom,* vol. 37, p. 36–39, 1985.

[17] Y. Kimura, K. Handa, K. Hayashi and Y. Mishima, "Microstructure control and ductility improvement of the two-phase γ-Fe/κ-(Fe, Mn)3AlC alloys in the Fe–Mn–Al–C quaternary system," *Intermetallics,* vol. 12, p. 607–617, 2004.

[18] C. Mapelli, G. Villa, S. Barella, A. Gruttadauria, A. Gruttadauria, D. Mombelli , X. Veys and L. Duprez, "Jmak model applied on the κ-carbide precipitation in femnalc steels," *Journal of Materials Research and Technology,* vol. 15, p. 3386–3398, 2021.

[19] K.H. Han, J.C. Yoon and W.K. Choo, "TEM evidence of modulated structure in Fe-Mn-Al-C austenitic alloys," *Scr. Metall,* vol. 20, p. 33–36, 1986.

[20] Kayak GL, " Fe–Mn–Al precipitation-hardening austenitic alloys," *Met Sci Heat Treat,* vol. 11, p. 95–97, 1969.

[21] Han KH, Yoon JC and Choo WK, "TEM evidence of modulated structure in FeMnAlC austenitic alloys," *Scr Metall,* vol. 20, p. 33–36, 1986.

[22] Acselrad oKalashnikov I, Silva E, Khadyev M, Simao, Acselrad O., Kalashnikov I., Silva E., Khadyev M. and Simao R., "Diagram of phase transformations in the austenite of hardened alloy Fe-28% Mn-8.5% Al-1% C-1.25% Si as a result of aging due to isothermal heating," *Met Sci Heat Treat,* vol. 48, p. 543–53, 2006.

[23] Cheng WC., Song YS., Lin YS., Chen KF. and Pistorius P., "On the eutectoid reaction in a quaternary Fe-C-Mn-Al alloy: austenite to ferrite+kappa-carbide+M23C6 carbide," *Metall Mater Trans A,* vol. 45A, p. 1199–1216, 2014.

[24] Cheng WC., Cheng CY., Hsu CW. and Laughlin DE. , "Phase transformation of the L12 phase to kappa-carbide after spinodal decomposition and ordering in a Fe–C–Mn–Al austenitic steel," *Mater Sci Eng A,* vol. 642, p. 128–35, 2015.

[25] H. Kim., D. W. Suh and N. J. Kim, "Fe-al-mn-c lightweight structural alloys: A review on the microstructures and mechanical properties," *Science and Technology of Advanced Materials,* vol. 14, 2013.

[26] J. Moon, S.-J. Park, J. H. Jang, T.-H. Lee, C.-H.Lee, H.-U. Hong, D.-W. Suh and S. H. Kim, "Atomistic investigations of κ-carbide precipitation in austenitic fe-mn-al-c lightweight steels and the effect of mo addition," *Scripta Materialia,* vol. 127, p. 97–101, 2017.

[27] K. Chang, C. Chao and T. Liu, "Excellent combination of strength and ductility in an fe–9a-28mn–1.8 c alloy," *Scripta Materialia,* vol. 2012, p. 162–165, 63.

[28] K. Choi, C.-H. Seo, H. Lee, S. Kim, K. G. Chin, K.-T. Park and N. J. Kim, "Effect of aging on the microstructure and deformation behavior of austenite base lightweight fe–28mn–9al-0.8 c steel," *Scripta Materialia,* vol. 10, p. 1028–1031, 2010.

[29] C.-H. Seo, K. H. Kwon, K. Choi, K.-H. Kim, J. Kwak, S. Lee and N. J. Kim, "Deformation behavior of ferrite–austenite duplex lightweight fe–mn–al–c steel," *Scripta Materialia,* vol. 66, pp. 519-522, 2012.

[30] O. Balancin, W. Hoffmann and J. Jonas, "Influence of microstructure on the flow behavior of duplex stainless steels at high temperatures," *Metallurgical and materials transactions A,* vol. 31, p. 1353–1364, 2000.

[31] S. Y. Shin, H. Lee, S. Y. Han, C.-H. Seo, K. Choi, N. J. Kim, J.-H. Kwak and K.-G. Chin,, "Correlation of microstructure and cracking phenomenon occurring during hot rolling of lightweight steel plates," *Metallurgical and Materials Transactions A,* vol. 41, p. 138–148, 2010.

[32] G. Frommeyer, E.J. Drewes and B. Engl, "Physical and mechanical properties of iron-aluminium-(Mn, Si) lightweight steels," *Rev. Met. Paris,* vol. 97, p. 1245–1253, 2000.

[33] A. Zargaran, H. Kim, J.H. Kwak and N.J. Kim, "Effects of Nb and C additions on the microstructure and tensile properties of lightweight ferritic Fe–8Al–5Mn alloy," *Scr. Mater.,* vol. 89, p. 37–40 , 2014.

[34] I. Gutierrez-Urrutia and D. Raabe, "High strength and ductile low density austenitic FeMnAlC steels: Simplex and alloys strengthened by nanoscale ordered carbides," *Mater. Sci. Technol.,* vol. 20, p. 1099–1104, 2014.

[35] Bausch M., Frommeyer G., Hofmann H., Balichev E., Soler M. and Didier M., "Ultra high-strength and ductile FeMnAlC light-weight steels.," 2009.

[36] Cheng WC., Cheng CY. and Hsu CW., "Phase transformation of the L12 phase to kappa-carbide after spinodal decomposition and ordering in a Fe–C–Mn–Al austenitic steel," *Mater Sci Eng A,* vol. 642, p. 128–35, 2015.

[37] O.A.Zambrano, "A general perspective of Fe–Mn–Al–C steels," *J Mater Sci,* vol. 53, p. 14003–14062, 2018.

[38] Chen FC., Chou CP., Li P. and Chu SL, "Effect of aluminium on TRIP FeMnAl alloy steels at room temperature," *Mater Sci Eng A,* vol. 160(2), p. 261–270, 1993.

[39] Wong SL., Madivala M., Prahl U., Roters F. and Raabe D., "A crystal plasticity model for twinning- and transformation induced plasticity," *Acta Mater,* vol. 118, p. 140–151, 2016.

[40] Yoo JD. and Park K-T., "Microband-induced plasticity in a high Mn–Al–C light steel," *Mater Sci Eng A,* vol. 496(1–2), p. 417–424, 2008.

[41] Welsch E., Ponge D., Hafez Haghighat SM., Choi P., Herbig M., Zaefferer S. and Raabe D., "Strain hardening by dynamic slip band refinement in a high-Mn lightweight steel," *Acta Mater,* vol. 116, p. 188–199, 2016.

[42] Sang-Heon Kim., Hansoo Kim and Nack J. Kim, "Brittle intermetallic compound makes ultrastrong low-density steel with large ductility," *Nature,* vol. 518, pp. 77-79, 2015.

[43] E. Tempelman, "Lightweight Materials, Lightweight Design," *Materials Experience: Fundamentals of Materials and Design,* p. 247–258, 2013.

[44] M. F. Ashby, "Overview No. 92: Materials and shape," *Acta metall,* vol. 39, p. 1025–1039, 1991.

[45] N. K. Katiyar, G. Goel, S. Hawi and S. Goel, "Nature-inspired materials: Emerging trends and prospects," *NPG Asia Materials,* Vols. 13, no. 1, 2021.

[46] A. Gibson and P.S. Nobel , "The Cactus Primer," *Harvard University Press,* 1986.

[47] I. Burgert and J.W.C. Dunlop, "Micromechanics of Cell Walls, Mechanical Integra-," *Springer-Verlag Berlin Heidelberg,* p. 27–52, 2011.

[48] Luca De Vivo, Albert K. Matsushita, Daniel Kupor, Josue Luna, Beatrice A. Tierra, Rober L. Sah and et al., "Cholla cactus frames as lightweight and torsionally tough biological materials," *Acta Biomaterialia,* vol. 112, p. 213–224 , 2020.

[49] D.R. Fowler, P. Prusinkiewicz , J. Battjes and D.R. Fowler , "A Collision-based Model of Spiral Phyllotaxis," *ACM SIGGRAPH,* vol. 26 (2), p. 361–368, 1992.

[50] S. C. Daminabo, S. Goel, S. A. Grammatikos and H. Y. Thakur, "Fused deposition modeling-based additive manufacturing: techniques for polymer material systems," *Materials Today Chemistry,* vol. 16, 2020.

[51] Ultimaker, "Technical datasheet - Ultimaker PP," 2018..

[52] J. Nath, "Chapter 4: Overview of Casting Processes," *Aluminum Castings Engineering Guide,* pp. 29 - 90, 2018.

[53] C. Poli, "Chapter 6 - Metal Casting Processes," *Design for Manufacturing,* pp. 115-126, 2001.

[54] Alessandro Capitanio and Giorgio Carlesso, "Development of advanced high-Mn stainless steels in contact with lead for nuclear lead reactors," 2024.

[55] H. Helms and U. Lambrecht, "The potential contribution of lightweighting to reduce transport energy consumption," *LCA Case Studies Light-Weighting of Vehicles,* 2006.

[56] F. Yoshimasa and N. Yasunobu , "High strength steel sheets for weight reduction of automobiles," 2019.

List of Figures

List if Tables

List of symbols

Variable	Description	SI unit
SFE	Stacking fault energy	mJ/m^2

Appendix

Abbreviations	Description
$\boldsymbol{\alpha}$	Ferrite from austenite phase
$\boldsymbol{\alpha'}$	Martensite
δ	Ferrite from liquid steel
$\boldsymbol{\gamma}$	Austenite
$\boldsymbol{\gamma_o}$	Carbon depleted austenite
$\boldsymbol{\gamma_R}$	Retained austenite phase
$\boldsymbol{\gamma'}$	Solute-lean austenite from high temperature austenite, having $L1_2$ crystal structure
$\boldsymbol{\gamma''}$	Solute-rich austenite from high temperature austenite, having $L'1_2$ crystal structure
β-Mn	Phase with a complicated crystal structure in Fe-Mn-Al-C steels
$\boldsymbol{\kappa}$	Carbide phase $(Fe,Mn)_3AlC$, Al atoms are located at corners, Fe and Mn at the face centred positions, and C at the body centre
$\boldsymbol{\kappa'}$	Metastable phase $(Fe,Mn)_3AlC_x$ $(x< 1)$
$\boldsymbol{\kappa^*}$	κ-carbides formed at grain boundaries
$\mathbf{L1_2}$	γ phase crystal structure, Al atoms are located at corner positions, Fe and Mn at face positions
$\mathbf{L'1_2}$	Crystal structure of κ', with an incomplete occupation of the C atoms
$\mathbf{E2_1}$	A perovskite crystal structure designated in the Strukturbericht classification

Acknowledgments

I would like to express my sincere gratitude to Professor Carlo Mapelli for his constant guidance throughout the entire duration of this thesis. His support was not limited to scientific advice, but extended to every phase of the work, following the development step by step with dedication and attention. I am particularly thankful for the great effort he devoted to establishing the contact with the foundry and making the production of my components possible. His commitment and trust have been fundamental for the successful completion of this research.

I would also like to thank the foundry for the valuable manufacturing support and for the time and care dedicated to the production of my casting components. Their technical expertise, availability, and willingness to accommodate the specific requirements of this work made the realization of the experimental structures feasible.

My sincere appreciation goes to Bazri Shahab for his guidance in the metallographic analysis. His suggestions and scientific insight were essential for correctly interpreting the microstructural results and for approaching the experimental work with a rigorous methodology.

A special thanks is addressed to Ludovica for her patience and kindness in teaching me how to use the machinery in the metallographic laboratory. Her continuous support during the preparation of the samples and the time she dedicated to the SEM and EBSD analyses were extremely important for the quality of the experimental results and for my personal learning.

I am also grateful to Lorenzo for managing the compression tests on the real structures. His help in organizing and conducting the experimental campaign allowed me to obtain reliable and meaningful mechanical data for the validation of the numerical models.

Finally, I would like to acknowledge all the people who, in different ways, contributed to this work and supported me during this journey.

Ringraziamenti

Desidero esprimere la mia più sincera gratitudine al Professor Carlo Mapelli per avermi seguito con costanza e dedizione durante tutto il percorso di questa tesi. La sua guida è stata continua e preziosa in ogni fase del lavoro, sia dal punto di vista scientifico che umano. Gli sono particolarmente riconoscente per l'impegno e il grande lavoro svolto nel contattare la fonderia e rendere possibile la produzione dei miei componenti: senza il suo supporto questo risultato non sarebbe stato raggiungibile.

Un sentito ringraziamento va alla fonderia per il fondamentale supporto nella realizzazione dei getti e per il tempo e l'attenzione dedicati alla produzione dei miei campioni. La loro disponibilità, competenza e collaborazione hanno reso possibile la concretizzazione della parte sperimentale di questo lavoro.

Ringrazio Bazri Shahab per avermi guidato nell'esecuzione delle analisi metallografiche, fornendomi indicazioni preziose e aiutandomi ad affrontare con rigore l'interpretazione dei risultati microstrutturali.

Un grazie speciale a Ludovica per la pazienza con cui mi ha insegnato a utilizzare le macchine del laboratorio metallografico e per il tempo che ha dedicato all'analisi dei miei campioni al SEM e all'EBSD. Il suo aiuto è stato fondamentale sia per la qualità delle analisi sia per la mia crescita personale all'interno del laboratorio.

Desidero inoltre ringraziare Lorenzo per aver gestito le prove di compressione sulle strutture reali. Il suo contributo ha permesso di ottenere risultati sperimentali affidabili e indispensabili per la validazione del modello numerico.

Infine, ringrazio tutte le persone che, in modi diversi, mi hanno supportato e accompagnato durante questo percorso, contribuendo alla realizzazione di questo lavoro.